Investigation of Plasmon Enhanced Optical Properties and Photocatalytic Applications of Composite Nanostructures

By

Gashaw Beyene

A THESIS SUBMITTED TO THE GRADUATE PROGRAMS IN PARTIAL FULFILLMENT
OF THE REQUIREMENTS FOR THE DEGREE OF DOCTOR OF PHILOSOPHY IN
CONDENSED MATTER PHYSICS
AT
ADDIS ABABA UNIVERSITY
ADDIS ABABA, ETHIOPIA
MARCH 2021

ADDIS ABABA UNIVERSITY
DEPARTMENT OF PHYSICS

The undersigned hereby certify that they have read and recommend to the Graduate Programs for acceptance a thesis entitled "**Investigation of Plasmon Enhanced Optical Properties and Photocatalytic Applications of Composite Nanostructures**" by **Gashaw Beyene** in partial fulfillment of the requirements for the degree of **Doctor of Philosophy in Condensed Matter Physics**.

Dated: March 2021

External Examiner: ______________________
Prof. Daniel Wamwangi

Research Supervisor: ______________________
Teshome Senbeta, Belayneh Mesfin and Prof. Q. Zhang

Internal examiner: ______________________
Dr. Chernet Amente

____

ADDIS ABABA UNIVERSITY

Date: **March 2021**

Author: **Gashaw Beyene**

Title: **Investigation of Plasmon Enhanced Optical Properties and Photocatalytic Applications of Composite Nanostructures**

Department: **Physics**

Degree: **Ph.D.** Convocation: **March** Year: **2021**

Permission is herewith granted to Addis Ababa University to circulate and to have copied for non-commercial purposes, at its discretion, the above title upon the request of individuals or institutions.

Signature of Author

To all Ethiopian people who died by COVID-19.

Table of Contents

Table of Contents **v**

Abstract **xiv**

Abbreviations **xvi**

Acknowledgements **xviii**

1 Introduction **1**

2 Optical Properties and Photocatalysis Mechanism of the Material **9**
- 2.1 Introduction 9
- 2.2 Models of Dielectric Functions 10
  - 2.2.1 Drude Free-Electron Model 10
  - 2.2.2 Lorentz Oscillator Model 13
- 2.3 Localized Surface Plasmon Resonances 14
- 2.4 Theory of Light Scattering by Small Particles 15
  - 2.4.1 Scattering, Absorption, and Extinction 16
  - 2.4.2 The Quasi-Static Approximation 17
  - 2.4.3 Spherical Particles - Mie Theory 21
  - 2.4.4 Size Effects 22
  - 2.4.5 Ellipsoidal (Non-Spherical) Particles - Shape Effects 22
- 2.5 Basic Principles and Mechanism of Photocatalysis 27

3 Synthesis of Nanocomposites and Characterization Techniques **30**
- 3.1 Introduction 30
- 3.2 Synthesis Methods 32
  - 3.2.1 Sol-Gel Method 32
  - 3.2.2 Rapid Synthesis Method 32

3.2.3 Green Synthesis Method 33
3.3 Characterization Techniques 33
3.3.1 X-ray Diffraction (XRD) 33
3.3.2 Scanning Electron Microscope (SEM) 37
3.3.3 Transmission Electron Microscope (TEM) 39
3.3.4 X-Ray Photoelectron Spectroscopy (XPS) 41
3.3.5 UV-Visible Spectroscopy 42
3.3.6 Fourier Transform Infrared (FT-IR) Spectroscopy 44

4 Size Dependent Optical Properties of $ZnO@Ag$ Core-Shell Spherical Nanostructures 46
4.1 Introduction 46
4.2 Model of Core-Shell Nanostructure 48
4.3 Numerical Analysis 52
4.4 Results and Discussion 53
4.4.1 Polarizability 53
4.4.2 Refractive Index 56
4.4.3 Optical Absorbance 60
4.5 Conclusions 63

5 Plasmonic Properties of Spheroidal Spindle and Disc Shaped Core-Shell Nanostructures Embedded in Passive Host-Matrices 65
5.1 Introduction 65
5.2 Model of Spheroidal Core-Shell Nanostructure 67
5.3 Numerical Analysis 71
5.4 Results and Discusion 72
5.4.1 Absorption Cross-Section 72
5.4.2 Radiation Efficiency 78
5.5 Conclusions 80

6 Synthesis and Characterization of Ultraviolet Emitter ZnO Nanoparticles for Photocatalytic Application 82
6.1 Introduction 82
6.2 Materials and Methods 85
6.2.1 Materials 85
6.2.2 Methods 85
6.3 Results and Discussion 88
6.3.1 XRD Patterns of ZnO Nanoparticles 88
6.3.2 SEM Analysis 90

6.3.3 Optical Spectroscopy of ZnO Nanoparticles 91
6.3.4 Photocatalytic Degradation Studies for ZnO Nanoparticles . . 92
6.4 Conclusions 95

7 Rapid Synthesis of Triple Layered Cylindrical $ZnO@SiO_2@Ag$ Core-Shell Nanostructures for Photocatalytic Applications 97
7.1 Introduction 97
7.2 Materials and Methods 100
7.2.1 Materials 100
7.2.2 Synthesis of Core-Shell Nanoparticles 101
7.2.3 Characterization of the Samples 102
7.3 Results and Discussion 103
7.3.1 XRD Patterns of ZnO Nanoparticles 103
7.3.2 TEM Analysis 105
7.3.3 SEM Analysis of $ZnO@SiO_2@Ag$ Nanocomposite 107
7.3.4 Optical Spectroscopy of Core-Shell Structures 107
7.3.5 X-ray Photoelectron Spectroscopy (XPS) 108
7.3.6 Photocatalytic Activity and Stability of the Samples 110
7.3.7 Cyclic Stability of Triple Layered Core-Shell Nanostructure . . 115
7.4 Conclusions 116

8 Enhancing the Photocatalytic Application of Bi Doped/Undoped TiO_2 Nanoparticles Using Ginger (Zingiber Officinale) Extract 118
8.1 Introduction 118
8.2 Materials and Methods 122
8.2.1 Materials 122
8.2.2 Synthesis Methods 122
8.2.3 Photocatalytic Degradation of Trypan Blue Dye 124
8.2.4 Characterization Techniques 125
8.3 Results and Discussion 125
8.3.1 XRD Pattern Analysis 125
8.3.2 SEM Analysis of Bi- Doped/Undoped TiO_2 128
8.3.3 Fourier Transform Infrared Spectroscopy (FT-IR) 128
8.3.4 Chemical Stability of Bi- Doped TiO_2 Nanoparticles 129
8.3.5 UV-Vis Analysis 131
8.3.6 Photocatalytic Activity 132
8.4 Conclusion 136

9 Conclusions and Future Work **137**
9.1 Conclusions 137
9.2 Future Work 139

Bibliography **142**

List of Figures

2.1 (a) A single metal atom; (b) view of metal in Drude model. 11

2.2 Homogeneous nano-sphere in electrostatic field. 18

2.3 Schematic model of ellipsoidal particle. 23

2.4 Schematic diagram of a spheroidal particle with dimensions (a, b, c), such as $a > b = c$ (prolate left) and $a < b = c$ (oblate right) [33]. . . . 26

2.5 Schematic diagram of photocatalytic reaction mechanism. 28

3.1 Illustration of the two types of synthesis processes and the suite of methods for fabricating nanoparticles. 31

3.2 A schematic diagram of Braggs reflection from the crystal 36

3.3 A schematic diagram of scanning electron microscope (SEM) 37

3.4 The interaction of electron with the sample in different depth and the signal after interaction 38

3.5 Simplified diagram of transmission electron microscope. 40

3.6 Schematic diagram of working principle of X-ray photoelectron spectroscopy (a) and schematic diagram of binding energy (b). 41

3.7 Interaction of reference and sample beam from UV-Vis source with sample cuvette and reference cuvette and the compression of their intensities. 43

3.8 A schematic diagram of interaction of light source and laser with the sample in FT-IR spectroscopy. 45

4.1 The schematic diagram of $ZnO@Ag$ spherical core-shell nanostructure with dielectric function of ZnO,ε_1 and Ag, ε_2. 49

4.2 The real part of the polarizability of the spherical nanoinclusions as a function of wavelength for different values of β. 55

4.3 The imaginary part of the polarizability of the spherical inclusions obtained for different value of β. 56

4.4 The real part of the refractive index as a function of wavelength for fixed filling factor $\xi = 0.001$ and different value of β. An increase in the metal fraction is indicated by the 'heads' of dashed arrows. 58

4.5 The real part of the refractive index obtained for $\beta = 0.875$ and different value of filling factor, ξ. 59

4.6 The imaginary part of the refractive index of the spherical inclusions obtained for different value of β and fixed filling factor $\xi = 0.001$. . . 60

4.7 The absorbance of the spherical inclusions obtained for different value of t_{Ag} and $\xi = 0.001$. The radii (a_2) of the QDs is 20 nm. 62

5.1 The arrays (A) and the structure (B) of core-shell nanostructure, with prolate (B(i)) oblate (B(ii)) shaped CSNS embedded in host matrix . 68

5.2 The absorption cross-sections for (A) spindle- and (B) disc-shaped CSNSs; for $AR_c = 2.33,\ 3.00,\ 5.00$ and constant $AR_s = 2.0$, $\varepsilon_h = 2.25$ [109]. 73

5.3 σ_{acs}, σ_{scs} and σ_{ecs} of the same size of spindle shaped; for $AR_c = 1.67$, $AR_s = 1.20$, $t = 5\ nm$, and $\varepsilon_h = 2.25$. 75

5.4 LM and TM resonance modes of spindle- and disc-shaped spheroids as a function of wavelength. The parameters used are $AR_s = 2.0$, $AR_c = 2.33$, and $t = 5\ nm$. 76

5.5 The effect of shape on LM and TM resonance modes of the absorption cross-section spectra for (A) spindle-shaped and (B) disc-shaped spheroids, for $AR_s = 2.0,\ 1.67$. The parameters used are $AR_c = 2.33,\ 1.88$, and $t = 5\ nm$. 77

5.6 The absorption cross-section of a spindle-shaped spheroid as a function of wavelength, for a host matrix of five different refractive index $RI = \sqrt{\varepsilon_h}$. The other parameters are $AR_s = 2.0$,$AR_c = 2.33$, and $t = 5$ nm. 78
5.7 Radiation efficiency of (A) the disc-shaped, (B) the spindle-shaped CSNSs as a function of wavelength; for three different values of AR_c. The other parameters are similar to that used in Fig. 5.2. 79

6.1 XRD pattern (a) and SEM image of ZnO NPs (b-f). 90
6.2 UV-Vis absorption spectra of ZnO nanoparticles synthesized via three routes from the same precursors. 92
6.3 The band gap energies plotted as $(\alpha h\nu)^2$ Vs $h\nu$ of zinc oxide nanoparticles. 93
6.4 Percentage of degradation (a), photocatalytic activity (b), the summary of percentage of degradation (c) and photocatalytic activity (d) of zinc oxide NPs, and schematic of mechanism for MO degradation over ZnO NPs under UV irradiation. 94

7.1 XRD pattern of $ZnO@SiO_2$ and $ZnO@SiO_2@Ag$ CSNPs. 104
7.2 TEM image of $ZnO@SiO_2$ (a,b) and $ZnO@SiO_2@Ag$ (c,d) cylindrical CSNPs and EDS result of $ZnO@SiO_2@Ag$ (e,f). 106
7.3 SEM image of $ZnO@SiO_2$ CSNPs ($ZS12$, $ZS4$) and $ZnO@SiO_2@Ag$ CSNPs ($ZSA12$, $ZSA4$). 108
7.4 UV-Vis absorption spectra of $ZnO@SiO_2$ and $ZnO@SiO_2@Ag$ nanoparticles synthesized from two ZnO NPs which are calcinated at different time. 109
7.5 The optical absorption band gap energy estimated using Tauc's plot relation for $ZnO@SiO_2$ and $ZnO@SiO_2@Ag$ CSNPs. 110
7.6 The survey scan XPS spectrum of $ZnO@SiO_2@Ag$ CSNPs. 111
7.7 High resolution XPS spectra of (a) ZnO $2p$, (b) SiO_2 $2p$, (c) Ag $3d$, and (d) O $1s$. 112

7.8 Percentage of degradation (a), photocatalytic activity (b), the summery of percentage of degradation (c) and photocatalytic activity (d) of double and triple layered CSNPs, and schematic of mechanism for MB degradation over triple layered CSNPs under UV irradiation light. 113

7.9 Cyclic photodegradation curve for the triple layered $ZnO@SiO_2@Ag$ CSNSs photocatalyst. 115

8.1 XRD pattern of $Bi-$ doped/undoped TiO_2 nanostructure using green synthesis and chemical synthesis route. 126

8.2 SEM image of $Bi-$ doped/undoped TiO_2 nanostructure using green synthesis and chemical synthesis method. 129

8.3 FT-IR spectra of Bi- doping and undoping green synthesized TiO_2 nanostructures. 130

8.4 The survey scan XPS spectrum of (a) $GB5T$ and $GB3T$, (b) high resolution XPS spectra of $GB5T$ Ti $2p$ and $GB3T$ Ti $2p$, (c) $GB5T$ Bi $4f$ and $GB3T$ Bi $4f$, and (d) $GB5T$ O $1s$ and $GB3T$ O $1s$. . . . 131

8.5 Optical absorbance (A) and band gap energy (B) of Bi- doping and undoping green synthesized TiO_2 nanostructures. 133

8.6 Efficiency of photo-degradation (a) and the photocatalytic activity (b) of green synthesized Bi- doped/undoped TiO_2 nanostructure versus irradiation time. 134

8.7 Schematic mechanism of photocatalysis process on $Bi-TiO_2$ nanoparticles under visible light irradiation. 135

List of Tables

6.1 Crystallite size for a particular plane (D at $hkl = 101$) (2^{nd} column), interplanar spacing at d_{101} (3^{rd} column) and average crystallite size (D) (4^{th} column) of ZnO NP. 89

7.1 Crystallite size of the nanoparticles prepared at a reaction temperature of 400 ^0C. 104

8.1 Spacing and Miller indices of Bi- doped/undoped TiO_2 NPs. 127

Abstract

In this dissertation, we investigated plasmon enhanced optical properties and photocatalytic applications of composite nanostructures by using noble materials from theoretical and experimental perspectives.

The theoretical investigation mainly focused on the optical and plasmonic properties of spherical and spheroidal $ZnO@Ag$ core-shell nanocomposite embedded in non-absorptive medium. The effective dielectrics function, polarizability, refractive index and optical absorbance for spherical as well as absorption cross-section and radiation efficiency for spheroidal nanocomposite are studied. These optical and plasmonic properties are tuned when size of core and/or composite, shell thickness, shape of core and/or shell, and refractive index of the host-medium is changed. In spherical nanocomposite, there are two resonances associated with interfaces while in spheroidal nanocomposite four plasmonic resonances are appeared that correspond to interfaces and the bonding/antibonding pairs. The tunable of plasmonic resonances from UV to infrared spectral regions of such composite enables it to exhibit very interesting material properties in a variety of applications.

Experimentally, we emphasized the optical properties and photocatalytic applications of ZnO nanoparticles, triple layered $ZnO@SiO_2@Ag$ core-shell composite nanostructures and Bi doped/undoped TiO_2 nanostructures. In particular, we synthesized ZnO nanoparticles using three different methods as presented in the experimental section of the study. Due to different synthesis methods and procedures as well as different surfactant/stablizing agent, the synthesized ZnO nanoparticles have different morphology, band gap energy, varying quantum size effect and photocatalytic responses. The photocatalytic performance of ZnO nanoparticles were evaluated by using methyl orange dye as a pollutant under UV-light irradiation. Triple layered $ZnO@SiO_2@Ag$ core-shell nanocomposites are also fabricated at 400 ^oC for different calcination time. The photocatalytic activity and stability of the as-synthesized samples were evaluated by photo-degradation of organic methylene blue under ultraviolet light irradiation. When $ZnO@SiO_2$ is coated with Ag, the stability and photocatalytic performance of the composite $ZnO@SiO_2@Ag$ photocatalysts were highly enhanced. In addition, Bi- doped/undoped TiO_2 nanoparticles are synthesized by green synthesis method using zingiber officinale extract solution. After doping Bi, the band gap energy is decreased from 3.00 eV to 2.76 eV, absorption region is shifted to visible range of solar spectrum, and surface function is modified. The photocatalytic activity of the sample is analyzed by UV-Vis spectroscopy using trypan blue dye. The photo-degradation efficiency of chemical synthesis TiO_2 nanoparticles is enhanced to 98.34 % by doping basic metal Bi and using ginger extraction solution. The synthesized samples were analyzed using a characterization techniques such as X-ray diffraction (XRD) spectroscopy, scanning electron microscope (SEM), Transmission electron microscope (TEM), Ultraviolet visible (UV-Vis) spectroscopy, Fourier transform infrared (FT-IR) spectroscopy, and X-ray photoelectron spectroscopy (XPS).

Abbreviations

- Ag - Silver
- AR - Aspect ratio
- Bi - Bismuth
- CSNP - Core-shell nanoparticle
- CSNS - Core-shell nanostructure
- DF - Dielectrics function
- DSSC - Dye sensitive solar cell
- DI - Deionized
- EM - Eelectromagnetic
- FTIR - Fourier transform infrared
- LED - Light emitting diode
- LM - Longitudinal mode
- MB - Methylene blue
- MO - Methyl orange
- MOF - Metal oxide framwork

- NP - Nanoparticle
- NS - Nanostructure
- PR - Plasmonic resonance
- QD - Quantum dot
- RT - Room temperature
- TB - Trypan blue
- TCO - Transparent conducting oxide
- TEM - Transmission electron microscope
- TiO_2 - Titanium Dioxide
- TM - Transverse mode
- SPR - Surface plasmonic resonance
- LSPR - Localized surface plasmon resonance
- SiO_2 - Silicon dioxide
- XPS - X-ray photoelectron spectroscope
- XRD - X-ray difractometer
- RI - Refractive index
- UV-Vis - Ultraviolet visible
- SEM - Scanning electron microscope
- ZnO - Zinc oxide

Acknowledgements

Accomplishment of a study of such scale cannot be anticipated without contribution of many individuals and institutions. It would be thus fair to mention people and institutions that have provided much needed support for the successful completion of the research project.

Primarily, I am sincerely indebted to my advisors, Dr. Teshome Senbeta, Dr. Belyaneh Mesfin, and Prof. Qinfang Zhang not only for their brotherly approach but also for their insightful professional assistance and academic support all through the duration of the study. Thank you all for your unforgettable, terrific commitment and invaluable support. I am also thankful to Dr. Chernet Amente for his support, showing direction and advice during my Ph.D courses and seminars. I want to extend my gratitude to Ms. Tsilat Adinew for her help in non-scientific related jobs like finance and documentation.

My experimental research experience was greatly enhanced by opportunities to collaborate with excellent researchers in Yancheng Institute of Technology, China. I would especially like to thank Miss Ni Han and Dr. Anjli Sharma for their kind and patient help during lab work. A big thank you, also, to Dr. Zhu lei and Dr. Liu Chao for allowing me to use their laboratory and for their generously guidance during lab work. Thank you all for all your support.

I am grateful to Ph.D students in AAU, for their help, support, camaraderie, and friendship; especially to Mr. Gamachis Sakata for always providing an enable environment through motivating discussions.

This work was financially supported by Yancheng Institute of Technology (NSFC, China), Addis Ababa University and Adama Science and Technology University.

I express my deep gratitude to my dearest wife W/o Hawolet Yimam, for all her patience, courage and sacrifice of loneliness you put up with when I was completely occupied in this pursuit. I love you and I am honestly humbled by your never-ending support. I thankful to my children Bilal Gashaw and Nejat Gashaw for that wonderful

smile and playful time that you were always able to create.

Chapter 1

Introduction

Nowadays, researchers devoted their time to fabricate materials which have different properties for the desire applications. The basic component of these is the nanoparticles, which are 1 nm to 100 nm in size in one dimension at least [1, 2]. At the present time, nanoparticles have been investigated expansively due to their novel material properties and applications compared to their bulk counterparts. To produce new materials with novel properties and applications, nanoparticles have been combined with other nanoparticles to form nanocomposites which enhances their functionalities. In an other word, the alternative way of resolving the limitation of microcomposites and monolithics as well as nanoparticles is nanocomposite materials. Once the materials are achieved nanometer scale at least in one dimension, interactions at phase interfaces are greatly improved, and this is playing a crucial role for the improving of properties. In this context, surface area to volume ratio and quantum confinement effect of reinforcement materials employed in the preparation of nanocomposites is crucial to the understanding of their structure-property relationships [3]. Nanocomposite can be made in the form of doping, alloying, hetero-structure, core-shell, and cluster. The preparation of nanocomposite is a challenging task as it requires careful control of the stoichiometry of all constituent materials. Nanocomposites as well as nanoparticles have been used for various applications like; solar cell, photocatalysis, biological application, pharmaceutical application, drug delivery, electronics device, energy and data storage, and others. Nanocomposites have modified, enhanced, or unique/new application or properties than it's individual components. In a nanocomposite materials, one of the constituents is a continuous matrix which is called a host matrix (host medium) while the others dispersed in the host matrix are called inclusions or fillers. This work mainly focused on plasmonic and optical properties core-shell nanocomposites and photocatalytic application of both nanoparticle and composite nanostructures.

With the growth of nanoscience and nanotechnology, engineering of core-shell (discovered in late 1980) nanocomposites provide the formation of multifunctional materials in different field of technological application and has aroused scientific research in the recent years. Due to the interface feature of core-shell nanostructures, enhancements in the chemical, electrical, catalytic, magnetic, and optical/plasmonic properties of new material with various applications are of interest. The shell is usually used as the barrier between the core material and the surrounding material and can alter the charge, surface reactivity, functionality, stability, toxicity, dispersive ability and cost effectiveness of the core material [4, 5]. The ultimate goal of engineering core-shell nanocomposite structure is to obtain new material which has modified/enhanced or unique/new property for the desire applications. Double, triple or multilayered core-shell nanocomposite can be from different material configurations and combination such as from metal, metal oxide, dielectrics or organic/inorganic materials with different combination way, where one material is a core and the other the same/different material is a shell [6]. The properties and applications of core-shell nanocomposite are depend on core size/shape, shell thickness/shape, number of layer, material type of core and/or shell, and refractive index of the surrounding medium.

The other alternative way of improving the shortcoming of nanomaterials is by doping with transition metal, basic metal, nonmetal, and rare earth element [7]. The dopant material can modify the band gap energy, recombination rate of photoinduced charge separation, thermal/chemical stability, and morphology of the material [3, 8]. Associated with these modified/improved parameters, the properties as well as applications of nanocomposite are modified/enhanced [9]. The properties and applications of doped nanomaterial are depend on the concentration of dopant, dopant sites, method of fabrication, morphology, and crystalline.

Large number of industries/factories release untreated by-product to the environment. Specially, the by-product from dye and textile industries are aromatic compounds, potentially toxic and difficult to degrade. The discharge of by-product from these industries can directly affect aquatic organisms, human health/live and ecosystem/biodeversity [10]. These discharge by-product can easily mix with water reservoirs/damps that can be used for drinking and directly/indirectly affects the human health through food chain, and reducing soil fertility [11]-[14]. Therefore, the treatment of these by-products is needed before and/or after release to the environment/community. To treat such waste materials, catalytic methods of degradation using nanocomposite like; core-shell and doping [15, 16] as well as nanoparticle are promising materials [17]. Nowadays, nanotechnology and nanoscience have been given great scope for the fabrication of desirable nanocomposite materials with large surface to volume ratios, unique surface functionalities, and low band-gap energy to treat these pollutants through oxidation processes. Among advanced oxidation process method, photocatalytic degradation is the effective means of degrading organic pollutant [18]. In this process, hydroxyl radical used for degrading pollutants via conversion to harmless minerals [11].

Modern nanoscience and nanotechnology are the creation and exploitation of nanoparticles with structural features in between in those of molecules and their bulk counterpart. In other words, nanoscience and nanotechnology are a technology of design and fabrications of nanoscale materials with unique properties and functions. Nanoparticles are fabricating for different application, like solar cell, photocatalysis, medical application, electronics device, cosmetics materials, energy and data storage device and others. However, nanoparticles have their own limitations or shortcomings for the require applications regarding to their band gap energy, fast recombination of hole-electron pairs, morphology, and size. These limitations or shortcomings are overcome by making alloy, core-shell, doping, hetero-junction, and by using other mechanism. In addition, when nanomaterials are fabricated using chemical synthesis method, the by-product can be hazardous to the ecosystem, animals, and biodiversity and the synthesized nanomaterials may not be stable. The green synthesis method is an alternative method of chemical synthesis and the extracted solution used as reducing, capping and stabilizing agent. Cost-effective, easy to fabrication, and using nature gift for different applications like cosmetics, medical, biological application are the other opportunity of green synthesis method.

Recently, many researchers most extensively studied oxide based nanomaterials for various applications specially as photocatalyst. Among these nanomaterials, metal oxide nanoparticles like ZnO and TiO_2 are a promise for various applications. ZnO

and TiO_2 are also non-toxic, inexpensive, chemical stable, relative abundance, easiness to fabricate as nanostructures with different morphology, and show different properties. But, these two materials have wide band gap energy and poor visible light absorption efficiency. In the past few decades, many effective approaches have been devoted to overcome the drawbacks and to enhance the properties in the field of photocatalysis. In band gap energy and electron-hole recombination rate concern, dopping and core-shell structures are more preferable. Under this consideration, ZnO and TiO_2 based core-shell and basic metallic dopant nanocomposites are studied, respectively. As far as our knowledge concern, ZnO based triple layered core-shell composite nanostructure for photocatalytic application and green synthesis of Bi doped/undoped TiO_2 nanostructures using ginger extraction solution for photocatalytic application are not reported.

The **main objective** of this study is to investigate plasmon enhanced optical properties and photocatalytic applications of composite nanostructures. The **specific objective** of the studies are:

- Investigate the enhancement of optical and plasmonic properties of spherical and spheroidal $ZnO@Ag$ core-shell nanocomposites.
- Photocatalytic response of ZnO nanoparticles, $ZnO@SiO_2@Ag$ core-shell composite nanostructures and Bi doped/undoped TiO_2 nanostructures are studied.
- Compare and analyze the effect of green and chemical synthesis method of ZnO and $Bi-$ doping $\mathrm{TiO_2}$, calcination time of $ZnO@SiO_2$ and $ZnO@SiO_2@Ag$ sample, and the concentration of Bi dopant in TiO_2 on the photocatalytic response.

- Study the effect of plant extracted solution on the photocatalytic response and structural properties of ZnO nanoparticles.
- Synthesis of $ZnO@SiO_2@Ag$ as a more stable and reusable photocatalytic composite for photodegradation.
- Enhance the photo-degradation efficiency of chemical synthesis TiO_2 nanoparticles using basic metal Bi as a dopant and using ginger extraction solution.

This dissertation contains two parts: theoretical and experimental. In **theoretical part**, we have investigated the plasmonic/optical properties of $ZnO@Ag$ core-shell spherical and spheroidal nanocomposites. The properties mainly depend on the interfaces and axes of oscillation of free electrons. Based on these two factors, two plasmonic resonances are appeared in spherical shaped nano-composites while four plasmonic resonances are appeared in spheroidal composite. In **experimental part**, synthesis and characterization of ZnO, $ZnO@SiO_2@Ag$ and Bi-doped TiO_2 by varying the parameters; calcination time, concentration, temperature, synthesis method, and type of extracted solution are investigated. The photocatalytic application and properties of synthesized nanomaterials are studied in detail. The dissertation is organized as follows:

- Chapter 2: In this chapter we present the interaction of metal/dielectrics composite with incident field wave and the optical response of the interaction. To study the optical/plasmonic properties of the composite, we will use two models; Drude free-electron model for metallic and Lorentz model for semiconductor material. The theory of light scattering by small particle is also addressed under this chapter.

- Chapter 3: Under this chapter we describe in detail the synthesis methods and the characterization tools used for this work.

- Chapter 4: In this chapter we will study the effect of size and shell thickness variation on the optical properties of a system consists of spherical $ZnO@Ag$ core-shell nanocomposites embedded in host matrix. Under this chapter the effective dielectrics function, polarizability, refractive index and optical absorbance of the composite are studied.

- Chapter 5: This chapter is devoted to the discussion of the plasmonic properties of $ZnO@Ag$ spindle- and disc-shaped core-shell nanocomposites embedded in the dielectrics passive host matrices. In particular, absorption cross-section and radiation efficiency of the composite is studied by varying the size and shape of composite, shell thickness, and dielectrics function of the host matrix.

- Chapter 6: Presents the photocatalytic activity of ZnO nanoparticle prepared by three synthesis methods; rapid, sol-gel and green synthesis under ultraviolet radiation. The photocatalytic performance of ZnO nanoparticle is evaluated by using methyl orange as a pollutant model.

- Chapter 7: A detail description of synthesis method and characterization techniques of triple layered $ZnO@SiO_2@Ag$ core-shell nanocomposite were discussed in this chapter. The photocatalytic activity, stability and also the properties of the sample is investigated under this section.

- Chapter 8: In this section we will develop cost-effective and eco-friendly techniques employed for the synthesis of $Bi-$ doped and undoped TiO_2 nanoparticles using zingiber officinale extract solution. The photocatalytic activity of synthesis samples analyzed by UV-Vis spectroscope using trypan blue dye.

- Chapter 9: Finally, a conclusion of the results obtained in the work and a proposed direction of the future work is presented under this chapter.

Chapter 2

Optical Properties and Photocatalysis Mechanism of the Material

2.1 Introduction

Interaction of light with nanocomposites/nanomaterials show new plasmonic/optical property without changing the properties of the materials. The linear and nonlinear optical response of metal nanoparticles is specified by oscillation/excitation of the surface electrons in the Coulomb potential formed by the positively charged ionic core. This type of excitation is called the surface plasmon (SP) [19]. In 1908, Mie proposed a solution of Maxwell's equations for spherical particles interacting with plane electromagnetic waves, which explains the origin of surface plasmon resonance (SPR) in the extinction spectra and colouration of metal colloids [20]. The optical properties of plasmonic (metallic) materials have been studied for almost more than a century. These studies showed that metal dielectric composites exhibits different optical properties due to interfacial effect, when illuminated by plane waves. Since, the optical properties of metal nanoparticles are governed by SPR, they are strongly dependent on the nanoparticle size, shape, concentration and spatial distribution as well as on the dielectrics properties of the surrounding matrix (host medium).

An incident field wave propagating through different media is affected by interactions with each medium as it traverses across the boundary between one medium and another. The discussion on incident field waves has been limited to the propagation of waves and interactions with simple structures composed of arbitrary media. In the following section, two different models to describe the optical response of a simple structure model will be discussed: Drude free-electron model and the Lorentz oscillator model. Both models approximately describe the plasmonic/optical properties of the nanoparticles in various geometrical size and shape and interactions. This chapter will include a brief description of the theory of light scattering by solids with nanometers and sum-microns dimensions.

2.2 Models of Dielectric Functions

2.2.1 Drude Free-Electron Model

When incident electric field interacts with metallic or nonmetallic medium, different optical responses will be displayed. This response optical difference arise due to the nature of the confinement of the electrons. In the event of free/conducting electrons, the presence of an oscillating field induces electronic oscillations due to the columbic interaction within the surface the displacements of the center of mass of the electron cloud from the ionic core constitutes the creation of a dipole. By definition the displacement of the charge from its equilibrium position can be permanent and spontaneous or temporarily induced. For bound electrons the effect of the field is seen through band to band transition as will be described in the Lorentz model. In metallic medium, the overlap of conduction and valence band allows for the excitation of electron with very little energy to different energy and momentum states by absorption of photons.

In 1900, Paul Drude developed a theory to explain the electrical and thermal conductivities in metals [21, 22]. Drude model takes a metal as a free gas of electrons and applies kinetic theory of gases. In our discussion of the Drude model, we shall simply assume that, in the formation of a metal, the valence electrons become detached and wander freely through the metal, while the metallic ions remain intact and act as immobile positive particles, as shown in Fig. 2.1.

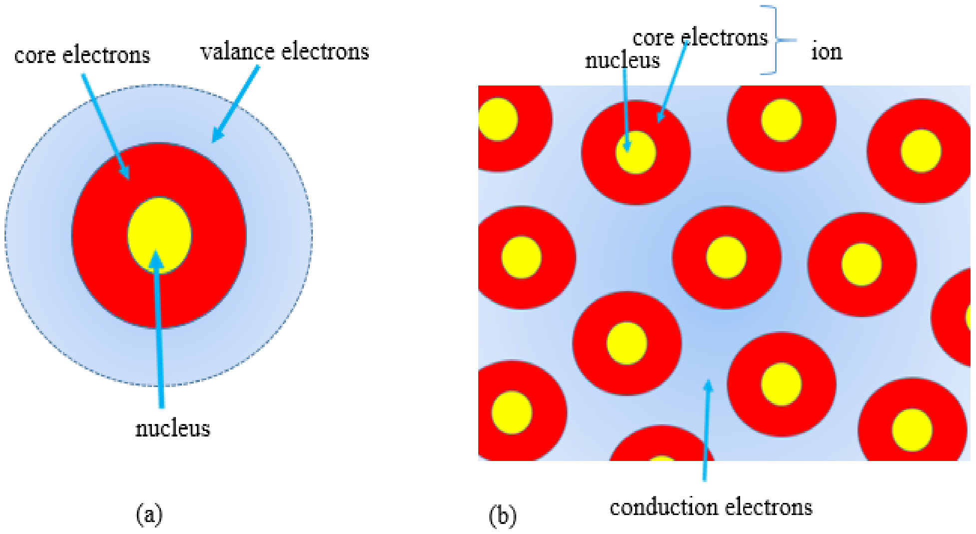

Figure 2.1: (a) A single metal atom; (b) view of metal in Drude model.

In this approach, when the external electric field $\mathbf{E} = \mathbf{E}_0 e^{-i\omega t}$ is applied to a metallic system the electric charge (q) is displaced. The equation of motion for an electric charge (electron) of mass m is defined by

$$\frac{d^2\mathbf{r}}{dt^2} + \gamma\frac{d\mathbf{r}}{dt} = -\frac{q\mathbf{E}_0}{m}e^{-i\omega t}, \tag{2.2.1}$$

where r is the displacement of the electron from the equilibrium point and E_0 is the amplitude of the applied electric field. The damping constant γ is related to the lifetimes of all electron scattering processes, namely; electron-electron, electron-phonon and electron-defect/impurity scattering processes in the bulk metallic materials.

The trial solution $\mathbf{r} = \mathbf{r}_0 e^{-i\omega t}$ of Eq. (2.2.1) yields:

$$\mathbf{r}(t) = \frac{q\mathbf{E}(t)/m}{\omega^2 + i\gamma\omega}. \tag{2.2.2}$$

Approximating the electron motion with that of a harmonic oscilator, and invoking 2.2.2 into the expression for the dipole moment $\mathbf{p} = -q\mathbf{r}$ gives the polarization density as

$$\mathbf{P} = n\mathbf{p} = -nq\mathbf{r} = -\frac{(nq^2\mathbf{E}_0/m)e^{-i\omega t}}{\omega(\omega + i\gamma)} = -\frac{\omega_p^2}{\omega(\omega + i\gamma)}\mathbf{E}\varepsilon_0, \tag{2.2.3}$$

where n is the number of dipole moment per unit volume and ω_p is the plasma frequency of the free electron gas (Fermi sea) defined by the expression:

$$\omega_p^2 = \frac{nq^2}{\varepsilon_0 m}, \tag{2.2.4}$$

where ε_0 is the permittivity of free space.

Similarly, from the relation between electric displacement ($\mathbf{D}$) and local electric field ($\mathbf{E}_0$) i.e., $\mathbf{D} = \varepsilon_0\mathbf{E}_0 + \mathbf{P}$, thus the frequency dependent dielectric function of the given system can be expressed as:

$$\varepsilon(\omega) = 1 - \frac{\omega_p^2}{\omega^2 + i\gamma\omega}. \tag{2.2.5}$$

Eq. (2.2.5) demonstrates that the dielectric constant can become zero near the plasma frequency where the material can support collective modes of oscillating electrons in phase with each other. By tuning the geometry of the structure, the oscillation can occur at negative values of the dielectric constant.

For nobel metals, like Ag, Au, Cu, the optical response to electric field is dominated by free electrons in s band in the region $\omega > \omega_p$, since the filled d band close to the Fermi surface causes a highly polarized environment. This effect can be described by a dielectric constant ε_∞, and we can write

$$\varepsilon(\omega) = \varepsilon_\infty - \frac{\omega_p^2}{\omega^2 + i\gamma\omega}. \tag{2.2.6}$$

2.2.2 Lorentz Oscillator Model

In noble metals such as Au, Ag and Cu, the bound electrons undergo interband transitions especially at higher frequencies ($\sim 10^{12}\ Hz$). These transitions give the luster in these metals. As we stated previously the optical properties of the metals is associated with harmonic motion of the conduction electrons relative to the stationary ionic cores, the behavior of bound electrons cannot be described using Drude model. Hence the plasma model due to H.A. Lorentz is used as a classical approach to describe the optical properties of electrons and ionic motion at high frequencies. The plasma model was developed by H. A. Lorentz as a classical approach to describe optical properties of materials by assuming that electrons and ions of a medium are simple harmonic oscillators and neglecting material properties such as the lattice potential and electron-electron interactions. In Lorentz's model, such inter-band transition can be described as a restoring force modeled by Hookes law.

$$F = -k\mathbf{r} = -m\mathbf{r}\omega_0^2. \tag{2.2.7}$$

Therefore, for the applied time-dependent electric field, the motion of an electron oscillator include restoring force, written as

$$\frac{d^2\mathbf{r}}{dt^2} + \gamma\frac{d\mathbf{r}}{dt} + \omega_0^2\mathbf{r} = -\frac{q\mathbf{E}_0}{m}e^{-i\omega t}, \tag{2.2.8}$$

where $k\mathbf{r}$ is the restoring force for an electron with a spring constant k and $\omega_0 = \sqrt{k/m}$ is natural frequency.

The solution of Eq. (2.2.8) can be written as

$$\mathbf{r} = \frac{(q\mathbf{E}_0/m)e^{-i\omega t}}{\omega^2 - \omega_0^2 + i\gamma\omega}. \tag{2.2.9}$$

The optical constants for a system of N oscillators is derived through the dielectric function for the bulk material as

$$\varepsilon(\omega) = 1 + \chi = 1 + \frac{\omega_p^2}{\omega_0^2 - \omega^2 - i\gamma\omega}, \tag{2.2.10}$$

where χ is dielectric susceptibility.

The dielectric function (DF) of the system can be decomposed into the real, ε_1 and imaginary, ε_2 components, i.e., $\varepsilon(\omega) = \varepsilon_1 + i\varepsilon_2$. At the natural frequency, ω_0, the imaginary part of the dielectric constant is maximum.

2.3 Localized Surface Plasmon Resonances

When the incident electric field interacts with metallic nanomaterials, the conduction electrons oscillate coherently by displacing the electron cloud from the nuclei rise to a spontaneous surface charge distribution. Due to the separation of positive and negative (electron) charge a restoring force is induced by the Coulomb interaction, characterized by oscillation frequencies of the electron cloud relative to the positive one. Each collective oscillation with different surface charge (free electron) distribution is called surface plasmon resonance (SPR), confined to the interface between metal and dielectric.

Optical properties of materials which have the size smaller or comparable to the wavelength of incident field are an intensive research area. The main concept of this area is the surface plasmon resonance for different geometries, alloys and dielectrics environments. Localized surface plasmons are non propagating excitations of the conduction electrons of metallic nanostructures coupled to the incident field [23]. Consider a metallic structure whose size is much smaller than the wavelength of the applied electromagnetic/electric field. When such a metallic structure interacts with an oscillating field, the field both inside and near-field zone outside the structure is enhanced due to the resonance of electrons on its surface. Such kind of resonance is called localized surface plasmon resonance (LSPR). The plasmonic/optical, magnetic and other properties of metal and metal based composites are highly influenced by LSPR [24]. The wavelength of surface plasmon resonance is depend on the type of material (composition), geometry and size of nanoparticles, electron density, and refractive index of surrounding material.

2.4 Theory of Light Scattering by Small Particles

When a nanoparticle is under the action of an incident field light, light rays can be reflected/redirected in random directions due to the presence of obstacle or inhomogeneities which result in the change in the refractive index of the material. Therefore the interaction of incident light with the materials causes the electronic cloud, electron begin to oscillate, transforming energy from incident wave to another form of energy in an absorption process. The electrons of the target material can also be accelerated and then irradiated in scattering process. The attenuation of electromagnetic wave going through nanoparticles dispersed in homogenous medium is the sum of absorption and scattering called electromagnetic (EM) extinction.

2.4.1 Scattering, Absorption, and Extinction

The plasmonic/optical properties of spherical and spheroidal (oblate, prolate shape) of nanostructures are quantified in terms of absorption (σ_{acs}), scattering (σ_{scs}) and extinction (σ_{ecs}) cross-sections. The extinction cross-section represents the loss of energy from the incident beam due to both absorption and scattering cross-section. Absorption (σ_{acs}) and extinction (σ_{ecs}) cross-sections as well are defined as the area removed from the incident beam due to absorption by the medium and the total area removed by the medium, respectively. The relation of these three terms are expressed as follows:

$$\sigma_{ecs} = \sigma_{acs} + \sigma_{scs}. \tag{2.4.1}$$

The scattering and absorption cross-sections as well as extinction cross-section are related to the polarizability of a solid. Polarizability (α) of spherical and ellipsoidal geometry has different expression (see Eq. (2.4.18) and (2.4.45)). Based on the quasi-static approximation, the expression of the corresponding cross-sections, in terms of polarizability, are given by [25, 26],

$$\sigma_{scs} = \frac{k^4}{6\pi}|\alpha|^2, \tag{2.4.2}$$

$$\sigma_{acs} = kIm[\alpha], \tag{2.4.3}$$

where $k = 2\pi\sqrt{\varepsilon_h}/\lambda$ is the wavevector with λ and ε_h are the wavelength of the incident field light and dielectric function of the host medium, respectively. The scattering cross-section is related to the imaginary part of polarizability (i.e., $Im[\alpha]$). Polarizability is proportional to the volume of any geometrical structure, within this regard, σ_{acs} depends on the linear volume while σ_{scs} depends on the square of volume. Therefore, in small structure absorption is dominant and in large structure scattering is dominant [27].

2.4.2 The Quasi-Static Approximation

When the considered nanoparticle's size is much smaller than the incident electric field's wavelength, the incident electric field may be regarded as spatially uniform over the entire of the particle; this is the quasi-static approximation. Despite its simplicity and lack of rigor, this approach is useful for qualitative understanding of the phenomena related to light scattering by nanoparticles as it considerably simplifies the mathematical analysis. In this case, the electrostatic solution can be obtained by solving Laplace equation for the potential. Considering a spherical nanoparticle with a radius r, which is much more smaller than the incident field's wavelength, embedded in a nonconducting host material, the phase retardation of the oscillating field over the sphere can be neglected. Thus the field can be approximately treated as an electrostatic field $E = E_0\hat{z}$ as shown in Fig. 2.2. ε_h and $\varepsilon(\omega)$ (or simply written as ε) are the relative permittivity of the surrounding medium and that of the sphere (system), respectively. By introducing the potential ϕ, we can write the electric field as $E = -\nabla\phi$. To get the electric field distribution through the medium, we firstly

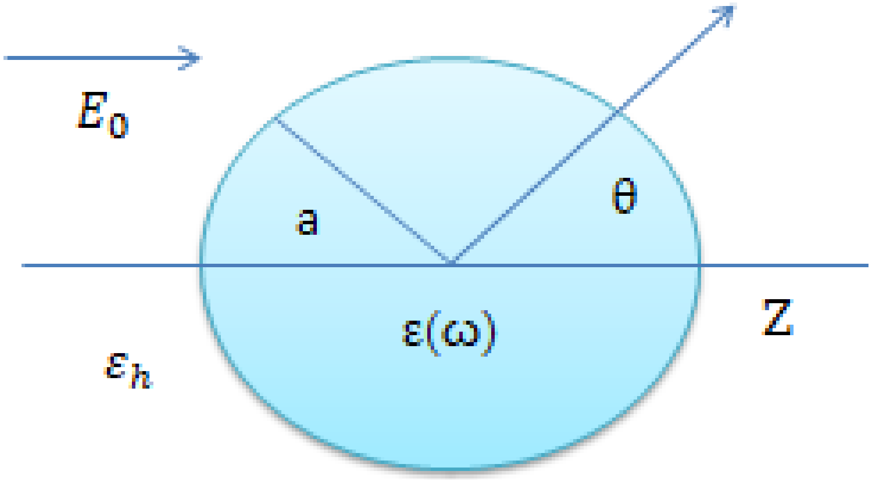

Figure 2.2: Homogeneous nano-sphere in electrostatic field.

need to get ϕ, which is the solution of Laplace equation

$$\nabla^2\phi = 0. \tag{2.4.4}$$

Assuming the given medium is a homogeneous and isotropic, thus it is symmetric in the azimuthal direction. The general solution is given by

$$\phi(r,\theta) = \sum_{l=0}^{\infty}[A_l r^l + B_l r^{-(l+1)}]P_l \cos(\theta). \tag{2.4.5}$$

In which P_l is the Legendre polynomials of the l^{th} order. First, let us determine the potential inside the sphere. When $r \to 0$, the potential should be finite. So, we obtain $B_l = 0$. The solution inside the spherical medium becomes

$$\phi_{in}(r,\theta) = \sum_{l=0}^{\infty} A_l r^l P_l \cos(\theta). \tag{2.4.6}$$

For the field outside the sphere at a distance $r >> a$, the term $B_l r^{-(l+1)} P_l \cos(\theta)$ in Eq. (2.4.5) is smaller enough to be omitted. We obtain

$$\phi_{out}(r, \theta) = \sum_{l=0}^{\infty} C_l r^l P_l \cos(\theta). \tag{2.4.7}$$

And from electrostatic field theory, we have

$$\phi_{out}|_{r \to \infty} \sim -E_0 r \cos\theta = -E_0 r P_l(\cos\theta). \tag{2.4.8}$$

Comparing Eq. (2.4.7) to Eq. (2.4.8), we obtain

$$C_1 = E_0, \quad C_l = 0. \quad (\text{for} \quad l \neq 0, 1) \tag{2.4.9}$$

The solution outside the spherical medium can be written as

$$\phi_{out} = C_0 - E_0 r P_l(\cos\theta) + \sum_{l=0}^{\infty} D_l r^{-(l+1)} P_l(\cos\theta). \tag{2.4.10}$$

The continuous of potential at the interface between the sphere and the surrounding medium demands

$$\phi_{in}|_{r=a} = \phi_{out}|_{r=a}. \tag{2.4.11}$$

Moreover, the continuous of normal component of displacement gives

$$\varepsilon_0 \varepsilon_h \frac{\partial \phi_{out}}{\partial r}|_{r=a} = \varepsilon_0 \varepsilon \frac{\partial \phi_{in}}{\partial r}|_{r=a}. \tag{2.4.12}$$

Substitution of Eq. (2.4.11) and (2.4.12) into Eq. (2.4.6), (2.4.10) and comparing the coefficient of the same order yields

$$\begin{cases} D_0 = 0 \\ C_0 = A_0 \end{cases} \qquad \begin{cases} A_1 = -\frac{3\varepsilon_h}{\varepsilon + 2\varepsilon_h} \\ C_1 = \frac{\varepsilon - \varepsilon_h}{\varepsilon + 2\varepsilon_h} a^3 E_0 \end{cases} \qquad \begin{cases} A_l = 0 \\ B_l = 0 \end{cases} \quad (l \neq 0, 1), \tag{2.4.13}$$

then the solution becomes

$$\begin{cases} \phi_{in} = A_0 - \frac{3\varepsilon_h}{\varepsilon + 2\varepsilon_h} E_0 r \cos\theta \\ \phi_{out} = A_0 - E_0 r \cos\theta + \frac{\varepsilon - \varepsilon_h}{\varepsilon + 2\varepsilon_h} a^3 E_0 r^{-2} \cos\theta. \end{cases} \tag{2.4.14}$$

By introducing dipole moment

$$\mathbf{p} = 4\pi\varepsilon_0\varepsilon_h a^3 \frac{\varepsilon - \varepsilon_h}{\varepsilon + 2\varepsilon_h} E_0, \tag{2.4.15}$$

the potential outside the sphere can be rewritten as

$$\phi_{out} = A_0 - E_0 r \cos\theta + \frac{\mathbf{p}.\mathbf{r}}{4\pi\varepsilon_0\varepsilon_h r^3}. \tag{2.4.16}$$

From the equations, we observe that the external applied field introduces a dipole moment inside a sphere of magnitude proportional to $|E_0|$. If we introduce the polarizability α into Eq. (2.4.15), rewritten as

$$\mathbf{p} = \varepsilon_0\varepsilon_h \alpha E_0, \tag{2.4.17}$$

yields

$$\alpha = 4\pi a^3 \frac{\varepsilon - \varepsilon_h}{\varepsilon + 2\varepsilon_h} = 3\frac{(\varepsilon - \varepsilon_h)}{\varepsilon + 2\varepsilon_h} V, \tag{2.4.18}$$

in which α describe the polarizability and V is the volume of the nano-sphere. It is apparent that the polarizability experiences a resonant enhancement under the condition that $|\varepsilon + 2\varepsilon_h|$ is a minimum, which for the case slowly tuning $Im(\varepsilon)$ around the resonance simplifies to

$$Re[\varepsilon] = -2\varepsilon_h. \tag{2.4.19}$$

The relationship is also called Frӧehlich condition [23] and the associate mode (in the oscillating field) is the dipole surface plasmon of the metal nanoparticle. Applying $E = -\nabla\phi$ on Eq. (2.4.14) gives us the electric field distribution

$$\begin{cases} E_{in} = \frac{3\varepsilon_h}{\varepsilon + 2\varepsilon_h} \\ E_{out} = E_0 + \frac{3r(p.r) - p}{4\pi\varepsilon_0\varepsilon_h}\frac{1}{r^3}. \end{cases} \tag{2.4.20}$$

The fields both inside and outside the spherical medium are enhanced due to the dipole resonance.

2.4.3 Spherical Particles - Mie Theory

Mie theory is analytical description of optical property of metallic nanoparticles. This is the simplest exact solution of Maxwell equations and original Mie formulation for an incident electromagnetic (EM) plane wave interacting with metallic sphere of a radius r embedded in a host medium. In 1908, Gustav Mie solved the Maxwell equations for the interaction of incident electromagnetic field with a metallic sphere using spherical polar coordinates [28]. The interaction of this EM wave with spherical nanoparticles produces scattering and absorption of incident plane wave. The Mie theory is used to calculate extinction cross-section for multipole oscillations. In the Mie theory, the scattering and extinction cross-sections are calculated by [29]:

$$\sigma_{ecs} = \frac{2\pi}{|k|^2} \sum_{n=1}^{\infty} (2n+1) Re(a_n + b_n), \tag{2.4.21}$$

$$\sigma_{scs} = \frac{2\pi}{|k|^2} \sum_{n=1}^{\infty} (2n+1)(|a_n|^2 + |b_n|^2), \tag{2.4.22}$$

with

$$a_n = \frac{m\psi_n(mx)\psi_n^{'}(x) - \psi_n^{'}(mx)\psi_n(x)}{m\psi_n(mx)\eta_n^{'}(x) - \psi_n^{'}(mx)\eta_n(x)}, \tag{2.4.23}$$

$$b_n = \frac{\psi_n(mx)\psi_n^{'}(x) - m\psi_n^{'}(mx)\psi_n(x)}{\psi_n(mx)\eta_n^{'}(x) - m\psi_n^{'}(mx)\eta_n(x)}, \tag{2.4.24}$$

where m is the ratio of refractive index of metallic sphere n and to that of host medium n_h, ψ_n and η_n are the Riccati and Bessel functions, the prime ($'$) indicates the first differentiation of Riccati and Bessel function with respect to the argument, and n is index of summation of partial waves ($n = 1$ for dipole oscillation, $n = 2$ for quadrupole oscillation, $n = 3$ for octupole, and so on).

2.4.4 Size Effects

Nanomaterials have unique properties due to its increase in the surface area to volume ratio and the quantum size effect. If the size of nanocomposite materials is smaller than their De-Broglie wavelength of electrons and holes are spatially confined, creating electric dipoles. Nano-sized materials have a probability of significant interface interaction, which strongly determines the properties like electrical resistivity, chemical reactivity, adhesion, and catalytic activity.

For instance, for very small metallic nanoparticles, the plasmonic properties are dependent on the radius r. The dielectric function Eq. (2.2.6) is dependent on the size of the material, and defined as [30, 31];

$$\varepsilon(\omega, r) = \varepsilon_\infty - \frac{\omega_p^2}{\omega(\omega + i\gamma(r))}. \tag{2.4.25}$$

The size dependent damping parameter can be expressed as;

$$\gamma(r) = \gamma_0 + A\frac{V_f}{r}, \tag{2.4.26}$$

where γ_0 is the bulk damping constant, V_f is the speed of electrons at Fermi energy surface and A is a parameter that depends on the specifics of the scattering process. The size dependent damping parameter highly determine the sharpness and broadness of optical absorbance of metallic nanoparticles as well as nanocomposite.

2.4.5 Ellipsoidal (Non-Spherical) Particles - Shape Effects

One of the main factors affecting the plasmonic properties of nanomaterial is shape. For instance, spherical nanomaterials has two plasmonic resonance associated with the interfaces, but, ellipsoidal nanoparticles possess more than two plasmonic resonances corresponding to the oscillation of electrons along the three axes and interfaces. These resonance wavelength depends on orientation of applied electric filed relative to the system. In these kinds of geometrical nanomaterials, plasmonic resonance frequency can be easily enhanced by changing axes length or eccentricity of the material. The high tunability of optical response of ellipsoidal nanoparticles have attracted the intense research interest due to their diverse application suites. In this geometry, the surface plasmon mode can be split into along the axes a, b and c (where $a > b > c$). Consider the area of the surface of an ellipsoid centered at the coordinate origin, with rectangular cartesian coordinate axes as shown in Fig. 2.3.

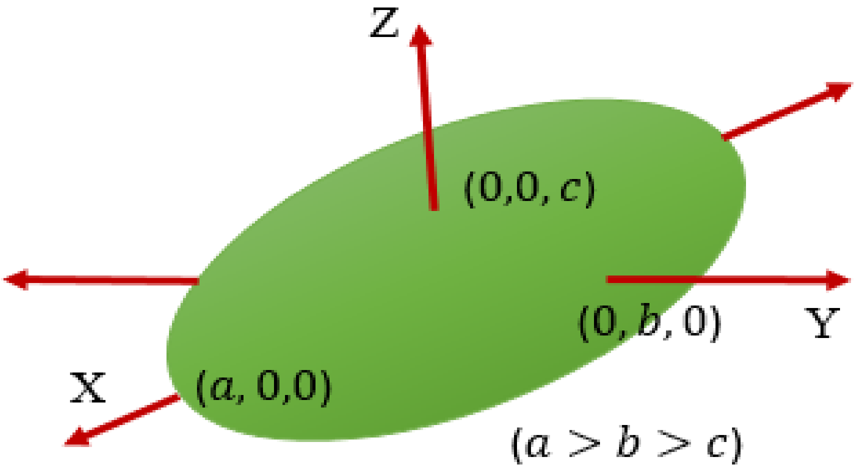

Figure 2.3: Schematic model of ellipsoidal particle.

$$\frac{X^2}{a^2} + \frac{Y^2}{b^2} + \frac{Z^2}{c^2} = 1. \tag{2.4.27}$$

The electric potential of confocal ellipsoidal nanoparticle subject to a uniform electric field is obtained with the help of ellipsoidal coordinates (ξ, η, ζ). To determine the dipole moment of the system in the quasi-static approximation, the surface area of ellipsoidal system is required. Therefore, the surface of an ellipsoid in ellipsoidal coordinates (ξ, η, ζ) is express as [32]:

$$\frac{X^2}{a^2+\xi}+\frac{Y^2+\xi}{b^2}+\frac{Z^2}{c^2+\xi}=1, \quad -c^2<\xi<\infty, \tag{2.4.28}$$

$$\frac{X^2}{a^2+\eta}+\frac{Y^2+\eta}{b^2}+\frac{Z^2}{c^2+\eta}=1, \quad -b^2<\eta<-c^2, \tag{2.4.29}$$

$$\frac{X^2}{a^2+\zeta}+\frac{Y^2+\zeta}{b^2}+\frac{Z^2}{c^2+\zeta}=1, \quad -a^2<\zeta<-b^2. \tag{2.4.30}$$

X,Y and Z in terms of the ellipsoidal cartesian coordinates (ξ, η, ζ) and semi-axes can be defined as:

$$X^2=\frac{(a^2+\xi)(a^2+\eta)(a^2+\zeta)}{(b^2-a^2)(c^2-a^2)}, \tag{2.4.31}$$

$$Y^2=\frac{(b^2+\xi)(b^2+\eta)(b^2+\zeta)}{(a^2-b^2)(c^2-b^2)}, \tag{2.4.32}$$

$$Z^2=\frac{(c^2+\xi)(c^2+\eta)(c^2+\zeta)}{(a^2-c^2)(b^2-c^2)}. \tag{2.4.33}$$

Consider a homogeneous ellipsoidal particle exposed to applied electric field along Z-axis, the potential Φ has symmetric properties as,

$$\Phi(X,Y,Z)=\Phi(-X,Y,Z)=\Phi(X,-Y,Z)=\Phi(-X,-Y,Z), \tag{2.4.34}$$

and

$$\Phi(X,Y,-Z)=\Phi(-X,Y,-Z)=\Phi(X,-Y,-Z)=\Phi(-X,-Y,-Z). \tag{2.4.35}$$

The potential inside the particle Φ_1 and potential outside the particle Φ_2 may be written as the superposition of the potential Φ_0 of the external field;

$$\Phi_0=-E_0Z=-E_0\left[\frac{(c^2+\xi)(c^2+\eta)(c^2+\zeta)}{(a^2-c^2)(b^2-c^2)}\right]^{1/2}, \tag{2.4.36}$$

and perturbing potential Φ_p caused by the particle. At sufficiently large distances from the particle the perturbing potential is negligible. We note that when $\xi \gg a^2$, then $\xi \simeq r^2$; therefore, we require that

$$\lim_{\xi \to \infty} \Phi_p = 0. \tag{2.4.37}$$

The potential is continuous across the surface of ellipsoidal particle and by using the boundary of the particle, the potential becomes:

$$\Phi_1(0, \eta, \zeta) = \Phi_0(0, \eta, \zeta) + \Phi_p(0, \eta, \zeta), \tag{2.4.38}$$

and the normal component is also continuous across the surface of the particle,

$$\varepsilon \frac{\partial \Phi_1}{\partial \xi} = \varepsilon_h \left[\frac{\partial \Phi_0}{\partial \xi} + \frac{\partial \Phi_p}{\partial \xi} \right], \tag{2.4.39}$$

where ε is the dielectric function ellipsoidal particle and ε_h is the dielectric function of host-medium. Applying Laplace equation and boundary equation stated above, we can obtain the following expressions:

$$\Phi_1 = \frac{\Phi_0}{1 + L_c \frac{(\varepsilon - \varepsilon_h)}{\varepsilon_h})}, \tag{2.4.40}$$

$$\Phi_p = \Phi_0 \frac{\frac{abc}{2} \frac{\varepsilon - \varepsilon_h}{\varepsilon_h} \int_\xi^\infty \frac{dq}{(c^2+q) f(q)}}{1 + L_c \frac{\varepsilon - \varepsilon_h}{\varepsilon_h}}, \tag{2.4.41}$$

where L_c is the depolarization or geometrical or shape factor is given as;

$$L_c = \frac{abc}{2} \int_0^\infty \frac{dq}{(c^2 + q) f(q)}, \tag{2.4.42}$$

and $f(q) = [(a^2 + q) + (b^2 + q) + (c^2 + q)]^{1/2}$. At large distance r from the origin, the potential Φ_p is given asymptotically by;

$$\Phi_p \sim \frac{E_0 cos\theta}{r^2} \frac{\frac{abc}{3} \frac{\varepsilon - \varepsilon_h}{\varepsilon_h}}{1 + L_c \frac{\varepsilon - \varepsilon_h}{\varepsilon_h}}, \quad (r \gg a) \tag{2.4.43}$$

From the relationship between potential and dipole moment, as written in Eq. (2.4.16), the dipole moment can also expressed as;

$$\mathbf{P} = 4\pi abc \frac{\varepsilon - \varepsilon_h}{3(\varepsilon_h + L_3(\varepsilon - \varepsilon_h))} E_0. \tag{2.4.44}$$

Therefore, the polarizability, α_c, of an ellipsoid in a field parallel to Z axis is

$$\alpha_c = 4\pi\varepsilon_h abc \frac{\varepsilon - \varepsilon_h}{3(\varepsilon_h + L_3(\varepsilon - \varepsilon_h))}. \tag{2.4.45}$$

The depolarization factor and polarizability for the remain axes (X and Y) have the same expression as Z. For the special class of ellipsoid; spheroids, which have two axes of equal length ($a > b = c$ for prolate spheroid and $a < b = c$ for oblate spheroid as shown in Fig. 2.4) and sphere ($a = b = c$), only one of the depolarization factor which is independent and all three depolarization factor are equal ($L_a = L_b = L_c = 1/3$), respectively. The depolarization factor of spheroidal nanoparticle is explicitly explained in Chapter 5.

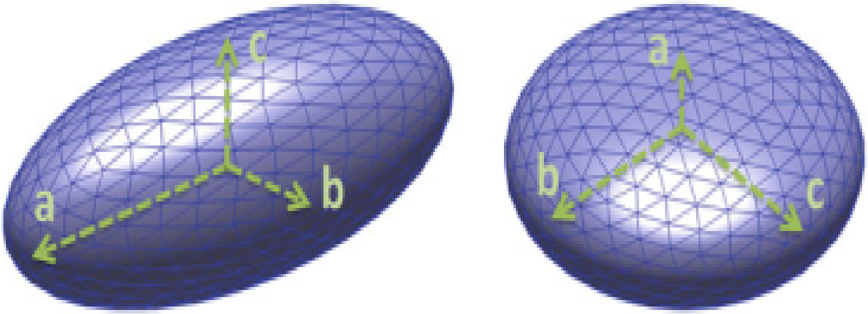

Figure 2.4: Schematic diagram of a spheroidal particle with dimensions (a, b, c), such as $a > b = c$ (prolate left) and $a < b = c$ (oblate right) [33].

2.5 Basic Principles and Mechanism of Photocatalysis

Photocatalysis is a unique process for remedying environmental and energy issue. The term ‘photocatalysis’ is composed from two words: ‘photo=light’ and ‘catalysis’. It also means that, in the presence of light and catalysis, the photocatalytic reaction is taking place on the surface of the catalyst. In terms of phase of reaction, the photocatalysis materials are classified into two: homogeneous photocatalysis in which reaction of photocatalytic takes place in a homogeneous phase and heterogeneous photocatalysis in which photocatalytic reaction takes place at their interface of two different phases or media.

Three main components which determine a photocatalytic reaction are, an emitted photon, a catalyst surface and an oxidizing agent. The photocatalytic process is instigated, when the incident photon energy is equal to or greater than the photocatalyst material’s band gap energy (E_g). When the photon energy interacts with material, electron-hole pairs are formed and they are used for oxidation and reduction process. Photocatalyst is an excellent technique which can be used for many applications such as production of hydrogen, antibacterial activity, purification of air, and degradation of organic pollutants in waste-water. After few decades, researchers give more attention for photocatalytic process in the field of waste-water treatment. Nowadays, the environment as well as aquatic body are polluted by industrial waste material. These polluted water by organic pollutants can be removed by heterogeneous photocatalysis which is a new promising alternative method. In waste-water treatment technology, the following important factors must be considered [34]:

- Flexibility of treatment

- Efficiency
- Recyclability
- Eco-friendliness and cost-effectiveness

Semiconductor material like ZnO, TiO_2, SnO_2, CeO_2, and bismuth oxyhalides are some examples of heterogeneous photocatalysis. The basic mechanisms of semiconductor based photocatalysis include;

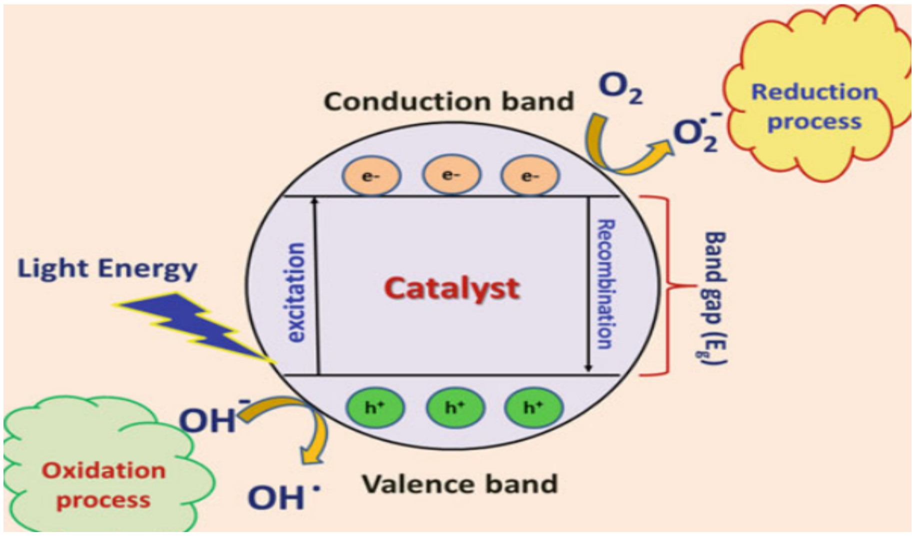

Figure 2.5: Schematic diagram of photocatalytic reaction mechanism.

- Photoabsorption in the catalyst material leading to an electronic transition from the valence band to the conduction band
- Valence band holes can oxidize donor molecules and react with water molecule to generate hydroxyl ($OH\bullet$) (strong oxidizing agent)

- Electrons in the conduction band react with dissolved oxygen species to form superoxide ions. These electrons induce the redox reactions.

The photocatalysis efficiency of materials is dependent on the following parameters crystal structure, size of the nanomaterial through quantum confinment effects, morphology and active area sites in the material, reaction temperature, light intensity, amount of waste-water, and concentration of catalysis material.

Chapter 3

Synthesis of Nanocomposites and Characterization Techniques

3.1 Introduction

Nano-synthesis is the production of novel nanomaterials with tunable properties for novel and diverse applications. Synthesis methods play a vital role in the development, modification and enhancement of their physical properties. Hence there is need to optimaze the size, surface topography and/or morphology of the nanomaterials. The synthesis method of nanomaterials are generally classified into two: bottom-up and top-down approach. Bottom-up or constructive method is the most preferable approach to synthesize nanomaterials from atom/molecule/cluster. Sol-gel, precipitation, hydrothermal, chemical vapor deposition, pyrolysis, and biosynthesis are the most commonly used bottom-up methods. Top-down or detractive method is the reduction of bulk materials using different techniques to nanometric scale material. Among these techniques are mechanical milling, laser ablation, thermal decomposition, and sputtering. The synthesis methods and their classification are summarized in Fig. 3.1. The geometry (morphology and size), elemental composition,

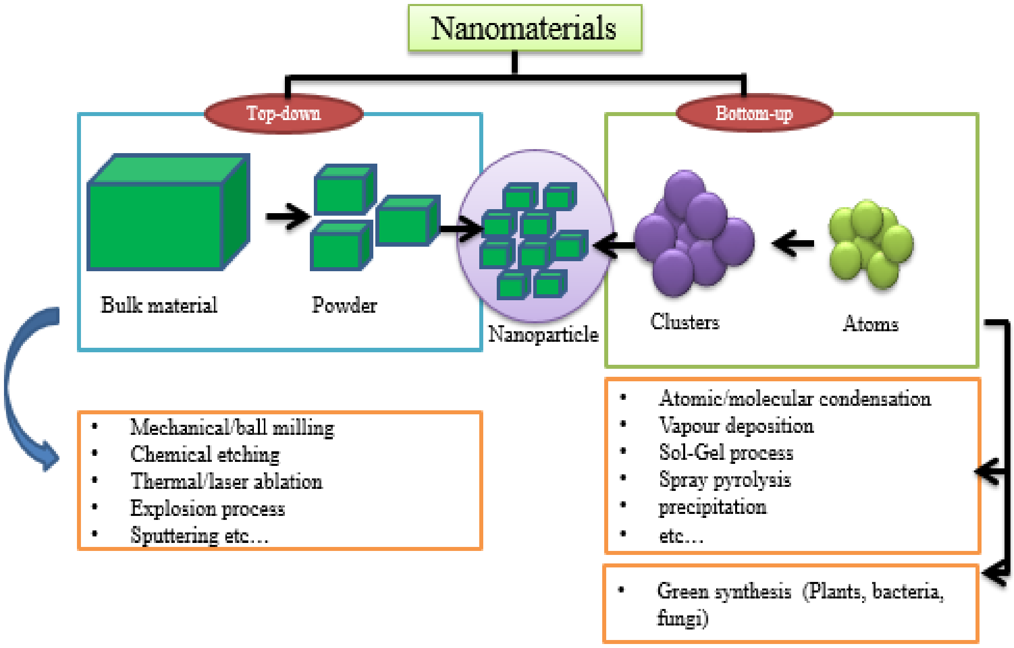

Figure 3.1: Illustration of the two types of synthesis processes and the suite of methods for fabricating nanoparticles.

surface charge, optical property, application, strength and stability, and crystallography of the synthesized nanomaterials are characterized by X-ray diffraction (XRD) spectroscopy, scanning electron microscope (SEM), transmission electron microscope (TEM), UV-Vis spectroscopy, Fourier transform infrared (FT-IR) spectroscopy, and X-ray photoelectron spectroscope (XPS).

3.2 Synthesis Methods

3.2.1 Sol-Gel Method

Sol-gel method (developed in the 1960s) is a process of formation of colloidal suspension (sol) and gelation of colloidal suspension to form a network in a continuous liquid phase (gel). The starting materials (precursors) are inorganic metal salts or metal organic compounds like, metal alkoxides [35]. The precursor should be added into water or dilute acid to form a dispersible oxide and forms a sol by shaking, stirring, or sonication [9]. The removal of liquid from the sol yields the gel, and the sol-gel transition through hydrolysis and condensation controls the synthesized size, shape, porosity, and high surface area for catalyst supports. The separation of the liquid solution from the sol and the subsequent drying leads to the formation of a gel which is calcined to form the oxide nanoparticle. The sol-gel method is mostly preferred due to its low processing cost, simplicity, energy efficiency, high production rate and rapid productivity of fine homogeneous powder.

3.2.2 Rapid Synthesis Method

Rapid synthesis method is a new method to synthesize nanoparticles using heat. When the precursor is placed in furnace within sufficient temperature, the precursor is decomposed into the final product. The other constituents of the precursor are decomposed into a gaseous form. As the name indicates, this method is very fast, we can get the sample within less than half a day. To synthesize samples, a certain gram of precursor is placed in the furnace and set the required temperature to decompose. Different morphology and size can be prepared only by varying two factors: calcination time and/or calcination temperature.

3.2.3 Green Synthesis Method

Green synthesis method is an environmental eco-friendly approach for the synthesis of non-toxic and biodegradable nanomaterials. This method is easy to handle, cost-effective, reliable, and environment-sustaining. The solution is extracted from different plants part (root, leaf, stem, fruit, seed), vegetable, enzyme, algae, fungi [2]. After collecting the required amount, the extraction solution is prepared in different ways. For instance with regards to plant leaf, (1) the leaves are washed by pure water to remove dust or organic materials from it's surface, (2) cut/grind into small pieces after/before dried, (3) the pieces macerated or boiled in water/methanol or in other solvent for the required time/day, (4) finally the extract solution is separated by using filtration technique. A certain amount (concentration) of extracted solution is then used for the synthesis of nanomaterials.

3.3 Characterization Techniques

Several characterization techniques were used to investigate the structural, optical, catalytic, magnetic, electronic properties of the sample in this work. The principles and properties that are investigated using these characterization tools will be discussed in detail in the subsequent sections.

3.3.1 X-ray Diffraction (XRD)

X-ray diffraction (XRD) is one of the most extensively used technique for the characterization of the crystal structure and microstructure of synthesized nanomaterials. XRD relies on the probing of the regular arrangment of atoms with a grain or crystal in a solid by X-ray scattering by their electron densities. Up to 1895, the study of matter at the atomic level was a difficult task but the discovery of electromagnetic radiation with $1\mathring{A}$ ($10^{-10}m$) wavelength, also known as X-ray radiation enabled the study of materials using diffraction at such length scales. As the atomic distance in matter is comparable with the wavelength of X-ray, the phenomenon of diffraction find its way through it and gives many profitable results related to the crystalline structure. X-ray diffraction (XRD) is a versatile, non-destructive technique used for qualitative and quantitative analysis of a crystalline materials.

X-ray diffraction has also been used to determine the phase of nanomaterials through determination of the lattice constants, grain sizes, dislocation lengths, phase matching in unknown materials, stress, texture and orientation of single crystals amongst other physical properties. In this way the technique can provide information on the phase purity, crystal quality and texture or preferred orientations in select forms of materials (thin film, bulk and powder). In addition, the diffraction pattern also provides information regarding the types of phases present in the polycrystalline material and can be used to calculate the approximate average grain size using Scherrers equation given by the expression [10, 36].

$$D = \frac{0.9\lambda}{\beta \cos\theta}, \tag{3.3.1}$$

where λ is the wavelength of incident X-ray beam ($\sim 1.54\mathring{A}$ for $Cu\ K\alpha$), β full width at half maximum in radians of the peak, D is the particle and crystalline size, and θ is the Bragg's diffraction angle (scattering angle) in degrees.

X-rays are short-wavelength, high energy electromagnetic radiation, having the properties of both waves and particles. They can be described in terms of both photon energy (E) or wavelength, λ (the distance between peaks) and frequency ν (the number of peaks passing a point in a unit of time). The relation between energy, frequency or wavelength in the case of photon is:

$$E = h\nu = \frac{hc}{\lambda}. \tag{3.3.2}$$

By rearranging the above equation Eq. (3.3.2) and substitute the values of the constants, which yields the following relationship.

$$\lambda = \frac{1240(eV)}{E}. \tag{3.3.3}$$

Bragg's Law

The atoms in crystals interact with X-rays through scattering of the X-rays by the electrons of the atoms in the crystal at two lattice spacings to produce constructive interference leading to a peak or destructive interference leading to no peak at all. The interaction can be thought of as if the atoms in a crystal structure reflect the waves. But, because a crystal structure consists of an orderly arrangement of atoms, the reflections occur from the atomic planes. Consider a beam of monochromatic X-rays entering a crystal with one of its planes oriented at an angle of θ to the incoming beam. Figure 3.2. shows two such X-rays, where the spacing between the atomic planes occurs over the distance, d.

The first ray scatters off at the upper atomic plane at an angle θ equal to its angle of incidence. Similarly, the second ray is scattered off at the lower place in the same geometrical condition, (θ). While second ray is in the crystal, however, it travels a distance of $2a$ farther than first ray. If this distance $2a$ is equal to an integral number of wavelengths $(n\lambda)$, then the first and second rays will be in phase on their exit from the crystal and constructive interference will occur. If the distance $2a$ is not an integral number of wavelengths, then destructive interference will occur and the

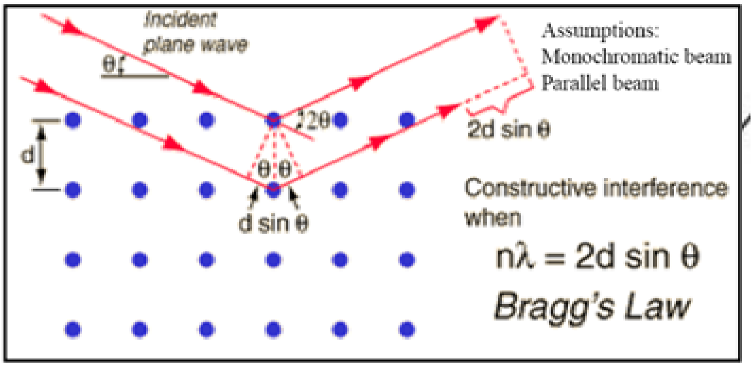

Figure 3.2: A schematic diagram of Braggs reflection from the crystal .

waves will not be as strong as when they entered the crystal. Thus, the condition for constructive interference to occur is

$$n\lambda = 2a. \tag{3.3.4}$$

But, from trigonometry, we can figure out what the distance $2a$ is in terms of the spacing, d, between the atomic planes.

$$a = d\sin\theta, \tag{3.3.5}$$

and

$$n\lambda = 2d\sin\theta. \tag{3.3.6}$$

This is known as Braggs Law for X-ray diffraction.

The diffracted X-rays are then detected, processed and counted. And by scanning the sample through a range of 2θ angles, all possible diffraction directions of the lattice are attained for a polycrystalline samples with randomly oriented grains such as a powder or thin film.

3.3.2 Scanning Electron Microscope (SEM)

Scanning electron microscope (SEM) is used to investigate the shape and morphology of nanomaterials. SEM uses a focused beam of high-energy electrons to generate a variety of signals at the surface of a sample. The primary beam of electrons from an electron source is collimated by the first and second electromagnetic condenser lenses and focused onto the sample surface by the sequential objective lens. The scanning coil is used to move the beam across the sample surface through Coulombic interaction. Accelerated electrons using different components, carry kinetic energy, and this energy is dissipated as a variety of signals produced by electrons and atoms on the surface or a various depth on the sample. The signals from the sample when

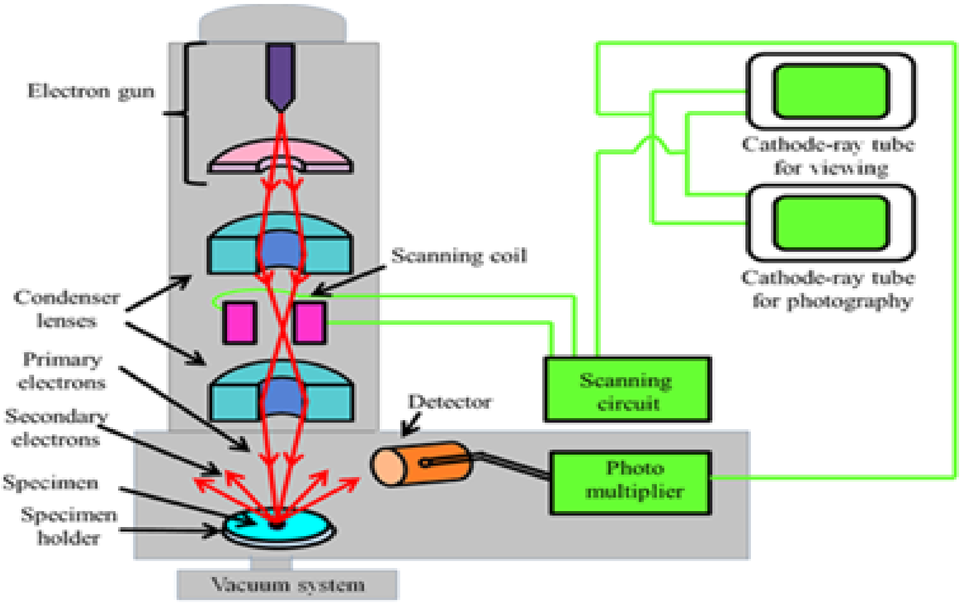

Figure 3.3: A schematic diagram of scanning electron microscope (SEM) .

incident electron interact with solid sample, provide the following information about the samples; external morphology, chemical composition, and crystal structure and orientation. These signals include secondary electrons (SE), backscattered electrons (BSE), diffracted backscattered electrons (DBSE: used to determine crystal structures and orientations), and characteristics X-rays for elemental analysis. The secondary electrons are detected by a scintillation detector that produces flashes of light upon electron impingement. The light flashes are then detected and amplified by a photomultiplier tube. Secondary electrons and backscattered electrons are commonly used for SEM imaging samples. Secondary electrons are most valuable for showing morphology and topography on samples and backscattered electrons are most valuable for illustrating contrasts in composition in multiphase samples [37]. Depending on the powder sample and the device setup, the contrast in the final image provides

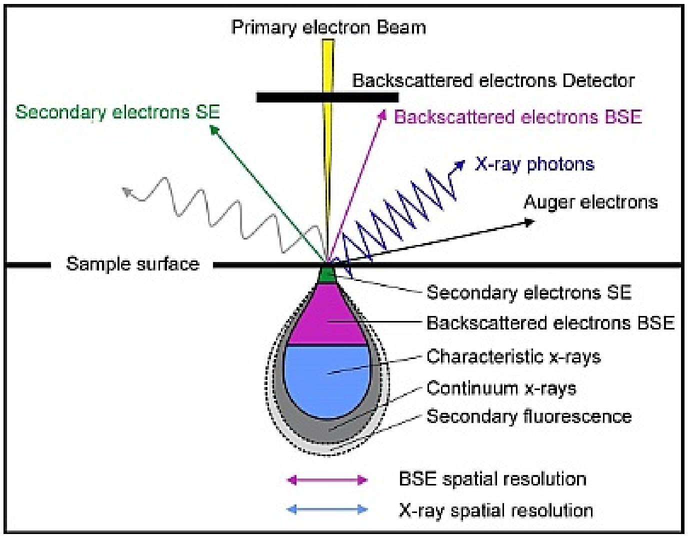

Figure 3.4: The interaction of electron with the sample in different depth and the signal after interaction .

information on the sample composition, topography and morphology. In most applications, data are collected over a selected area of the surface of the sample, and a 2D image is generated that displays spatial variations in these properties. Areas ranging from approximately 1 cm to 5 microns in width can be imaged in a scanning mode using conventional SEM techniques (magnification ranging from 20X to approximately 30,000X, spatial resolution of 50 to 100 nm). The SEM is routinely used to generate high-resolution images of shapes of objects. It is also widely used to identify phases based on qualitative chemical analysis and/or crystalline structure .

3.3.3 Transmission Electron Microscope (TEM)

Transmission electron microscope (TEM) is a high resolution electron microscope used to investigate particle size, shape and morphology [38] with a highly-magnified image. TEM can magnify images up to million times. TEM is an imaging techniques where an energetic beam of electrons are focused onto the sample by means of a high voltage to create a highly magnified image. TEM has electron gun at the top which emits electron beam that traverses through the microscope's tube and focus it on the sample. Electron gun (electron source) consists of positive potential (anode) and negative potential (cathode). The electrons are confined by a negative cathode and emit electrons when heated. Then, the released electron beam is accelerated by the positive anode towards the specimen.

The released electrons are focused into the target using the metal apertures and a series of electromagnetic lenses. The electrons in the beam have their own small energy. In coming electron beam is restricted and filtered out unwanted beam before interacting with the specimen. .

The imaging device is composed of another set of electromagnetic lenses and a screen.

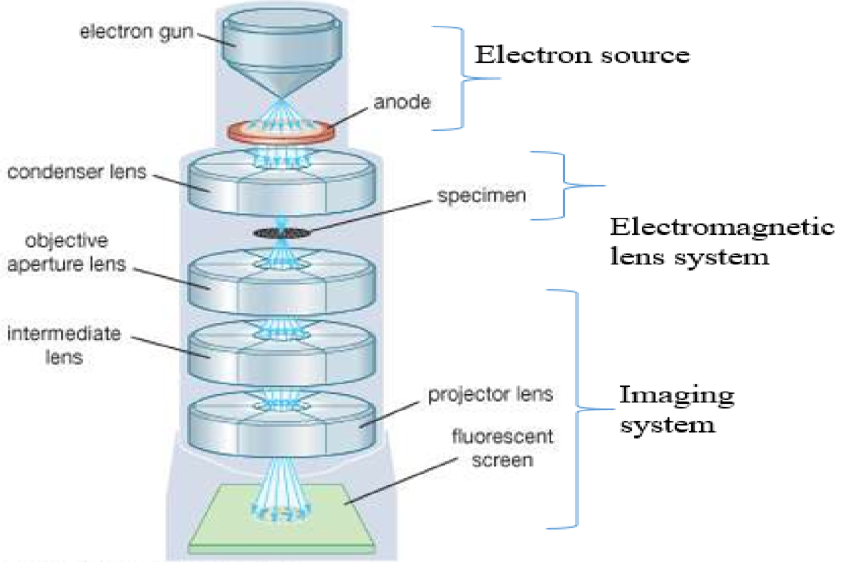

Figure 3.5: Simplified diagram of transmission electron microscope.

The electromagnetic lens system requires two lens systems, one to refocus the electrons after passing through the specimen, and the other to magnify the image and project it onto a screen as an image. The computer has a phosphorescent plate that glows when electrons hit it. The process of image formation is akin to photography since the projected image is legible and must have high resolution due to the monochromatic nature of the electron source.

The image formed is monochromatic and must be visible to the eye either by allowing the electrons to fall on a fluorescent screen at the base of the microscope column or by digitally recording the image for viewing on a computer screen.

3.3.4 X-Ray Photoelectron Spectroscopy (XPS)

X-ray photoelectron spectroscope (XPS) is very important spectroscopy tool, commonly used for investigating the elemental composition, electronic structure and oxidation state of nanoscale materials [32] based on the photoelectric effect. It is used to investigate the energy distribution of the emitted electrons at surface of the sample. When the higher enough X-ray photon energy is absorbed by a core electron, the electron is emitted from the atom of the sample a certain kinetic energy. The emitted electron is also known as the known as photo-electron. Simultaneously, amount of electrons released from the sample and their kinetic energy are measured by the electron energy analyzer as shown in Fig. 3.6.

XPS provides information on the binding energy of each emitted electron as estimated from the equation;

$$E_{BE} = E_{ph} - (E_{KE} + E_{SP}), \tag{3.3.7}$$

$$E_{KE} = h\nu - E_{BE} - E_{SP}, \tag{3.3.8}$$

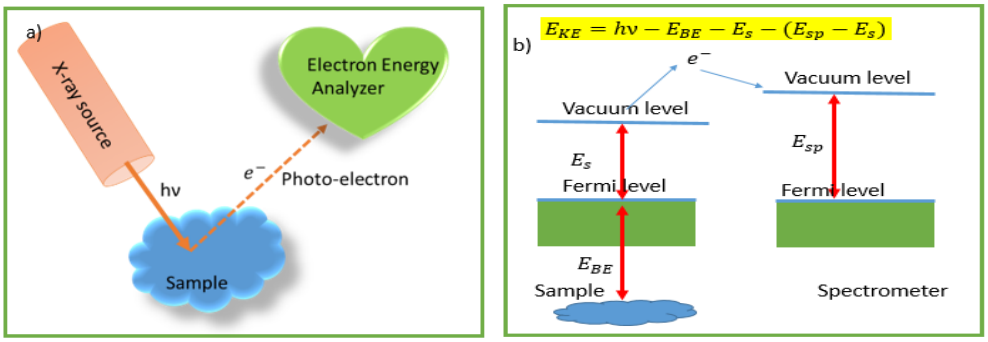

Figure 3.6: Schematic diagram of working principle of X-ray photoelectron spectroscopy (a) and schematic diagram of binding energy (b).

where E_{BE} is the binding energy of the atomic orbital from which the electron originates, E_{ph} is the energy of the X-ray photons being used, E_{KE} is the measured kinetic energy of the emitted electron and E_{SP} is the work function of spectrometer. The XPS spectrum describes the number of detected electrons as a function of binding energy. Each elements produce a set of XPS peaks associated with the detected electrons at a specific characterization binding energy values. Additionally the analysis of the concentration of the elements and their binding energies can be used to determine the charge sate of materials.

3.3.5 UV-Visible Spectroscopy

An instrument used in the ultraviolet-visible spectroscopy is called UV-Vis spectrophotometer. In a standard UV-Vis spectrophotometer, a beam of light is split; one half of the beam (the sample beam) is directed through a transparent cell containing a solution of the compound being analyzed, and one half (the reference beam) is directed through an identical cell that does not contain the compound but contains the solvent. The instrument is designed to use a dual beam method to measure the coincidence of the reference and sample beams by scanning their intensities with a grating over the desired wavelengths of interest. If the compound absorbs light at a particular wavelength, the intensity of the sample beam (IS) will be less than that of the reference beam [40]. This method conforms to the principle of conservation of energy, since the transmissivity (T), absorbance (A), scattering (S) and reflection (R) all contribute additively to the incident beam according to the expression;

$$1 = T + A + S + R \tag{3.3.9}$$

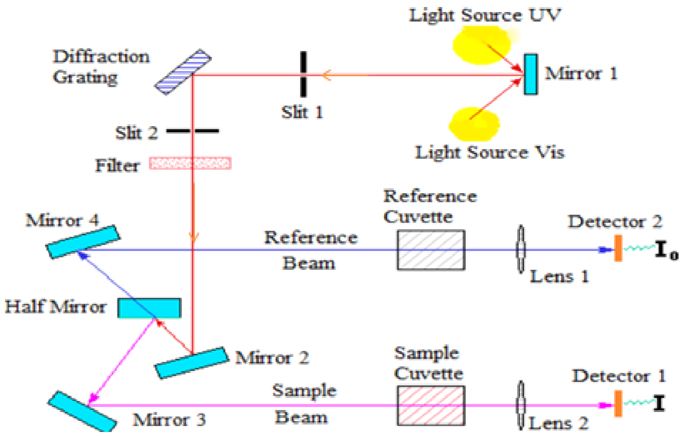

Figure 3.7: Interaction of reference and sample beam from UV-Vis source with sample cuvette and reference cuvette and the compression of their intensities.

The strength of each component is determined by the dielectric function of the material.

Absorption of radiation by a sample is measured at various wavelengths and plotted by a recorder to give the spectrum. The spectrum of absorbance and transmittance is a dispersion of the intensities of each component at all wavelength range of the instrument. The absorption intensity of light (I) depends on the absorption coefficient (α), thickness of the sample (t), and wavelength (λ).

$$I = I_0 exp(-\alpha t) = I_0 exp\left(-\frac{4\pi kt}{\lambda}\right), \tag{3.3.10}$$

where I_0 is the intensity before interaction, $\alpha = \frac{4\pi k}{\lambda}$ and k is extinction coefficient. And the band gap of the sample can be obtained by plotting the graph between ($\alpha h\nu$ versus $h\nu$) and extrapolating it along $h\nu$-axis [41], where ν is the frequency and α is the optical absorption coefficient.

Ultraviolet and visible spectrometry is almost entirely used for quantitative analysis; that is, the estimation of the amount of a compound known to be present in the sample.

3.3.6 Fourier Transform Infrared (FT-IR) Spectroscopy

In the region of longer wavelength or low frequency the identification of different types of chemicals is possible by of infrared spectroscopy and the instrument required for its execution is FT-IR spectrometer. The spectroscopy is based primarily on the assumption that molecules absorb different frequencies typical of their structure, called resonant frequencies, i.e., the frequency of the absorbed radiation matches the frequency of the vibrating bond or group. And the detection of energy is done on the basis of shape of the molecular potential energy surfaces, the masses of the atoms, and the associated vibronic coupling. Because each individual material is a unique mixture of atoms, no two materials create the exact same spectrum of infrared. Therefore, infrared spectroscopy can result in a positive identification (qualitative analysis) of every different kind of materials.

In addition, the size of the peaks in the spectrum is a direct indication of the amount of material present. FT-IR can be used to analyze a wide range of materials in bulk or thin films, liquids, solids, pastes, powders, fibers, and other forms. FT-IR analysis can give not only qualitative (identification) analysis of materials, but with relevant standards, can be used for quantitative (amount) analysis. FT-IR can be used to analyze samples up to $\sim$11 mm in diameter, and either measure in bulk or the top $\sim$1 μm layer. FT-IR spectra of pure compounds are generally so unique that they are like a molecular fingerprint.

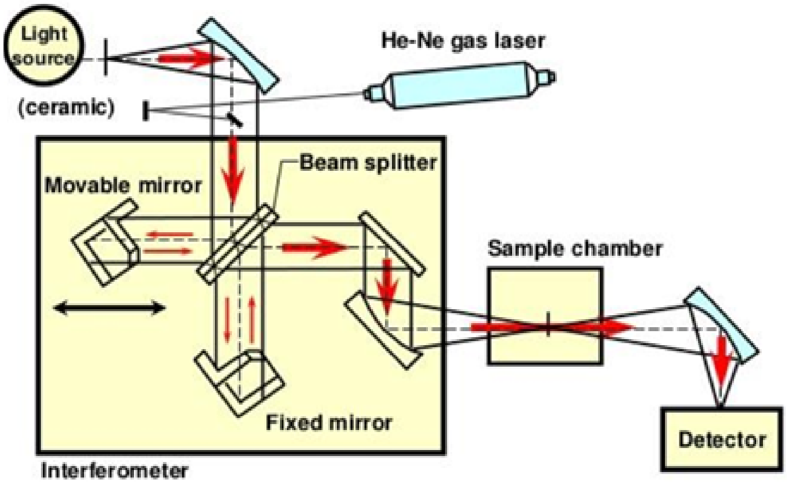

Figure 3.8: A schematic diagram of interaction of light source and laser with the sample in FT-IR spectroscopy.

Chapter 4

Size Dependent Optical Properties of $ZnO@Ag$ Core-Shell Spherical Nanostructures

4.1 Introduction

Zinc-oxide (ZnO) is a direct band gap of semiconductor. The Wurtzite ZnO has wide band gap (3.37 eV), high exciton binding energy ($\sim 60\ meV$) at room temperature, and high dielectric constant. These bulk material properties enable ZnO find utility in various applications including in the fabrication of electronic and optical devices such as UV/blue lasers [42]. However, compared to their bulk counterparts, ZnO nanoparticles (NPs) exhibit significantly different optical, electrical, and physical properties, which can be controlled simply by varying their size ($0D$, $1D$, $2D$ and $3D$) and/or shape [43]. Due to these size and shape tunability, ZnO NPs have attracted great interest for a diverse potential applications in optoelectronics devices such as sensors, light emitting diodes (LED), diode lasers, as electrodes or electron transport layers, and photovoltaic cells [44, 45].

Furthermore, NPs coated with a noble metal exhibit strong coupling between the plasmon resonance of the metal and the quantum size effect of the NPs that give rise to new properties [43]. In particular, core-shell nanostructure (CSNS) composites with metal-oxide core and metallic shell have several unique optical, photocatalytic, and electronic properties neither shown by the bare metal nor by metal-oxide nanostructures [46]-[48]. Their physical and chemical properties can be tuned by varying the size of the core and/or the thickness of the shell. Besides their unique electrical and optical properties, noble metals like Ag, Au, and Pt are preferred as a shell material because of their high chemical stability, bio-affinity, strong absorption of light. ZnO/Ag and ZnO/Au core-shell nanocomposites have been utilized in a wide range of applications such as photovoltaics, light emitting diodes (LED), photocatalysis, photodetectors, sensors, and also have fascinating properties such as transparent conduction, resistive switching, and biophysical functionalities [46, 49].

The fabrication of core-shell nanostructure needs a careful selection of both the core and shell material in order to optimize the passivation and to reduce the structural defects induced by positive mismatch of their lattice parameters [46]. The properties of core-shell nanostructure (CSNS) materials depend on the compositions and arrangements of both components present in the materials [50] as well as local environment [51]. Recently, new variety of CSNSs which integrate inorganic NPs with metal-organic frameworks (MOFs) into $NP@MOF$ core-shell NSs has been demonstrated [52]-[54]. This newly introduced technique of coating inorganic NPs with MOF shells is expected to provide the core NPs with high stability and additional functionalities [52, 53]. In inorganic core-shell nanocomposites, silver with thicknesses ranging between 5 and 10 nm is selected as a shell material for many applications [55] of ZnO nanosphere or nanodot due to its non-toxicity, strong absorption in/near visible spectrum [56] and surface plasmon resonance [57, 58].

In this chapter, we studied the size dependent optical properties of an ensemble consisting of spherical core-shell $ZnO@Ag$ nanoparticles embedded in a dielectric host matrix. The core size and the thickness of the metallic shell are varied, simultaneously. The polarizability, refractive index, and optical absorbance of the composite are theoretically and numerically investigated. The analysis is carried out by employing the electrostatic approximation to determine the distribution of the electric potential in the various regions of the NPs and the Maxwell-Garnet mixing formula to determine the effective permittivity of the ensemble (i.e., core-shell structure embedded in a dielectric medium).

4.2 Model of Core-Shell Nanostructure

Consider a spherical core-shell composite nanoparticle (NP) consisting of a semiconductor core of dielectric function (DF) ε_1 and a metallic shell of DF ε_2 embedded in a dielectric host matrix, as shown in Fig. 4.1. The host medium is assumed to be isotropic and non-absorbing with dielectric constant ε_3. The parameters a_1 and a_2 are the radii of the core and core-shell NP, respectively. When an electromagnetic wave is incident on the composite core-shell NP, electric field is induced in the system due to polarization. For NPs of (diameter $= 2a_2$) much less than the wavelength of the incident light, the distribution of the electrostatic potential Φ associated with the induced field can be obtained by solving the Laplace equation, $\nabla^2\Phi = 0$.

Suppose a uniform, static electromagnetic field polarized along the z-axis is applied on the spherical core-shell NP embedded in a host matrix. If the center of the NP is assumed to coincide with the origin of a spherical coordinate system, then the

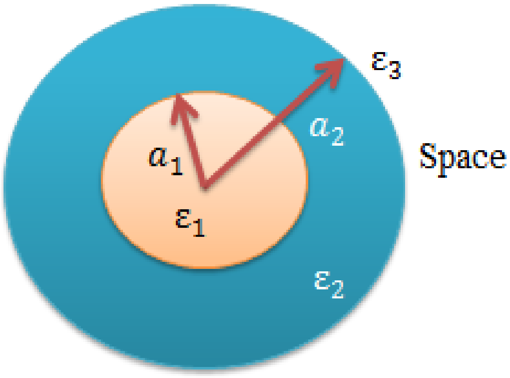

Figure 4.1: The schematic diagram of $ZnO@Ag$ spherical core-shell nanostructure with dielectric function of ZnO,ε_1 and Ag, ε_2.

distribution of the electric potentials in the system using Eq. (2.4.5) may be found to be:

$$\Phi_1(r,\theta) = A_1 r\cos\theta, \qquad r < a_1 \tag{4.2.1}$$

$$\Phi_2(r,\theta) = \left(A_2 r + \frac{B_1}{r^2}\right)\cos\theta, \qquad a_1 < r < a_2 \tag{4.2.2}$$

$$\Phi_3(r,\theta) = \left(A_3 r + \frac{B_2}{r^2}\right)\cos\theta. \qquad r > a_2 \tag{4.2.3}$$

where Φ_1, Φ_2, and Φ_3 are the electric potentials in the dielectric core, metal shell, and host matrix, respectively, A_3 is a quantity associated with the external applied field, r is the distance from the center of the NP, θ is the zenith angle, and the coefficients A_1, A_2, B_1, and B_2 are constants to be determined by using the appropriate boundary conditions at the interfaces.

It is worthwhile to note that the second term on the right-side of Eq. (4.2.3) represents the induced potential outside the core-shell NP. The optical properties of the system may readily be described by the induced field outside the concentric spheres.

Consequently, it is suffice to determine the value of the coefficient B_2. Imposing the relevant boundary conditions in Eqs. (4.2.1)-(4.2.3), we obtain the following relation:

$$B_2 = \left[\frac{(\varepsilon_1 + 2\varepsilon_2)(\varepsilon_2 - \varepsilon_3) + v_f(\varepsilon_1 - \varepsilon_2)(2\varepsilon_2 + \varepsilon_3)}{(\varepsilon_1 + 2\varepsilon_2)(\varepsilon_2 + 2\varepsilon_3) + 2v_f(\varepsilon_1 - \varepsilon_2)(\varepsilon_2 - \varepsilon_3)}\right] A_3 a_2^3, \tag{4.2.4}$$

where $v_f = (a_1/a_2)^3$.

In view of Eq. (4.2.3), the induced potential outside the concentric spheres is then given by

$$\Phi_{ind} = \frac{B_2}{r^2}\cos\theta. \tag{4.2.5}$$

Moreover, employing the dipole approximation, the induced potential may be expressed as [59]

$$\Phi_{ind} = \frac{p\cos\theta}{4\pi\varepsilon_3 r^2}. \tag{4.2.6}$$

where p is the electric dipole moment of the system. In view of Eqs. (4.2.5) and (4.2.6), the dipole moment becomes

$$p = 4\pi\varepsilon_3 B_2 = \varepsilon_3 \alpha A_3, \tag{4.2.7}$$

where α is the polarizability of the composite given by

$$\alpha = 4\pi\left[\frac{(\varepsilon_1 + 2\varepsilon_2)(\varepsilon_2 - \varepsilon_3) + v_f(\varepsilon_1 - \varepsilon_2)(2\varepsilon_2 + \varepsilon_3)}{(\varepsilon_1 + 2\varepsilon_2)(\varepsilon_2 + 2\varepsilon_3) + 2v_f(\varepsilon_1 - \varepsilon_2)(\varepsilon_2 - \varepsilon_3)}\right] a_2^3. \tag{4.2.8}$$

Further, the polarizability of an equivalent sphere of effective DF ε_I embedded in a host matrix of DF ε_3 can be expressed in the form of the Clausius-Mossotti relation [60, 61]. That is, which is similar to Eq. (2.4.18),

$$\alpha = 4\pi a_2^3 \frac{\varepsilon_I - \varepsilon_3}{\varepsilon_I + 2\varepsilon_3}, \tag{4.2.9}$$

after equating Eqs. (4.2.8) and (4.2.9) and simplifying, we get the effective DF of the core-shell spherical inclusion to be

$$\varepsilon_I = \varepsilon_2 \frac{(\varepsilon_1 + 2\varepsilon_2) + 2(\varepsilon_1 - \varepsilon_2)v_f}{(\varepsilon_1 + 2\varepsilon_2) - (\varepsilon_1 - \varepsilon_2)v_f}. \tag{4.2.10}$$

Introducing the volume fraction (β) of a spherical core-shell nanostructure by

$$\beta = 1 - \left(\frac{a_1}{a_2}\right)^3, \tag{4.2.11}$$

the effective DF of the composite, Eq. (4.2.10), may be rewritten as

$$\varepsilon_I = \varepsilon_2 \frac{\varepsilon_1(3/\beta - 2) + 2\varepsilon_2}{\varepsilon_1 + \varepsilon_2(3/\beta - 1)}. \tag{4.2.12}$$

Next, we consider an ensemble where identical spherical core-shell NPs (nanoinclusions) are homogeneously dispersed in a continuous host matrix of DF, ε_3. The polarizability and effective permittivity of the system may be described by using the Clausius-Mossotti relation together with the Maxwell-Garnett mixing theory. If N denotes the density number of the inclusions/scatteres in the system, then the polarizability expressed in terms of the permittivity becomes [62]

$$\frac{N\alpha}{3} = \frac{\varepsilon_{eff} - \varepsilon_3}{\varepsilon_{eff} + 2\varepsilon_3}, \tag{4.2.13}$$

where ε_{eff} is the effective DF of the system (ensemble) and α is the polarizability defined by Eq. (4.2.9). Equation (4.2.9) may conveniently be rewritten as $\alpha = 4\pi a_2^3 \eta$, where η is the dimensionless polarizability defined by

$$\eta = \frac{\varepsilon_I - \varepsilon_3}{\varepsilon_I + 2\varepsilon_3}. \tag{4.2.14}$$

Substitute Eq. (4.2.12) into (4.2.14) and rearranging, we find that

$$\eta = 1 - \frac{3}{2}\left[\frac{\varepsilon_2\varepsilon_3(3/\beta - 1) + \varepsilon_1\varepsilon_3}{\varepsilon_2^2 + \varepsilon_1\varepsilon_2[3/(2\beta) - 1] + \varepsilon_2\varepsilon_3(3/\beta - 1) + \varepsilon_1\varepsilon_3}\right]. \tag{4.2.15}$$

Furthermore, the effective permittivity of the ensemble may be obtained by substituting Eqs. (4.2.9) and (4.2.14) into (4.2.13). That is,

$$\varepsilon_{eff} = \varepsilon_3 \left(\frac{1 + 2\xi\eta}{1 - \xi\eta} \right), \tag{4.2.16}$$

which is similar with that obtained in Ref. [63]. Here, ξ is the filling factor of the inclusion given by

$$\xi = N \frac{4\pi a_2^3}{3}. \tag{4.2.17}$$

It is worthwhile to note that Eqs. (4.2.15) and (4.2.16) are general expressions for any two-layered spherical core-shell composite NPs that are embedded in a dielectric host matrix, regardless of whether the core-shell composites are metals, semiconductors/dielectric or a combination.

4.3 Numerical Analysis

For numerical evaluation, we considered an ensemble that consists of spherical $ZnO@Ag$ core-shell quantum dots dispersed in vacuum ($\varepsilon_3 = 1$). In the frequency domain of interest, we assumed that the DF of the ZnO core to be real, constant and independent of frequency. In addition, the DF of the silver shell is chosen to be of the modified Drude form that takes into account its nano-size. That is,

$$\varepsilon_2(\omega) = \varepsilon_\infty - \frac{\omega_p^2}{\omega(\omega + i\Gamma(l_e))}, \tag{4.3.1}$$

where ε_∞ is the permittivity at high frequencies, ω_p is the plasma frequency, $\Gamma(l_e)$ is the size dependent electron collision frequency, and ω is the frequency of the incident radiation. The size dependent damping parameter for silver can be expressed as [64, 65]

$$\Gamma(l_e) = \Gamma_0 + A \frac{V_f}{l_e}. \tag{4.3.2}$$

where $\Gamma_0 = 1.67 \times 10^{13}\ rad/s$ is the bulk damping constant describing bulk dissipative losses, $V_f = 1.39 \times 10^6\ m/s$ is the velocity of electrons at the fermi energy and $A = 1$ is a constant that accounts for the details of the electron scattering process [66, 67]. l_e is the effective mean free path for NPs of core radius a_1 and core-shell radius a_2 given by [68, 69]

$$l_e = \frac{a_2}{2}[(1 - v_f^{1/3})(1 - v_f^{2/3})]^{1/3}. \tag{4.3.3}$$

Further, separating Eq. (4.3.1) into real and imaginary, we have

$$\varepsilon_2(\omega) = \varepsilon_2^{'}(\omega) + i\varepsilon_2^{''}(\omega), \tag{4.3.4}$$

where

$$\varepsilon_2^{'} = \varepsilon_\infty - \frac{1}{z^2 + \rho^2}, \quad \text{and} \quad \varepsilon_2^{''} = \frac{\rho}{z(z^2 + \rho^2)}, \tag{4.3.5}$$

with $z = \omega/\omega_p$ and $\rho = \Gamma(l_e)/\omega_p$.

4.4 Results and Discussion

4.4.1 Polarizability

Since the permittivity (ε_2) is complex, the electric polarizability is also a complex function of the frequency ω. That is,

$$\eta = \eta^{'} + i\eta^{''}, \tag{4.4.1}$$

where $\eta^{'}$ is the real part and $\eta^{''}$ imaginary part. Substituting Eq. (4.3.4) into (4.2.15), we obtain

$$\eta^{'} = 1 - \frac{3}{2}\left[\frac{(\varepsilon_2^{'}\Delta_1 + \varepsilon_1\varepsilon_3)\gamma + (\varepsilon_2^{''}\Delta_1)\delta_1}{\gamma^2 + \delta^2}\right], \tag{4.4.2}$$

and

$$\eta^{''} = \frac{3}{2}\left[\frac{(\varepsilon_2^{'}\Delta_1 + \varepsilon_1\varepsilon_3)\delta - (\varepsilon_2^{''}\Delta_1)\gamma}{\gamma^2 + \delta^2}\right], \tag{4.4.3}$$

where

$$\Delta_1 = \varepsilon_3\left(\frac{3}{\beta} - 1\right),$$

$$\gamma = (\varepsilon_2^{'})^2 - (\varepsilon_2^{''})^2 + \varepsilon_2^{'}\Delta_2 + \varepsilon_1\varepsilon_3,$$

$$\delta = 2\varepsilon_2^{'}\varepsilon_2^{''} + \varepsilon_2^{''}\Delta_2.$$

$$\Delta_2 = \Delta_1 + \varepsilon_1\left(\frac{3}{2\beta} - 1\right),$$

Below, the real and imaginary parts of the polarizability of the $ZnO@Ag$ core-shell embedded in vacuum are analyzed using Eqs. (4.4.2) and (4.4.3). The parameters used for the numerical evaluations are: $\varepsilon_1 = 8.5$, $\omega_\infty = 4.5$, $\omega_p = 1.46 \times 10^{16}\ rad/s$ [70, 71], $\Gamma_0 = 1.67 \times 10^{13}\ rad/s$, $V_f = 1.39 \times 10^6\ m/s$ and $A \approx 1$ [64, 65].

Figure 4.2, depicts the real part of the polarizability of the spherical nanoinclusions as a function of the wavelength of the incident radiation for different values of the parameter, β. It is observed that the real part of the polarizability has two sets of resonances in the UV spectral region around $\lambda = 310\ nm$ and in the visible region above $\lambda = 440\ nm$. The two sets of resonance peaks occur as a result of the surface plasmon resonances of silver at the inner and outer (ZnO/Ag and Ag/host-matrix) interfaces [70]. Due to the abundance of free carriers within the silver shell, the first set of the resonance peaks are more pronounced than the second peaks. Moreover, when the value of β is increased, which may be realized either by decreasing the size of the core or increasing the thickness of the shell, the two resonances become closer and closer to each other indicating that the real part of the polarizability is dominated by that of the metal shell.

The imaginary part of the polarizability of the nanoinclusions as a function of wavelength are shown in Fig. 4.3, for different values of β. Similar to the previous

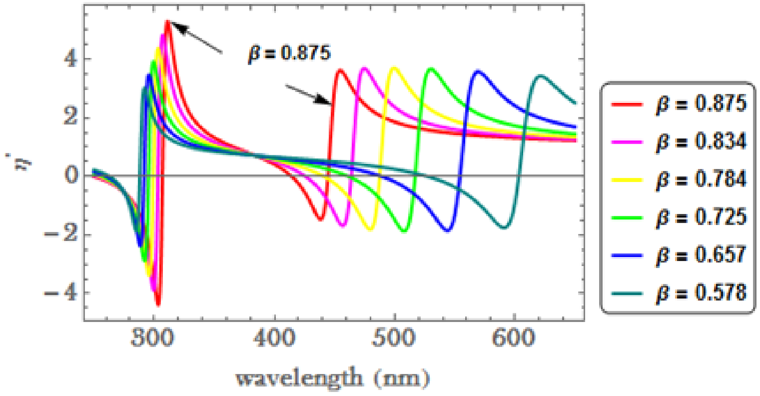

Figure 4.2: The real part of the polarizability of the spherical nanoinclusions as a function of wavelength for different values of β.

case, two sets of resonance peaks are observed in the UV and visible regions. In particular, for $\beta = 0.875$, the first peak is located in the UV region at the wavelength $\lambda = 306.8\ nm$, whereas the second resonance peak is at $\lambda = 446.3\ nm$ in the visible region.

Figs. 4.2 and 4.3, show the scattering of electrons at the interface is maximum from metal surface to the dielectric ZnO and also transmission of electrons in the metal is maximum when the metal thickness is increased. Moreover, the proposed theoretical model derived via polarization in an external electric field may be valuable in controlling and designing highly absorbing electrostatic resonance and emission from nano-sphere arrays particularly for hybrid photovoltaic applications.

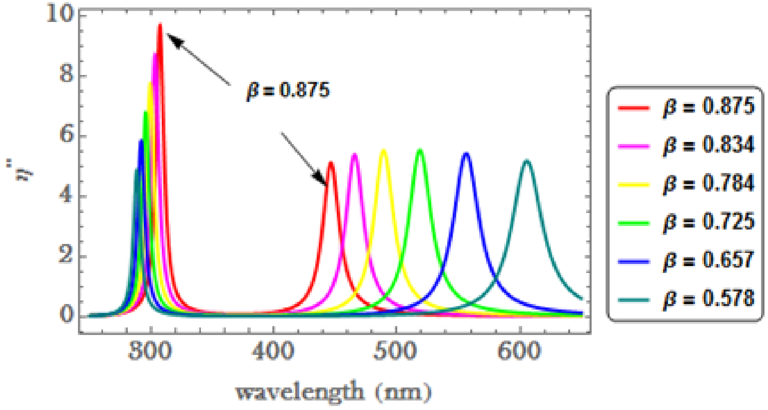

Figure 4.3: The imaginary part of the polarizability of the spherical inclusions obtained for different value of β.

4.4.2 Refractive Index

The response of a medium to an incident electromagnetic wave is described by a complex refractive index ($\tilde{n}$) which for a nonmagnetic medium is expressed as

$$\tilde{n} = \sqrt{\varepsilon_{eff}}, \tag{4.4.4}$$

where $\varepsilon_{eff} = \varepsilon^{'}_{eff} + i\varepsilon^{''}_{eff}$ is the complex effective DF of the medium. Introducing the real (n) and imaginary parts (k), $\tilde{n}$ may be written as

$$\tilde{n} = n + ik. \tag{4.4.5}$$

Further, manipulating Eq. (4.4.4) together with ε_{eff}, we find that

$$\tilde{n}^2 = n^2 - k^2 + 2ikn = \varepsilon^{'}_{eff} + i\varepsilon^{''}_{eff}. \tag{4.4.6}$$

Hence, the real and imaginary parts of the refractive index, respectively, takes the form:

$$n = \frac{1}{\sqrt{2}}\left[(\varepsilon^{'2}_{eff} + \varepsilon^{''2}_{eff})^{1/2} + \varepsilon^{'}_{eff}\right]^{1/2}, \tag{4.4.7}$$

and

$$k = \frac{1}{\sqrt{2}}\big[(\varepsilon_{eff}^{'2} + \varepsilon_{eff}^{''2})^{1/2} - \varepsilon_{eff}^{'}\big]^{1/2}. \tag{4.4.8}$$

Below, the real and imaginary parts of the refractive index of an ensemble consisting of spherical $ZnO@Ag$ core-shell nanoinclusions in vacuum are analyzed using Eqs. (4.4.7) and (4.4.8). The parameters used for the numerical evaluations are the same as that used in Section 4.4.1. Fig. 4.4 shows the real part of the refractive index as a function of the wavelength of the incident light for a fixed value of the filling factor $\xi = 0.001$ and six different values of β. The graph shows that the refractive index varies between 0.9935 and 1.008 and possesses two sets of resonances corresponding to two anomalous dispersion regions; the first set in the UV region around 300 nm and the second peaks in the visible region between 425 and 640 nm. The peaks show slight red shifts in the UV region and blue shifts in the visible region when the volume fraction, β, is increased. In addition, when β increases the two resonance peaks gets closer and closer to each other, and eventually merge for $\beta = 1$.

Furthermore, we analyzed the effect of varying the filling factor, ξ, on the real part of the refractive index, as shown in Fig. 4.5. It is observed that the refractive index in the vicinity of the two resonances progressively increases as ξ increases from 0.001 to 0.011 in steps of 0.002. However, the peaks position remain almost constant independent of the values of ξ. The result suggests that light propagates in the ensemble more readily when the concentration (ξ) of the nanoinclusions is small. Hence, as Fig. 4.5 depicts, the refractive index near the resonances can be tuned by changing the filling factor (ξ), the shell thickness, and the density of the packed nanosphere arrays, which can play a great role in applying the core-shell structure in sensors.

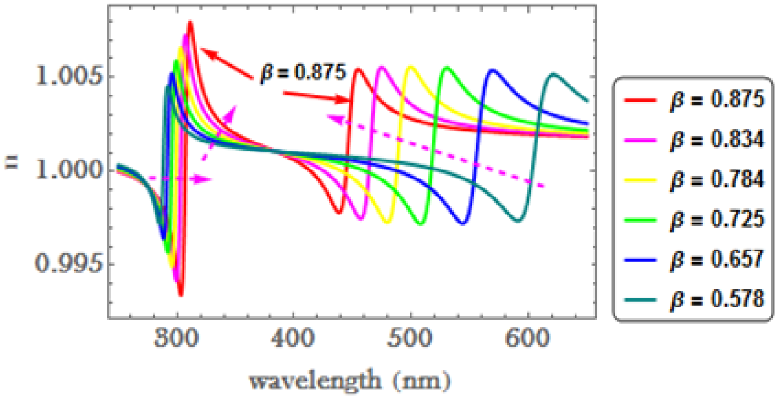

Figure 4.4: The real part of the refractive index as a function of wavelength for fixed filling factor $\xi = 0.001$ and different value of β. An increase in the metal fraction is indicated by the 'heads' of dashed arrows.

The imaginary part of the refractive index, shown in Fig. 4.6, has two resonances for the two anomalous dispersions of the system. When the volume fractions of the concentric spheres are nearly unity, the imaginary part of the refractive index in the UV region is maximum. The positions and values of the maxima strongly depend on β (with the other parameters kept constant). In particular, for $\beta \gtrsim 0.75$; the second maxima are about one-half smaller than the first one and the peaks are almost constant independent of β. In addition to the volume fraction, this phenomena can occur if the electric fields are comparable with the inner atomic fields [32]. When β is increased, the peaks in the UV region and visible regions show red shift and blue shift, respectively.

The most prominent UV emission from a bare ZnO is considered as the characteristic band edge emission of ZnO or the excitonic recombination, whereas those observed in the different regions of the UV/visible (the so-called deep level emissions)

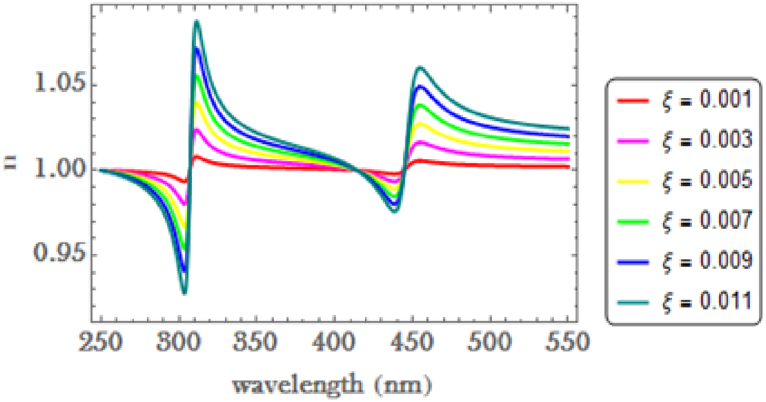

Figure 4.5: The real part of the refractive index obtained for $\beta = 0.875$ and different value of filling factor, ξ.

spectrum are attributed to intrinsic or extrinsic defects [67, 72]. Defects are boundaries and interior regions of crystals which disrupt their translational symmetry. In ZnO NPs, the intrinsic defects are those due to both oxygen and zinc vacancies, interstitials, and anti-sites [73]; and the extrinsic defects arises when a foreign atom (impurity) is inserted into the lattice. In the $ZnO@Ag$ nanostructure, the Fermi level of Ag is near the defect levels of ZnO [74, 75]; therefore, electrons can be transferred from the Ag defect levels to the Fermi level of ZnO, where these electrons are excited by incident photons. The energy level of the excited electrons is near the conduction band of Ag, which may subsequently be transferred to the conduction band of Ag where they become a part of the electron-hole recombination process thereby increasing the near band edge emission. In this model, as a consequence of the electrons transfer, the visible emission will be reduced and the UV emission will be enhanced [76]. Due to such enhancement mechanisms, the refractive index in UV region may be used for medical application in nano-fields like cancer treatment and cancer detection.

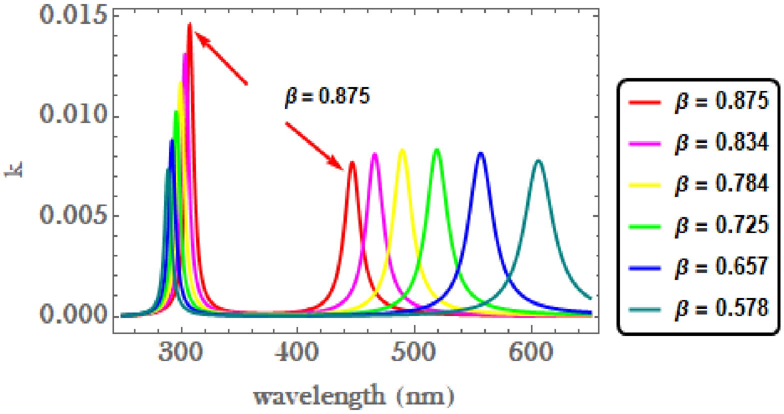

Figure 4.6: The imaginary part of the refractive index of the spherical inclusions obtained for different value of β and fixed filling factor $\xi = 0.001$.

4.4.3 Optical Absorbance

The spherical inclusions in the ensemble (system) are polarizable, with field-induced dipoles, where the dipole moments interact with the applied uniform electric field. In our case, the incident field is assumed to be polarizable along the $z-$axis which is may be expressed as $E = E_0 \exp[i\omega(\tilde{n}z - ct)/c]$, where E_0 is the amplitude of the field, $\tilde{n} = n + ik$ is the refractive index, and c is the speed of light in vacuum. Because of the presence of the term $\exp(-k\omega z/c)$, the wave decays as it propagates in the spherical core-shell nanostructure.

Incident light, in general, propagating in the medium is attenuated both by absorption and by scattering [67]. However, for NPs that are much smaller than the wavelength of light, scattering effects may be neglected so that only the absorption contributes significantly to the attenuation. The intensity (I) of the propagating wave is related to the electric field by $I \sim |E|^2$. Generally, as the wave traverses in the medium, the intensity is attenuated as [67]:

$$I = I_0 e^{-\alpha z}, \tag{4.4.9}$$

where I_0 is the intensity at $z = 0$ and α is the optical absorption coefficient defined by

$$\alpha = \frac{2k\omega}{c} = \frac{4\pi k}{\lambda}, \tag{4.4.10}$$

where $\lambda = 2\pi c/\omega$ is the wavelength of the incident radiation and k is the imaginary part of the refractive index.

The parameter which describes the typical length of light propagation in a medium is the skin depth l; defined by $l = 1/\alpha$. The quantity in the exponent of Eq. (4.4.9) is the absorbance (A) which may be generally be expressed as $A = \ln(I_0/I_t) = t\alpha$ where I_t is the intensity at $z = t$. For the $ZnO@Ag$ NPs, the absorbance at metal/shell interface takes the form:[77]

$$A(\lambda) = \frac{k\omega}{c} t_{Ag} = \frac{2\pi k}{\lambda} t_{Ag}, \tag{4.4.11}$$

where $t_{Ag} = t = a_2 - a_1$ thickness of silver shell.

Figure 4.7 depicts the absorbance of the spherical $ZnO@Ag$ nanoinclusions as a function of wavelength for $\xi = 0.001$ and different values of β, (or t_{Ag}); while the core-shell radius (20 nm) is kept constant. It shows, the two sets of absorption peaks: the first in the UV and the second in the visible spectral regions.

It is observed that when the shell thickness is increased from $t_{Ag} = 5 - 10$ nm the resonance peaks located in the vicinity of 300 nm, UV region, are enhanced and slightly red shifted. These resonances may be attributed to near band edge absorption (NBA) due to free exciton recombination. Decreasing the size of the ZnO core (or equivalently increasing the thickness of the silver shell) moved the absorption

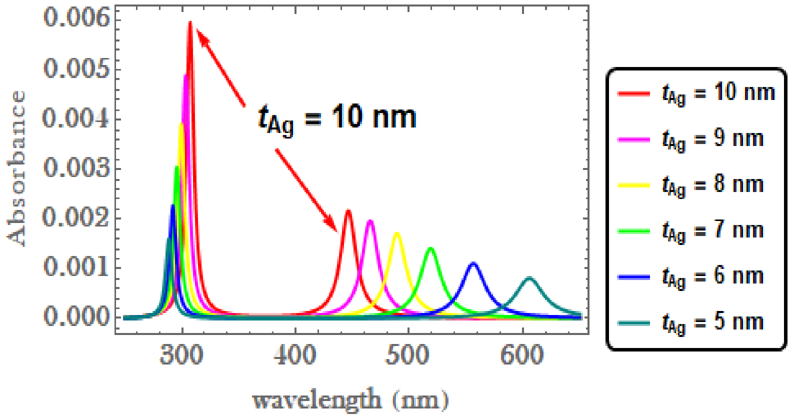

Figure 4.7: The absorbance of the spherical inclusions obtained for different value of t_{Ag} and $\xi = 0.001$. The radii (a_2) of the QDs is 20 nm.

edge in the UV spectral region towards high wavelengths (red shift). The shift of the absorption edge represented the change in the nanoparticles energy gap [78]. It means that since the bandgap of semiconductor materials will increase with the decrease in particle size, the so-called quantum size effect, it leads to the shift of the absorption edge towards high energy (blue shift) [42]. For the single semiconductor materials of ZnO NPs, absorption peak originate from the interaction between electrons in the valence band and incoming photon, which lead to excitation of these electrons to the conduction band. The optical absorbance of the composite is affected not only by the core or/and the shell, but also affected by the properties of the dielectric host matrix. The second resonance peaks located above 420 nm are in the visible spectral region. The absorption is still enhanced when the thickness of the shell is increased, but blue shifted contrary to that in the UV region. These resonance peaks are due to deep level emissions (DLE) which are attributed to the surface plasmon resonance of silver nanoshell. Such absorptions in the visible spectral region in ZnO has been frequently ascribed to several intrinsic and extrinsic effects [78]. DLE or blue radiation is due to electron recombination in oxygen vacancy with a hole in the valence band. The absorption intensity become stronger as the thickness of silver shell increase from $5-10\ nm$. On the other hand, blue shift of the absorption maximum with an increase in shell thickness and the broadening of the absorption spectra are observed when the thickness of the shell decreases [67]. This broadening of the spectra is caused because of the incorporation of the NPs size effect in our analysis via Eq. (4.3.2).

It may be concluded that the direct contact between quantum dots (QDs) of ZnO and Ag NPs can lead to interfacial charge transfer process that are of paramount importance in highly relevant topics such as photocatalytic reactions and light energy conversion [79]-[82], via the application of the core-shell nanostructure.

4.5 Conclusions

In conclusion, we studied the effect of varying the core radius and thickness of the metallic shell on the optical response of nanocomposites consisting of spherical $ZnO@Ag$ core-shell nanoinclusions embedded in vacuum. The polarizability, refractive index, and optical absorbance of the system are determined by employing the electrostatic approximation and the Maxwell-Garnett effective medium theory. Moreover, the DF of the silver shell is chosen to be of the modified Drude form that takes into account its nano-size. It is shown that for different values of the metal fraction β and filling factors ξ, the graphs of the real and imaginary parts of the polarizability and refractive index of the nanocomposites as a function of wavelength possess two resonance peaks in the UV (around 300 nm) and visible (between 425 and 640 nm) spectral regions. These resonance peaks correspond to the surface plasmon resonances of Ag at the ZnO/Ag and $Ag/$host-matrix interfaces, respectively. The resonance peaks show slight red shift in the UV region and blue shift in the visible region when β or ξ is increased. Similarly, for a fixed core-shell radius of 20 nm, the graphs of the optical absorbance versus wavelength for fixed $\xi = 0.001$ and different values of shell thicknesses ($t_{Ag} = 5 - 10$ nm) show also two sets of absorption peaks - in the same spectral regions. It is observed that when the Ag shell thickness increases, the two sets of resonance peaks are enhanced; accompanied with slight red shift in the UV and blue shift in the visible spectral regions.

The enhancement in the optical properties is mainly attributed to strong coupling of the surface plasmon resonance of the Ag shell and the energy gap of the ZnO NPs in both spectral regions. Indeed, compared with the bare ZnO, the silver coated ZnO NPs possess improved potential device applications in the optical frequency region. The results may be used to optimize ‘desired’ device parameters of nanocomposites consisting of $ZnO@Ag$ core-shell nanostructures that are designed for various applications such as sensors and nano-optoelectronics devices.

Chapter 5

Plasmonic Properties of Spheroidal Spindle and Disc Shaped Core-Shell Nanostructures Embedded in Passive Host-Matrices

5.1 Introduction

Core-shell nanosystems essentially involve two or more particles/compounds formed by using encapsulation process in different shape and size to obtain a new composite material with combined properties and other unique properties neither shown by the core or by the shell nanostructures (NSs) [83]. Incorporating nanoparticles (NPs) in complex, multilayer, or core-shell nanostructures have attracted significant interest because they can offer additional opportunities for innovation with tailored materials in the fields of physics, nanomaterials, biomedical nanosystems, optical, chemical and biological sensors [84], magnetic nanocomposite [85], engineering chemistry [86], photocatalysis [87], solar cells [88], and electrical nanosystems. This unique property originates from the confined spatial distribution of polarization of charges over the surface of the nanostructure. The spatial and dynamic behavior of charge polarization over a variety of geometrical shapes and dielectric properties is the fundamental secrets and pillars of their applications suites. Among these special structures, the core-shell is a particular class of NPs, consisting of a core and one or several shell layers.

Recently, noble metal nanoparticles (NPs) have attracted the attention of the scientific community due to their unique catalytic [89], electronic [90], plasmonic and optical [91] properties. Additionally their chemical inertness, bio-affinity, strong absorption of light [92], which are dominated by the localized surface plasmon resonance (SPR) continues to inspire interest in the research and industrial community. Beside this, the key concept in the field of plasmonics is the surface plasmon resonance − a collective resonant oscillation of the conduction electrons in the metal confined to the interface between the metal and a dielectrics (or semiconductor), which are described by evanescent electromagnetic waves that are not necessarily located at the interface [93]. SPR spectra of the composite nanoparticles have been shown to vary with the particle size, shape, composition and the surrounding medium [94]-[96].

Different types of core-shell nanoparticles (CSNPs) based on various core and shell materials have been investigated, including CSNPs with metal@metal, metal@dielectrics, and dielectrics@metal, as well as dielectrics@dielectrics structures [97]. In particular, ZnO@noble-metal CSNPs possess a wide variety of potential applications in many developing technologies [98, 99]. It is found that surface coating with noble metals like Ag, Au, Cu, Pt, can dramatically change the properties of ZnO nanocrystallites as well as its applications. Silver nanoparticle with thicknesses ranging between 5 and 10 nm is widely preferred as a shell material on ZnO nanospindle and nanodisc shape due to its non-toxicity [100], strong absorption in/near visible spectrum [56], high electrical and thermal conductivity, high work function, antibacterial characteristics, and cost effective [100].

For spheroidal shaped CSNSs embedded in a host matrix, three plasmon resonance frequencies are expected; corresponding to the oscillation of electrons along the three axes. The resonance wavelength depends on the orientation of applied filed relative to the particle. In addition to this, by changing the axes length, the plasmon resonance wavelength of the nanospheroid can be turned systematically. The possibility of tuning the plasmon resonance of NPs has attracted attention of scientists and large variety of new synthesis methods have been developed to fabricate elongated [101] as well as flattened CSNSs. In view of the interesting material properties of CSNPs described above, we seek to further investigate theoretically and numerically the optical and plasmonic properties of prolate (spindle) and oblate (disc) shaped $ZnO@Ag$ core-shell NPs embedded in a dielectric host matrix by varying the core size, shell thickness, size of composite and host medium.

5.2 Model of Spheroidal Core-Shell Nanostructure

Due to the spheroidal shape, the surface plasmon mode would split into two distinct modes. The first is along the short axis of the spheroid, while the second is rather along the long axis as shown in Fig. 5.1. The two oscillations induce a charge separation and thus localized at the interface, they lead to two plasmonic modes namely the transverse and longitudinal modes depending on the direction of propagation of the applied field.

The optical as well as plasmonic properties of two layers nanoparticles consisting of a core and shell can be successfully described within the framework of classical electrodynamics of continuous media. Consider an array of spheroidal core-shell composite nanoparticles consisting of a semiconductor core and a metallic shell embedded in a non-absorbing (passive) host matrix; of the dielectric functions (DFs) ε_c, ε_s, and ε_h, respectively, as shown in Fig. 5.1(A). Figure 5.1(B) depicts the cross-sectional views of prolate and oblate shaped core-shell nanocomposites. The core ellipsoidal NPs are characterized by shell thickness t and semi-principal axes a_1, a_2, and a_3 with (i) $a_1 > a_2 = a_3$ for prolate and (ii) $a_1 < a_2 = a_3$ for oblate. Note that the prolate (spindle-shaped) spheroid can be generated by the rotating an ellipse about its major axis (a_1 in Fig. 5.1B(i)), while the oblate (disc-shaped) spheroid may be generated by rotating an ellipse about its minor axis (a_1 in Fig. 5.1B(ii)). The polarizability of the composite depends on the dielectric function of its constituents i.e., ε_c, ε_s, and ε_h.

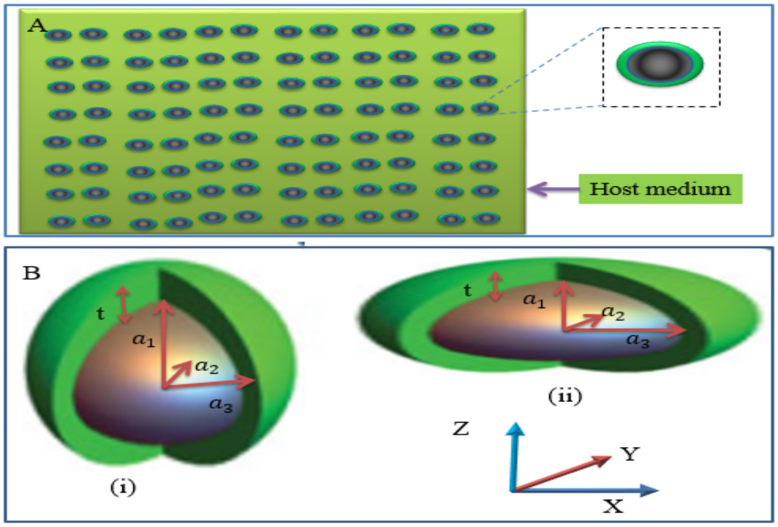

Figure 5.1: The arrays (A) and the structure (B) of core-shell nanostructure, with prolate (B(i)) oblate (B(ii)) shaped CSNS embedded in host matrix .

When the system is irradiated with electromagnetic waves, assumed to be polarized perpendicular to the xy plane (along a_1 in Fig. 5.1(B)), the applied field causes the polarization of the system. The effective polarizabilities α_i of the core-shell system can be shown to have the form [102, 103],

$$\alpha_i = V\left[\frac{(\varepsilon_s-\varepsilon_h)(\varepsilon_s+(\varepsilon_c-\varepsilon_s)(L_i^c-fL_i^s))+f\varepsilon_s(\varepsilon_c-\varepsilon_s)}{(\varepsilon_s+(\varepsilon_c-\varepsilon_s)(L_i^c-fL_i^s))(\varepsilon_h+(\varepsilon_s-\varepsilon_h)L_i^s)+fL_i^s\varepsilon_s(\varepsilon_c-\varepsilon_s)}\right], \tag{5.2.1}$$

where V is the volume of the core-shell nanocomposite; f is the fraction of the total volume occupied by the core (or core concentration). These terms are expressed as follows:

$$V = \frac{4\pi}{3}(a_1+t)(a_2+t)(a_3+t). \tag{5.2.2}$$

$$f = \frac{(a_1)(a_2)(a_3)}{(a_1+t)(a_2+t)(a_3+t)}. \tag{5.2.3}$$

L_i^s and L_i^c are the depolarization factors of the composites (core + shell) and core, respectively, $i = 1, 2, 3$ refer to the longitudinal ($i = 1$) and degenerate transverse ($i = 2, 3$) modes. It is worth noting that in the frequency domain of interest, we assumed that the DF of the ZnO core to be a real constant ($\varepsilon_c = constant$) independent of frequency, whereas the DF, $\varepsilon_s = \varepsilon_{s1} + i\varepsilon_{s2}$, of the silver shell is chosen to be of the Drude form. By rewriting Eq. (2.2.6) as

$$\varepsilon_s(\omega) = \varepsilon_\infty - \frac{\omega_p^2}{\omega(\omega+i\gamma)}, \tag{5.2.4}$$

where ε_∞ is the permittivity at high frequency, ω_p is the plasma frequency, γ is the electron collision frequency (damping constant describing dissipative losses), and ω is the frequency of the incident radiation.

For convenience, we introduce the following notations $a_c = a_2 = a_3$, $a_s = a_2 + t = a_3 + t$, $c_c = a_1$ and $c_s = a_1 + t$; for both prolate and oblate spheroids (refer to Fig.

5.1(B)).

For prolate spheroid, the depolarization factors along a_1, a_2, and a_3 axes, respectively, are given by [102]

$$L_1^{s,c} = \frac{1-e_{s,c}^2}{e_{s,c}^2}\left(\frac{1}{2e_{s,c}}\ln\left[\frac{1+e_{s,c}}{1-e_{s,c}}\right]-1\right), \tag{5.2.5}$$

$$L_2^{s,c} = L_3^{s,c} = 0.5(1-L_1^{s,c}), \tag{5.2.6}$$

where the subscripts 'c' is for the core and 's' is for the composite (core + shell), and $e_{s,c}$ are the ellipticity of the core and the composite, respectively, which are defined by

$$e_{s,c}^2 = 1 - \frac{a_{s,c}^2}{c_{s,c}^2} \tag{5.2.7}$$

Similarly, the corresponding depolarization factors for oblate spheroid are given by [104]

$$L_1^{s,c} = \frac{g}{2e_{s,c}^2}\left(\frac{\pi}{2}-\arctan(g)\right)-\frac{g^2}{2}, \tag{5.2.8}$$

$$L_2^{s,c} = L_3^{s,c} = 0.5(1-L_1^{s,c}), \tag{5.2.9}$$

where

$$e_{s,c}^2 = 1 - \frac{c_{s,c}^2}{a_{s,c}^2} \qquad g^2 = \frac{1-e_{s,c}^2}{e_{s,c}^2}. \tag{5.2.10}$$

The aspect ratios (AR) of the prolate and oblate nanoparticles are defined by $AR_c = c_c/a_c = a_1/a_2$ and $AR_c = a_c/c_c = a_2/a_1$ for the cores and $AR_s = c_s/a_s = (a_1+t)/(a_2+t)$ and $AR_s = a_s/c_s = (a_2+t)/(a_1+t)$ for the composites, respectively.

In the quasi-static limit, the extinction cross-section σ_{ecs} of the ensemble (system) can be modeled and has the relation with absorption cross-section σ_{acs} and scattering cross-section σ_{scs}, which are expressed in Eq. (2.4.1). The term σ_{acs} and σ_{scs} for spheroidal structures are defined by [105]

$$\sigma_{acs}(\lambda) = \frac{k}{3}\sum_{i=1}^{3} Im[\alpha_i(\lambda)], \tag{5.2.11}$$

and

$$\sigma_{scs}(\lambda) = \frac{k^4}{18\pi}\sum_{i=1}^{3} |\alpha_i(\lambda)|^2, \tag{5.2.12}$$

where k is a parameter which depends on the wavelength (λ) of the incident light. That is

$$k = \frac{2\pi}{\lambda}\sqrt{\varepsilon_h}. \tag{5.2.13}$$

Furthermore, among the important parameters that are used to characterize the plasmonic properties of NSs is the radiation efficiency, η_{rad}. It is defined by [26, 106],

$$\eta_{rad} = \frac{\sigma_{scs}}{\sigma_{ecs}} = \left(1 + \frac{\sigma_{acs}}{\sigma_{scs}}\right)^{-1}. \tag{5.2.14}$$

It is worth nothing that, the radiation efficiency represents how much of the incident light interacting with the nanoparticles is scattered rather than being absorbed.

5.3 Numerical Analysis

Unlike spherical shaped nanostructures, NPs with different symmetry axes exhibit more than two plasmonic modes [107]. Since a spheroid has three-fold symmetry axes, it exhibits both longitudinal and transverse plasmon modes corresponding to the redistribution of the polarized charges along each principal axes. For an electromagnetic field applied on a core-shell nanocomposite, changing size and shape of the composite results in changing negative/positive charges separation and hence tailoring the frequency and the intensity of the SPR in different wavelength of incident radiation. The oscillatory shift of the electron cloud relative to the positive core along each principal axes results in two plasmonic modes: longitudinal mode (LM), and transverse mode (TM).

Below, we apply numerical investigation on the effect of size, shape, thickness of the metallic shell, and the host matrix on the optical and plasmonic properties of spindle and disc shaped $ZnO@Ag$ core-shell. For numerical analysis, we used the following values: $\varepsilon_c = 8.5$, $\varepsilon_h = 2.25$, $\varepsilon_\infty = 4.5$, $\omega_p = 1.46 \times 10^{16}\ rad/s$, and $\gamma = 1.67 \times 10^{13}\ rad/s$ [92].

5.4 Results and Discusion

5.4.1 Absorption Cross-Section

The absorption cross-sections of spindle and disc-shaped spheroidal core-shell NSs as a function of wavelength are depicted in Figs. 5.2; for three different shell thicknesses of 5 nm, 10 nm, 15 nm, and constant core-shell aspect ratio of $AR_s = 2.0$. Fig. 5.2(A) shows the simulated σ_{acs} spectra of the spindle-shaped CSNSs for the parameters AR_c are 2.33, 3.00, and 5.00, corresponding to the core concentrations (f) of 49.22 %, 18.75 %, and 3.91 %, respectively. It is observed that there are four resonance peaks. The first two resonance peaks (located between 300 and 500 nm) correspond to surface plasmon resonances of the silver shell at the inner and outer interfaces [92]. The peaks of these two resonances are found to decrease and red-shifted with an the increase of core concentration; in agreement with that reported in Ref. [108]. On the other hand, the third and fourth set of resonance peaks (located above 500 nm) are due to the polarization of charges along the principal axes of the spheriod. In particular, the third resonance peaks (counted from left) are associated with the transverse plasmon mode (TM), while the fourth peaks correspond to the longitudinal mode (LM). The peaks of the TM modes decrease and are blue shifted when the core's aspect ratio and shell thickness increase. This is attributed to the increase in the frequency dependent restoring force with decreasing shell thickness. The polarized charge spacing is reduced when the shell size decreases. Moreover, the longitudinal surface plasmon resonance (fourth resonance peaks) are found to be very sensitive to the aspect ratio, AR_c, [102] - it is seen that as AR_c is increased, the longitudinal band maximum is shifted to shorter wavelengths with a relative increase in the peak intensity.

The plasmonic properties NSs vary based on the shape of the core-shell NPs. In Fig. 5.2(B), the graph of σ_{acs} versus wavelength for the disc-shaped CSNSs are shown for the same parameters as that used in Fig. 5.2(A) with the corresponding core

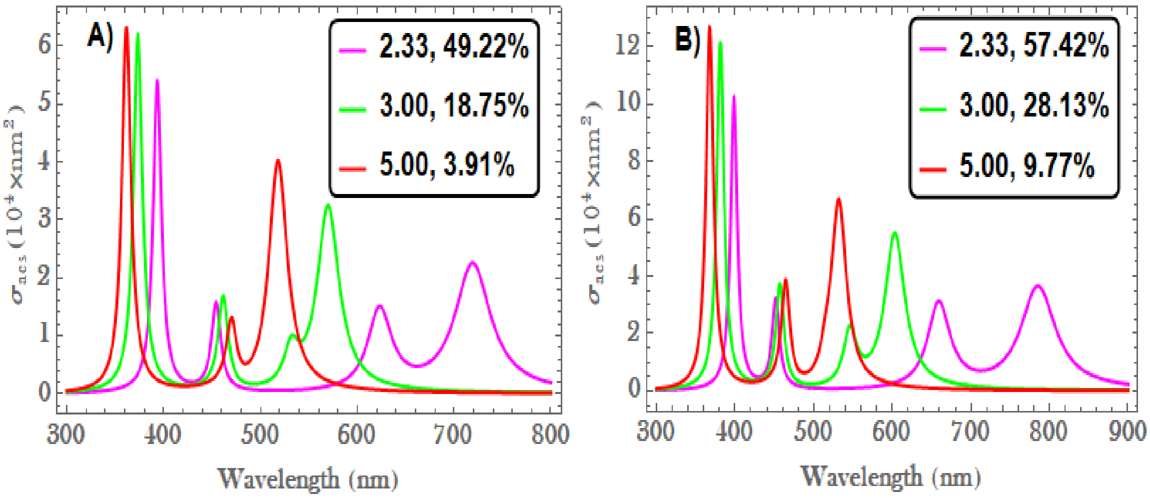

Figure 5.2: The absorption cross-sections for (A) spindle- and (B) disc-shaped CSNSs; for $AR_c = 2.33,\ 3.00,\ 5.00$ and constant $AR_s = 2.0$, $\varepsilon_h = 2.25$ [109].

concentration being $f = 57.42$ %, 28.13 %, 9.77 %. Similar to the previous case, there are four resonance peaks - the first two (counted from left) corresponding to the plasmon resonances of the silver shell while the third and fourth peaks corresponding to the TM and LM, respectively. It is seen that all the peaks decrease and are blue shifted with an increase in the core's aspect ratio and shell thickness. Moreover, comparison of Figs. 5.2(A) and (B) shows that (i) the corresponding resonance peaks are more pronounced for the disc-shaped CSNSs than that for the spindle-shaped and (ii) the TM and LM resonance peaks of the disc-shaped spheroid are more broader and red shifted with respect to that of the spindle-shaped. For small NPs, the SPRs are influenced by the NP size for the same constitutes of composite, such that, for particles of few nanometers the resonances do not change their position or wavelength, but they become wider because of dispersion effect. When its size increases (here the volume of nanodisc is almost twice of nanospindle) the SPR are now affected by the secondary radiation which moves their position to larger wavelength (red shifted) and makes the peaks broader [93]. The results may indicate that with appropriate design of core-shell nanoparticles, it is possible to achieve broad band response for light harvesting in photovoltaic application [110, 111] or extremely narrow band width response for applications such as bio-sensing, lasing and photo-switching [112].

Also, note from Figs. 5.2(A) and (B) that for $AR_c = 5.0$ the third and fourth resonance peaks associated with the LM and TM modes effectively merge (there are only 3 peaks for $AR_c = 5.0$, unlike the other two). This may be attributed to the fact that as synergetic effect between the components as well as their structural details can be designed in such a way that they positively interact with each other.

For particles of sizes larger than 100 nm, the spectrum of scattering cross-section is larger than the absorption cross-section even at low wavelength of incident light [113]. However, NPs which have sizes less than 100 nm (which is less than the wavelength of light) have small scattering cross-sections at high wavelengths and larger at low wavelengths than absorption cross-sections [113]. Figure 5.3 shows σ_{acs}, σ_{scs} and σ_{ecs} spectra, which is plotted for the shell thickness of 5 nm and core concentration $f = 46.88$ %. It is seen that the scattering cross-section is above the absorption cross-section at lower wavelength. In all cases, there are four peaks including longitudinal and transverse resonance peaks due to the two interfaces of silver nanoparticles and bonding/antibonding of the composite at the surfaces for large concentration of core ZnO NPs around 50 %.

We also analyzed the plasmonic response of both spindle- and disc-shape spheroidal $ZnO@Ag$ core-shell nanostructures for the TM and LM plasmonic modes. Fig. 5.4 depicts these plasmonic modes plotted both for the spindle- and disc-shaped spheroidal core-shell NPs; for equal lengths of the major and minor axes, i.e., the aspect ratio

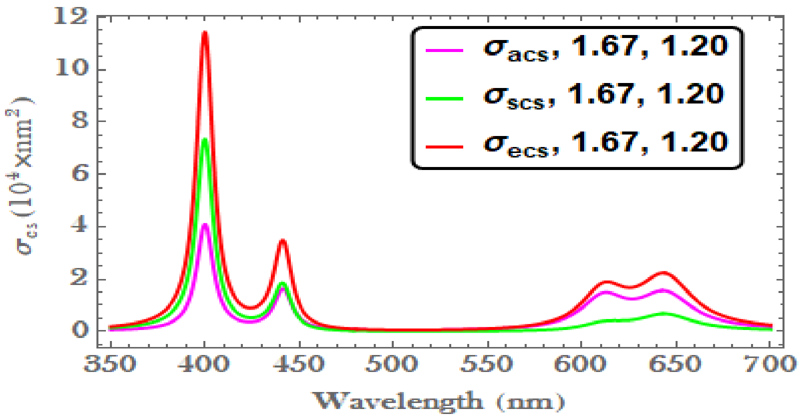

Figure 5.3: σ_{acs}, σ_{scs} and σ_{ecs} of the same size of spindle shaped; for $AR_c = 1.67$, $AR_s = 1.20$, $t = 5$ nm, and $\varepsilon_h = 2.25$.

of core ZnO of both NSs is arranged at 2.33. Consistent with that obtained in Fig. 5.2, the spectra shown in Fig. 5.4 confirms that the resonance wavelength of the disc-shaped (oblate) core-shell nanoparticles have the largest absorbance spectra and are red shifted compared with the spindle-shaped (prolate) CSNSs.

The effect of shape on the plasmonic properties of spheroidal $ZnO@Ag$ core-shell nanostructures is depicted in Fig 5.5. As shown in the Fig. 5.5(A) and (B), TM and LM resonance peaks for the disc-shaped NPs are enhanced compared with those for the spindle-shaped NPs. In addition, the spectrum of the TM and LM peaks for the disc-shaped NPs extends well beyond the visible spectrum, i.e., one of the peak for $AR_c = 1.88$ and $AR_s = 1.67$ lies in the near infrared region. However, when the aspect ratios of both core and composite are increased, the longitudinal resonance modes are red-shifted for the disc-shaped spheroids and blue-shifted for the spindle shaped structures. The transverse resonance modes of the spindle-shaped core-shell NSs coincide, while that for the disc-shaped structure the resonance peaks

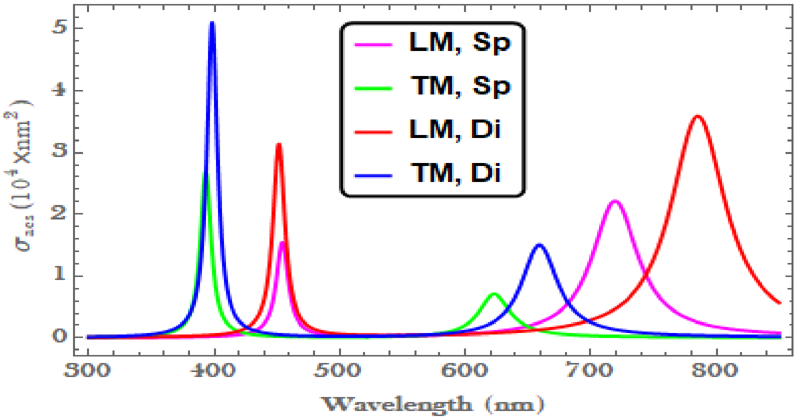

Figure 5.4: LM and TM resonance modes of spindle- and disc-shaped spheroids as a function of wavelength. The parameters used are $AR_s = 2.0$, $AR_c = 2.33$, and $t = 5\ nm$.

are enhanced and red-shifted. These properties arises for the same freedom of charge oscillation and AR, due to the shape of the composites as well as the core's concentration, which are strongly related to the size and quantum confinement effects. Here, the core concentration vary from 49.22 % to 49.70 % for the spindle-shaped and from 57.21 % to 55.94 % for the disc shaped nanostructures when the aspect ratios of composite is decreased form $AR_s = 2.00$ to $AR_s = 1.67$.

The other factor that affects the plasmonic properties of core-shell NSs is the dielectric function (or refractive index (RI)) of the host matrix. Fig. 5.6 depicts the effect of varying the DF of the host medium on the spindle-shaped $ZnO@Ag$ spheroidal core-shell NSs. It is observed that the RI considerably affects the plasmonic properties, i.e., the spectra of the absorption cross-section of the spindle-shaped CSNSs is red-shifted in both near-UV/visible and infrared spectral regions, when the refractive

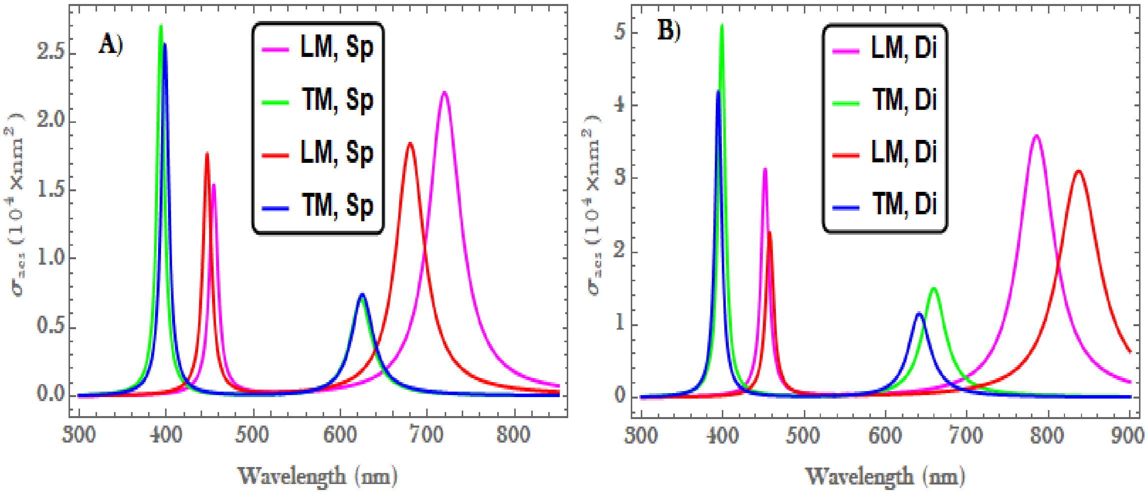

Figure 5.5: The effect of shape on LM and TM resonance modes of the absorption cross-section spectra for (A) spindle-shaped and (B) disc-shaped spheroids, for $AR_s = 2.0,\ 1.67$. The parameters used are $AR_c = 2.33,\ 1.88$, and $t = 5\ nm$.

index of the host medium is increased. For refractive index larger than 2, the location of the LM resonance modes shift toward the infrared region with the spectra becoming broader and broader. The absorption cross-section spectra of the CSNSs attains maximum peaks for small refractive index, except for the medium of vacuum in UV region, and decrease with increasing refractive index of the medium. On the other hand, the peaks of the TM resonance modes increase while that of the LM slightly decrease with increasing refractive index. Similar effects are observed for disc-shaped spheroidal CSNSs.

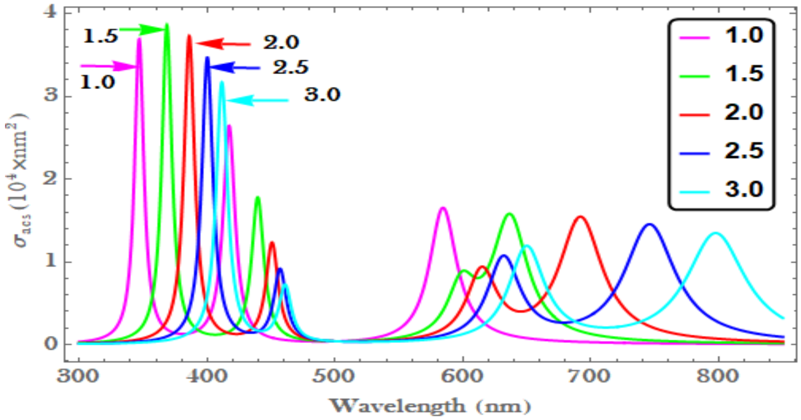

Figure 5.6: The absorption cross-section of a spindle-shaped spheroid as a function of wavelength, for a host matrix of five different refractive index $RI = \sqrt{\varepsilon_h}$. The other parameters are $AR_s = 2.0$,$AR_c = 2.33$, and $t = 5\ nm$.

5.4.2 Radiation Efficiency

Finally, we plotted the radiation efficiency (η_{rad}) of both geometries as shown in Fig. 5.7(A) for the disc-shaped and Fig. 5.7(B) for the spindle-shaped NSs by using the same parameters as that used in Fig. 5.2. As shown in the Figures, due the effect of shape, η_{rad} is more enhanced and red-shifted for disc-shaped CSNS than spindle-shaped. The radiation efficiency indicate the re-radiation of the incident energy and its dependence of the strength of the resonance at a given wavelength. As depicted in Fig. 5.7, due to the interband transition of the metal silver coat, the radiation efficiency is low at low wavelength for small concentration of the silver shell. When the thickness of the silver on ZnO nanoparticles increase, the radiation efficiency becomes intense and broaden. For large concentration or thick coat of silver, the CSNSs has higher polarizability [106], resulting in larger radiative rate as shown in both Figures, Figs. 5.7(A) and (B) for higher wavelengths.

In the long wavelength regions, the spectra with the minimum peak value of the

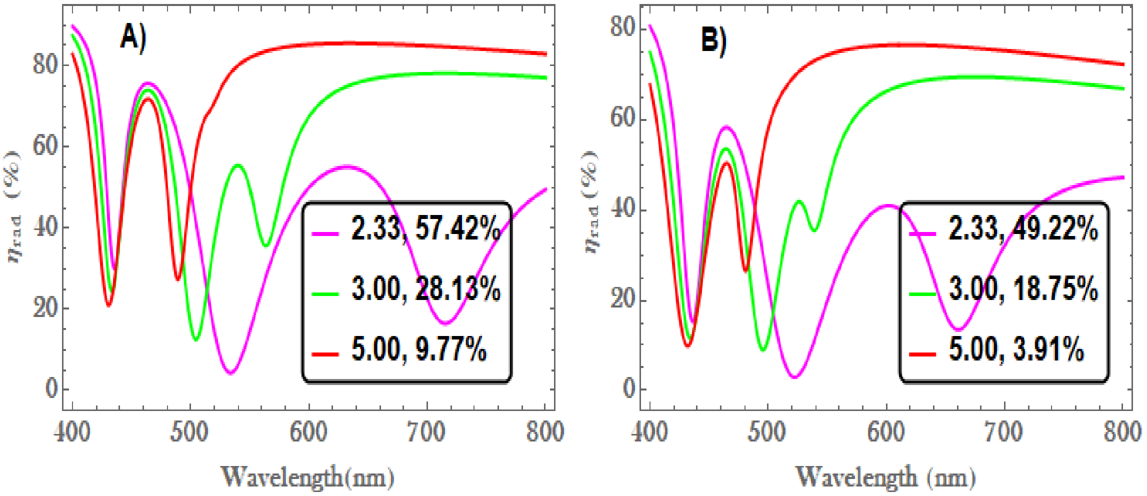

Figure 5.7: Radiation efficiency of (A) the disc-shaped, (B) the spindle-shaped CSNSs as a function of wavelength; for three different values of AR_c. The other parameters are similar to that used in Fig. 5.2.

radiative efficiency exhibits more red-shifted, while there is a little red-shift for the "Fano-like" resonances [70, 114] observed around 430 nm, which tell us that at the particular wavelength, η_{rad} is dominated by absorption rather than scattering. In the quasi-static limit approximation method, the ratio of scattering to absorption rate increases for large particles, which is valid for subwavelength scale particles, while particles with sizes comparable to or larger than the incident wavelengths are likely to suffer from electrodynamic damping, causing energy loss through particle heating. In particular, for applications in thin photovoltaic layers, plasmonic particles with high optical radiation efficiencies can be positively rigid their supportive ability as well as enhance the effective absorption length at longer wavelengths [26].

5.5 Conclusions

In this work, we studied the effect of size, shape, shell thickness, and the nature of the surrounding environment on the plasmonic and optical properties of spindle- and disc-shaped spheroidal $ZnO@Ag$ core-shell nanostructures. It is found that the absorption and scattering efficiencies of semiconductor ZnO nanoparticles strongly depend on the thickness of the silver shell with the optical properties being strongly modified as a result of the metal coating. In particular, the numerical analysis for different values of shell thickness, size, shape, and refractive index of the host medium, the spectra of the absorption cross-section of $ZnO@Ag$ nanoinclusions as a function of wavelength possess four plasmon resonance peaks with the peaks extending from the UV to near-IR spectral regions. These resonance peaks correspond to the silver/core, silver/host-matrix interfaces, and the bonding/antibonding pairs due to separation of charges in the composites along the principal axes. Moreover, the position of the resonance peaks strongly depends on the aspect ratio and refractive index of the medium exhibiting a shift towards higher wavelengths with an increase in the refractive index of the host medium and thickness of the silver shell. The results obtained in this work may be utilized in various applications which employ shape-dependent plasmonic effects of core-shell spheroidal nanostructures.

Chapter 6

Synthesis and Characterization of Ultraviolet Emitter ZnO Nanoparticles for Photocatalytic Application

6.1 Introduction

Zinc oxide is a n-type semiconductor [115, 116] with deep ultraviolet (UV)/ visible absorption [116], high thermal and mechanical stability at room temperature [117] and a highly effective UV absorber [118]. Zinc oxide (ZnO) nanoparticles (NPs) are semiconductors which have wide applications in piezoelectric devices, photo-catalysis, solar cells, pigments, electrical devices, biological, anti-UV additives, UV-light of emitters, and cosmetic [119]-[121].

Today, to synthesize ZnO NPs, many chemical and physical routes have been developed. Among many different synthesis routes; precipitation [122, 123], hydrothermal synthesis [124, 125], sol-gel [126], electrochemical deposition [127], mechanochemical [128] are few of them to obtain products with particles differing in shape, size and spatial structure. Among and in addition to these routes, rapid thermal decomposition, sol-gel and biological methods are mostly preferable related to the difficulty of scale up the process of synthesis, separation and purification of nanoparticles from the surfactant, co-surfactant, organic solvents and toxic materials. In addition to this, the advantages of these methods compared with other methods are cost-effective, simplicity, non-toxicity and easy to control size, shape and morphology of the particles at a given temperature.

Biological or green synthesis methods for ZnO NPs using the extraction solution of microorganisms, enzymes, and different parts of plants [129] have recently been proposed as potential for eco-friendly alternatives to chemical and physical methods. In various fields, the green synthesis of ZnO NPs is applicable, particularly for biological, cosmetic, medicinal, and antibacterial activities. For instance, as reported in [130], ZnO NPs synthesized using plant leaf are used for antifungal activity, in [131] synthesized from vegetable for DSSC application, in [132] synthesized from plant leaf for anti-bacterial activity and in [133] synthesized from tea leaf for solar cell applications. The application of ZnO NPs depend on their inherent properties which are correlated to particle size, morphology and defect structure. By increasing the number of active sites of the synthesized samples [134], this surface defect has a significant effect on optical and electronic properties, as well as on photocatalytic activity. If surface defects can be systemically introduced into the material by air-quenching (thermal decomposition) of the precursors, these properties can be monitored. Intrinsic defects can be introduced by annealing temperature whereas extrinsic defects occur due to addition of doping metal ion. The size and morphology of nanoparticles has also influenced on the type of defect centers.

Lot of researchers used to study *ZnO* NPs as photocatalyst for the degradation of the organic dye and found that it shows good photocatalytic activity. Photocatalysis occurs on the surface [117] of the semiconductor (catalyst) and its efficiency is strongly influenced by morphology and surface modification of the oxide. The band gap of semiconductor materials has pairs of electron-hole, producing electrons in the conduction band, and producing holes in the valance band. In order to produce reactive oxygen species responsible for photocatalysis, some of these charge carriers scatter across the crystal surface and react with the absorbed water molecules which are hydroxide ions and oxygen molecules.

Due to noble properties and various applications of *ZnO* NPs, we focused on the photocatalytic application of this nanomaterial by comparing the new synthesis method with familiar method. Recently, biological route (green synthesis method) has impressed many researchers due to its cost-effectiveness, non-toxic and harmless reactions which made it superior than conventional methods. To the best of our knowledge, for photocatalytic use, ZnO NP synthesized by biological route from olea leaves, sansevieria (mother in-law tongue), abies fraseri conifer and also rapid route is not yet reported. We fabricated ZnO NPs via rapid, biological and sol-gel routes. Rapid and biological routes are new for photocatalytic application and have many advantages than the other routes. We used olea leaves (broadly grown in Ethiopia) and Sansevieria (mother-in-law tongue) and abies fraseri conifer (widely available in PR. China) for biological synthesis of *ZnO* NP as capping and stabilizing agent.

6.2 Materials and Methods

6.2.1 Materials

Materials and solvents that are used for the synthesis of ZnO nanoparticles via three methods are zinc acetate dihydrate ($Zn(CH_3COO)_2.2H_2O$, 99 %), sodium hydroxide ($NaOH$, 96 %), fresh and healthy olea leaves, sansevieria (mother-in-law tongue), and abies fraseri conifer, ethanol absolute and dionized (DI) water.

6.2.2 Methods

Synthesis Methods of ZnO

In this experiment, we prepared five samples labelled as RP, SG, OL, $MILT$, and AFC by using three methods; rapid, sol-gel and green synthesis methods from the same precursor and in same annealing temperature within different annealing times. ZnO nanoparticles (called RP sample) were synthesized using $Zn(CH_3COO)_2.2H_2O$ as a precursor material via rapid synthesis method. The synthesis of nano-rod morphology of zinc oxide nanoparticles were conducted according to the procedures developed in [135]. About 12 gm of $Zn(CH_3COO)_2.2H_2O$ was placed into a silica crucible and calcinated at 400 ^0C for 12 h in a muffle furnace without any special atmospheric condition. Above this temperature, the particles are found to thermally degrade [136] and we observed a color change from white to a dark ash color. Finally, the obtained material was grinded using mortar and pestle.

The second sample (SG) were synthesized from the same precursor only by changing the synthesis method according to the procedures developed [137]. ZnO nanoparticles have been prepared using the mentioned precursor by sol-gel method. An aqueous solution of 0.3 M (or 4.7756 gm) zinc acetate dihydrate ($Zn(CH_3COO)_2.2H_2O$) is dissolved in 50 mL DI-water and stirred for about 25 minutes at room temperature. After this reaction time, 50 mL of 0.75 M (or $2gm$) sodium hydroxide ($NaOH$) solution was added dropwise. The mixture is stirred for 4 h at room temperature. After 4 h, the deposited gel-like solution is washed with DI-water and ethanol several times. The samples are then suspended in ethanol and allowed to age for 2 h without stirring. Thereafter, the sample filtered by electronic filter is dried in an oven at 80 ^oC for 2 h. Then, the prepared ZnO nanoparticles are placed in the middle of muffle furnace in silica crucible after grinded. The samples have been annealed at 400 ^oC for 4 h.

And in the other case, the other three samples of ZnO NPs are synthesized by using green synthesis method from plants used as surfactant; (i)- from olea leaves (OL), (ii)- from sansevieria (mother-in-law tongue) ($MILT$), and (iii)- from abies fraseri conifer (AFC). A certain gram of olea leaves were collected from olive trees planted at Faculty of Natural and Computational Sciences of Addis Ababa University (Ethiopia) and also sansevieria (mother-in-law tongue) and abies fraseri conifer are collected from North campus of Yancheng Institute of Technology (P.R. China). The collected leaves were washed several times with DI-water to remove dust particles and then dried by sunshine to remove the residual moisture. Extracted samples were prepared by placing 15 gm of dried fine cut in 500 mL glass beaker along with 400 mL of DI-water for each types of plants separately. The mixture was then boiled until the color of aqueous solution changed from watery to yellow. The mixture was cooled to room temperature and filtered with Whatman No. 1 filter paper before centrifuging at 1200 rpm for 1 h to remove biomaterials. In a typical reaction mixture, 15 mL of the aqueous yellow extract of plants were added to 300 mL of 4 mM of aqueous zinc acetate dihydrate solution and stirred at room temperature for 10 *min* to achieve pale yellow solution. After that, 1 *M* sodium hydroxide solution is added to the mixture drop by drop, with continuous stirring at room temperature, that leads to change the color from yellow to yellowish-white suspension. The suspended particles were purified by dispersing in DI-water and centrifugation several times. Afterwards, the white particles were washed with DI-water to remove the impurities for the final product. Then a white powder was obtained after drying at a temperature of 400 ^oC for 8 *h* in furnace. The dried samples were grinded using mortar and pestle for characterization.

Photocatalytic Degradation of Methyl Orange Dye

The photocatalytic performances of the samples were evaluated by the decomposition of methyl orange (MO) solution under UV light. A 120 *mL* aqueous solution of methyl orange (10 mg/L) dye was prepared in DI-water. 85 *mg* of ZnO nanoparticles was suspended into the dye solution as photocatalyst. For proper homogeneity of the photocatalyst and to preserve the absorption-desorption equilibrium, the solution was ultra-sonicated for 30 *min* in a dark place and then irradiated by UV light. The samples were withdrawn within 20 *min* interval and after the UV irradiations the photocatalysts were removed from these solutions by centrifugation with 1200 *rpm* for 5 *min*. Finally, the absorption spectra of the samples were taken by using UV-Vis-NIR spectroscopy in the wavelength range of $200 - 800$ *nm* with DI-water as the reference medium.

The degradation rate was calculated using the following formula [120], [138]-[140]:

$$Degradation\ percent = \frac{C_0 - C_t}{C_0} \times 100(\%), \tag{6.2.1}$$

where C_0 is the primal concentration of MO solution and C_t is concentration at different UV irradiation time.

Characterization Techniques

X-ray diffractometer (XRD) (PANalytical X' Pert^3 Powder) was used to identify the crystallite phase and to estimate the crystalline size. The morphology was characterized by field emission scanning electron microscope (SEM) (FE-SEM, Nova Nano SEM 450). The optical absorption were measured by ultraviolet-visible-infrared (UV-Vis-IR) spectroscope (UV-3600 plus, Shimadzu). EDX to determine the composition of the synthesis sample. The photocatalytic performance of the prepared samples were evaluated by the same equipment and all measurements were carried out at room temperature.

6.3 Results and Discussion

6.3.1 XRD Patterns of ZnO Nanoparticles

The crystal structures of ZnO nanoparticles are confirmed by X-ray diffraction with Cu Kα radiation and the pattern recorded in the 2θ range from 25^o to 75^o operating at 40 KV and 40 mA as shown in Fig. 6.1(a). It has been found that all the major diffraction peaks are perfectly indexed to the hexagonal wurtzite structure of ZnO. In this pattern, the peaks (position are the same i.e., overlap with each other) are detected at angles of 2θ around 31.75^o, 34.43^o, 36.25^o, 47.55^o, 56.60^o, 62.90^o, 66.45^o, 67.98^o and 69.08^o corresponding to the lattice planes (100), (002), (101), (102), (110), (103), (200), (112) and (201), respectively, which are in good agreement with those of powder ZnO obtained from the International Center of Diffraction

Samples	Cr. size for plane $hkl = 101$, (nm)	Spacing $d_{101}(\mathring{A})$	Average size D (nm)
RP	30.25	2.211	27.01
SG	23.84	2.215	22.37
OL	10.34	2.218	10.65
MILT	20.74	2.216	20.72
AFC	21.40	2.214	19.67

Table 6.1: Crystallite size for a particular plane (D at $hkl = 101$) (2^{nd} column), interplanar spacing at d_{101} (3^{rd} column) and average crystallite size (D) (4^{th} column) of ZnO NP.

Data card (JCPDS-36-1451) confirming the formation of a crystalline structure. No extra diffraction peaks of other phases were detected, indicating the phase purity of the ZnO nanopowder. The average crystallite size of the ZnO NPs were calculated using Debye Scherer formula Eq. (3.3.1) and listed in Table (6.1). The variation in the average crystallite size of ZnO NPs may be due to the duration of calcination temperature, the procedure of synthesis and plant extraction solution. All ZnO NPs possess wurtzite crystalline structure with lattice parameters shown in Table (6.1). The structure of ZnO can be simply described as a number of alternating planes composed of tetrahedrally coordinated Zn^{2+} and O^{2-} ions, stacked alternately along a certain axis. The lattice constants 'a' and 'c' related to the spacing 'd_{hkl}' for wurtzite structure of ZnO have been calculated according to Eq. (6.3.1).

$$d_{hkl} = \frac{ac}{2}\sqrt{\frac{3}{c^2(h^2+hk+k^2)+3\frac{(al)^2}{4}}}, \tag{6.3.1}$$

where h, k and l are the Miller indices, d is interplanar distance.

According to Eq. (6.3.1), the spacing for a particular plane d_{101} are summarized in third column of Table (6.1). It is seen that the decomposition of the biological matter is complete due to the lack of Bragg reflexes at low scattering angle and amorphous

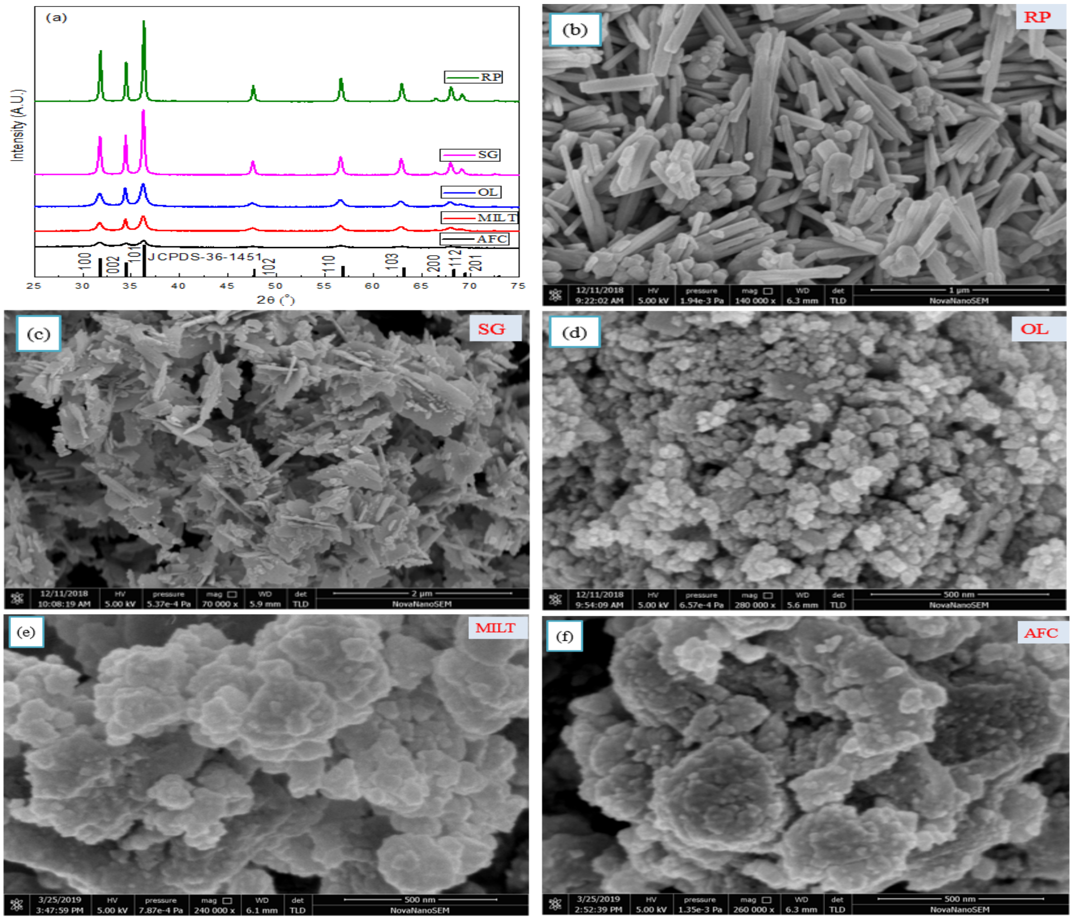

Figure 6.1: XRD pattern (a) and SEM image of ZnO NPs (b-f).

humps at the scattering angles of ZnO.

6.3.2 SEM Analysis

The morphology of the synthesized ZnO NPs are observed with the aid of Nova Nano SEM (NN-SEM) at different magnification for 5 kV applied potential as shown in the Fig. 6.1(b-f). The different shape of the ZnO NP formed from different precursors seem to be aggregated and have hexagonal shapes and facets. The ZnO NP synthesized by green synthesis method have been presented using a higher magnification of $\sim 250,000\times$ and it is clearly evident that there is a lot of agglomeration due to possibly to week Van Der Waal interactions. The agglomeration occurred probably during the process of drying. The morphology of ZnO NP prepared by biological route is spherical, sheet-like and grain-like, respectively, for OL, $MILT$ and FAC. The morphology of the other samples are rod-like and sheet-like for rapid (RP sample) and sol-gel (SG sample) routes, respectively, which are very best quality for photocatalytic application due to their site of interaction with incident light.

6.3.3 Optical Spectroscopy of ZnO Nanoparticles

The UV-Vis absorption peaks of ZnO NPs were recorded with UV-Vis spectroscopy in the wavelength region of $200-800$ nm at room temperature. Finally, the absorption spectra of ZnO NPs were analyzed using *origin* 8.5 software. As shown in Fig. 6.2, all the fine grounded powder samples absorb the radiations in the UV range up to 366.50 nm. This confirms the presence of ZnO nanoparticles which absorbed light in the UV spectral region and almost all the visible spectral radiations are transmitted by the samples. The UV emission refers to the recombination between the conductive band and the valence band of free excitons and is termed near-band-edge emission (NBE). Figure 6.3, shows the Tauc plots for different samples, which were applied to determine the optical band gap energy (E_g) of the ZnO nanoparticles. The energy band gap of the prepared samples are estimated using Tauc relation [141, 142]:

$$\alpha h\nu = A(h\nu - E_g)^n. \tag{6.3.2}$$

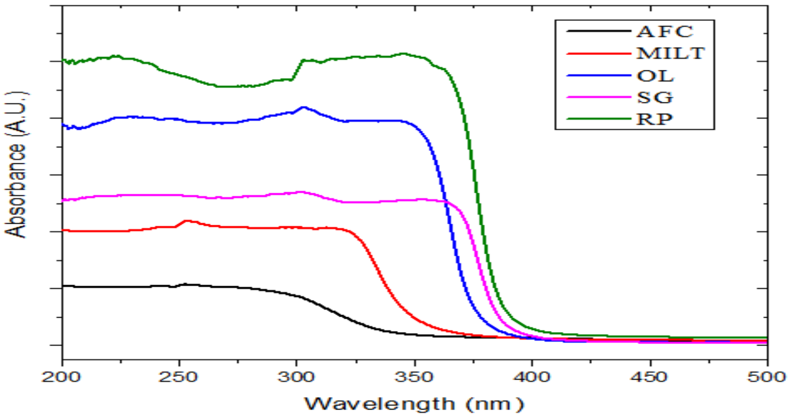

Figure 6.2: UV-Vis absorption spectra of ZnO nanoparticles synthesized via three routes from the same precursors.

where A, h, ν, α and E_g are a constant, Plank's constant, frequency of the incident photon, optical absorption coefficient, and the band gap energy of semiconductor, respectively. The constant 'n' correspond to direct ($n = 1/2$) and indirect ($n = 2$) band gap semiconductor [141, 143].

The band gap energy of the ZnO NPs can be determined by extrapolating the curve drawn between $h\nu$ against $(\alpha h\nu)^2$. As depicted in Fig. 6.3, the band gap energy obtained by extrapolating the curve is found to be approximately 3.19 eV, 3.04 eV, 3.26 eV, 3.18 eV, and 3.11 eV for RP, SG, OL, $MILT$ and AFC samples, respectively. This variation in band gap might be due to various factors such as structural parameter, carrier concentration, size, and induced defects [144].

6.3.4 Photocatalytic Degradation Studies for ZnO Nanoparticles

Figure 6.4 shows the percentage of photocatalytic degradation of MO dye solution with 85 mg of ZnO NPs under UV-light irradiation. The characteristic absorption

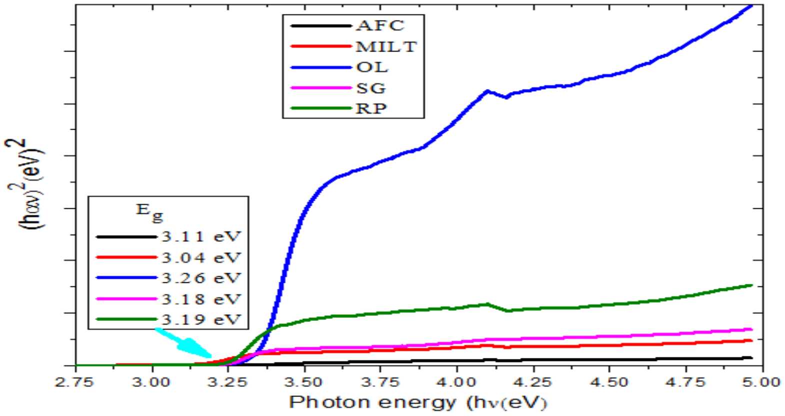

Figure 6.3: The band gap energies plotted as $(\alpha h\nu)^2$ Vs $h\nu$ of zinc oxide nanoparticles.

peaks of MO around 463 nm are monitored for different UV exposure time. It can be seen from Fig. 6.4(a), the samples AFC, $MILT$, OL, SG and RP have 31.61 %, 40.92 %, 20.23 %, 88.14 % and 93.71 % percent of photodegradation respectively at 120 min UV-light irradiation time as summerized in Fig. 6.4(c).

ZnO NPs have high binding energy than other transparent conducting oxides (TCO) which persist the event of excitonic absorption and recombination between electron and hole even at room temperature [145]. This process is enhanced with the nature of a direct band gap electronic structure due to their high absorption coefficient which favors increased photo-absorption and thus enhances the efficiency of photo-generated electron transfer. When UV irradiated, ZnO nanostructured photocatalysts are excited to produce a pair of electrons and holes. The oxygen molecules adsorbed on the photocatalyst interacts with ZnO to form superoxide anion radicals ($\bullet O_2^-$). Surface hydroxy groups react with holes in the valence band of ZnO leading to the formation

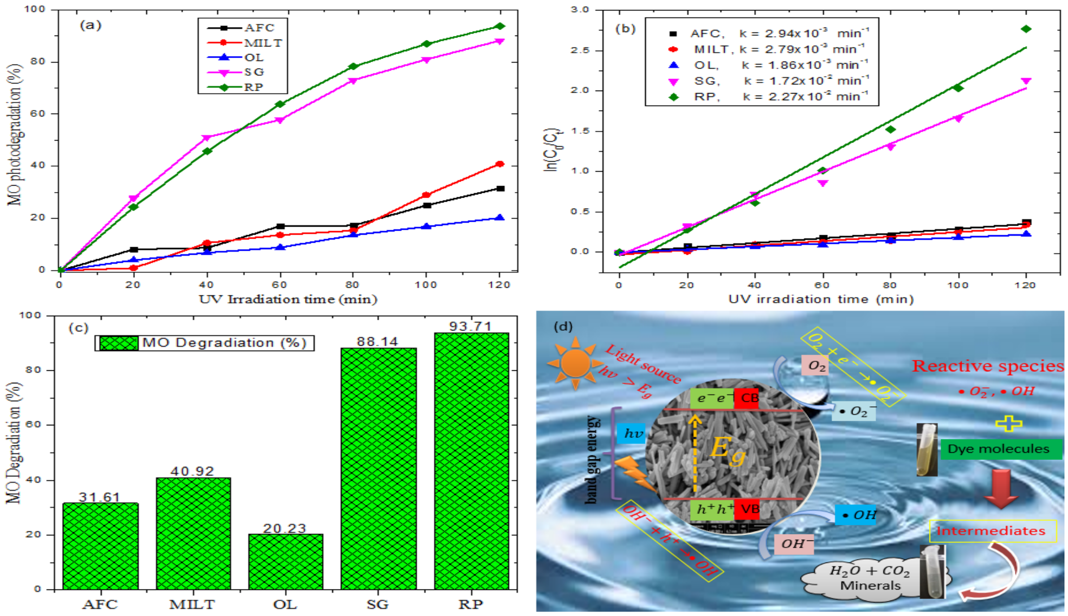

Figure 6.4: Percentage of degradation (a), photocatalytic activity (b), the summary of percentage of degradation (c) and photocatalytic activity (d) of zinc oxide NPs, and schematic of mechanism for MO degradation over ZnO NPs under UV irradiation.

of highly reactive hydroxyl ($\bullet OH$) radicals. The hydroxyl radicals ($\bullet OH$) and superoxide radicals ($\bullet O_2^-$) react with the dye molecules adsorbed on the photocatalyst surface and lead to their photocatalytic degradation. The mechanism is schematically depicted in Figure 6.4(d) and the possible corresponding reactions taking place are summarized as follows:

- $ZnO + h\nu \rightarrow e^-(CB) + h^+(VB)$,
- $e^- + O_2 \rightarrow \bullet O_2^-$,
- $h^+ + OH^- \rightarrow \bullet OH$,
- $\bullet\, OH + organic\ dye \rightarrow degradation\ products$,

- $\bullet O_2^- + organic\ dye \rightarrow degradation\ products.$

The photocatalytic application of ZnO NPs depend on the morphology, size and shape intrinsic defects as well as method of preparation. As shown in Fig. 6.4, rapid synthesis of ZnO NP has good photocatalytic degradation for the rod-like shape than the other samples. In photocatalytic analysis, rod-shaped nanoparticles demonstrate the best photocatalytic efficiency due to the large ratio of surface to volume. These different morphologies has been found to be greatly influenced on the time rate of photocatalytic activity [146].

The degradation of organic dye (MO) on the surface of photocatalyst can be described by pseudo-first-order degradation kinetics. The degradation/reaction rate constant can be determined by the following formula [147, 148]:

$$kt = ln(C_0/C_t), \tag{6.3.3}$$

where k is the photocatalytic degradation constant (photocatalytic activity) and t is a time of degradation.

From the logarithmic expression Eq. 6.3.3, the photocatalytic activity is obtained from the graph of $ln(C_0/C_t)$ versus irradiation time (t) as shown in Fig. 6.4(b). The degradation rate of our sample is obtained from the slope of the fitting curve (i.e., k). The photocatalytic degradation rate constant ($2.27 \times 10^{-2}\ min^{-1}$) of rod-like ZnO NP (RP) is larger and around 7.79, 8.14, 12.20 and 1.32 times the others degradation rate constants: AFC, $MILT$, OL and SG, respectively.

6.4 Conclusions

ZnO NPs have been fabricated for use in various field of applications such as photocatalytic, solar cell, biological/medical, cosmetics due to their unique properties. In this work, ZnO NPs with different morphology were synthesized by three cost-effective, non-toxic, and ease to control and scale up methods: rapid, sol-gel and green synthesis. The photo-degradation of nanomaterial highly depend on the morphology, band gap energy, and electron-hole recombination rate; the photo-degradation of RP sample is more enhanced than the other samples due to its morphology. From the result of XRD and TEM, the particle size of the synthesized ZnO NPs using green synthesis method are small compared to the others.

Chapter 7

Rapid Synthesis of Triple Layered Cylindrical $ZnO@SiO_2@Ag$ Core-Shell Nanostructures for Photocatalytic Applications

7.1 Introduction

Recently, core-shell nanostructured (CSNS) materials have attracted great attention in various fields due to their unique electrical, catalytic, magnetic, plasmonic and optical properties. Due to quantum confinement effects, large surface-to-volume ratio of the constituents and the interaction between the constituents; core-shell nanoparticles (CSNPs) exhibit high thermal/chemical stability and high light harvesting ability with new and/or modified material properties [50, 83, 149, 150]. The properties of CSNPs can be modified by changing the constituent materials' geometry, core size, spacer, shell thickness, and the host-medium [51, 96, 151]. These new and/or modified properties of the CSNS materials have various potential applications; such as in bio-nanotechnology, enhanced optical devices, tailored magnetic devices, electronic and optical devices [152], bio-imaging systems, pharmaceutical analysis [153], energy storage materials [152]-[154], genetic engineering, dye sensitized solar cells (DSSC) [155] and many important catalytic processes [50, 156, 157]. The fabrication of CSNSs require careful selection of the core and shell materials with the aim to optimize the passivation and to reduce the structural defects induced by positive mismatch of their lattice parameters. Both double- and triple-layered core-shell nanostructures can be assembled from semiconductor, dielectrics, metal, or organic/inorganic in different possible combination [50, 96, 97].

Among the widely used types of core-shell structures is the zinc-oxide (ZnO) based nanocomposite. The wurtizite form of zinc-oxide (ZnO) has a wide band-gap of 3.37 eV and high exciton binding energy ($\sim 60\ meV$) at room temperature [92, 158]. In addition to these bulk material properties, ZnO nanoparticle exhibits a unique and controllable features which makes it suitable for a variety of new/additional potential applications in laser diodes, solar cell, field emission displays, field effect transistor, optoelectronics devices, gas sensor, photo-catalysis, antibacterial activity, ultraviolet laser [157, 159, 160]. Recently, much effort has been devoted to study ZnO as a promising photo-catalyst for the photo-degradation of waste water, owing to its high activity, ease of morphology control, low cost, abundance, and environmental friendly feature.

However, the drawback of ZnO NPs for photocatalytic is the large band gap and charge carrier recombination of the photo-generated electron/hole pairs that occurs within a few nanoseconds [5], [161]-[163] and hence its photocatalytic activity is relatively weak. On the other hand, silica (SiO_2) is used in many fields for applications like catalysis [5, 164], drug delivery, chemical sensor, biomedical [164, 165], which motivated us to synthesize and characterize core-shell nanocomposites consisting of ZnO and SiO_2. We believe that, this core-shell nanocomposite will enable us to achieve novel properties resulting from the synergic interaction of these two chemical components. In addition to providing large surface area and inhibit recombination of electron-hole pairs [162, 166], SiO_2 can also help to improve the dispersion properties of other third layer like noble metals on the surface and create new catalytic active sites due to the interaction between semiconductor photo-catalysts and SiO_2. The absorption threshold of SiO_2 core-shell nanocomposites span from the UV to visible light spectral regions. The absorption can be enhanced and extended by employing various techniques such as coating by plasmonic materials [83, 167]. The noble metals Ag, Cu, Au, and Pt are preferred as a coating materials due to the following reasons [46, 52, 153];

- they act as a trap
- assist separation of electron and hole pairs
- they have high chemical stability
- bio-affinity
- strong absorption of light

Particularly, for photocatalytic application the plasmonic Ag is used as a shell because it has high electrical and thermal conductivity, high work-function, non-toxicity, improved overall photocatalytic performance of its composite, and antibacterial characteristics [168]-[170].

In the present work, we report the photocatalytic application of plasmonic triple-layered $ZnO@SiO_2@Ag$ cylindrical-shaped core-shell nanostructures for the first time.

These rod-shaped nanocomposite samples were synthesized by combining three methods: rapid thermal decomposition, St$\ddot{o}$eber method, and precipitation. The plasmonic Ag shell has a great role for the enhancement of photo-degradation, chemical stability, reusability, and optical absorbance. The as-prepared samples were characterized by X-ray diffraction (XRD), scanning electron microscope (SEM), transmission electron microscope (TEM), X-ray photoelectron spectroscopy (XPS), and ultraviolet-visible (UV-Vis) spectrometer. The photocatalytic activity of the synthesized nanoparticles was analyzed by the photo-degradation of methylene blue (MB) (as a model for pollutants in waste water) under UV irradiation. To the best of our knowledge, plasmonic coated, rod-shaped triple layered $ZnO@SiO_2@Ag$ core-shell composite nanostructure for photocatalytic application has never been investigated and this forms the basis of this study and articulated in this chapter.

7.2 Materials and Methods

7.2.1 Materials

The materials used for the synthesis of $ZnO@SiO_2@Ag$ triple layered core-shell nanoparticles are zinc acetate dihydrate ($Zn(CH_3COO)_2 \cdot 2H_2O$, 99%), silver nitrate ($AgNO_3$, 99.8%), and tetraethoxysilane (TEOS) as precursor materials, ammonia solution (NH_4OH, 25%), sodium hydroxide ($NaOH$, 96%) and sodium borohydrate ($NaBH_4$) was used as reducing agent, cetyltrimethyl ammonium bromide (CTAB) was capping as well as stabilizing agent, absolute ethanol (EtOH), methylene blue (MB), and DI water.

7.2.2 Synthesis of Core-Shell Nanoparticles

A) ZnO Nanoparticles

Initially, samples of ZnO nanoparticles were prepared according to the procedures outlined in [135]. The zinc acetate dihydrate, $Zn(CH_3COO)_2 \cdot 2H_2O$ was used as a precursor material. 12 gm of $Zn(CH_3COO)_2 \cdot 2H_2O$ were placed into a silica crucible and calcined at 400 ^0C for two reaction times, 4 h and 12 h in a muffle furnace without any special atmospheric condition. Finally, the resulting samples were grinded using mortar and pestle to obtain ZnO NPs in powder form.

B) $ZnO@SiO_2$ Core-Shell Nanoparticles

The core-shell $ZnO@SiO_2$ nanoparticles were prepared by using Stöeber method. About 2 gm of the prepared ZnO nanoparticles were dispersed into a mixture of 20 mL ethanol, 9 mL deionized water, and 0.5 mL ammonia solution (25 %) under ultrasonic condition for 30 min, and then 0.5 mL of TEOS was added into the mixture. After a reaction time of 3 h, the precipitate was isolated by centrifuge and washed with ethanol and water several times. The as-obtained products were dried at 80 ^0C under vacuum for 2 h. The samples synthesized using the ZnO NPs with reaction times of 4 h and 12 h at 400 ^0C are labelled as $ZS4$ and $ZS12$, respectively. Both samples were grinded and prepared for the next triple layered CSNS.

C) $ZnO@SiO_2@Ag$ Core-Shell Nanoparticles

The triple-layered $ZnO@SiO_2@Ag$ NPs were synthesized from the prepared $ZS4$ and $ZS12$ samples using the precipitation method. About 0.7 $mmol$ of $ZnO@SiO_2$ NPs were dispersed in 50 mL deionized water using ultra sonication for 30 minutes. After sonication, 0.09 $mmol$ of CTAB was dissolved in the solution under constant stirring by magnetic stirrer, heated at 50 ^0C, and then cooled down gradually to room temperature. Then, 25 mL aqueous solution of 0.7 $mmol$ of $AgNO_3$ was slowly added drop-wise to the solution, the mixture was continuously stirred for about 1 h. Next, 25 mL aqueous solution of 0.7 $mmol$ of $NaBH_4$ were added to the resulting mixture with constant stirring to reduce the Ag NPs. Then, the solution was centrifuged with ethanol and deionized water. After centrifugation, the obtained product was dried over night in an oven at 80 ^0C. Finally, the synthesized materials were ground using mortar and pestle to obtain $ZnO@SiO_2@Ag$ NPs in powder form for characterization. The tripled-layered samples prepared using the $ZS12$ and $ZS4$ samples were labelled as $ZSA12$ and $ZSA4$, respectively.

7.2.3 Characterization of the Samples

To determine the crystalline phase and estimate the crystallite size of the prepared $ZnO@SiO_2$ and $ZnO@SiO_2@Ag$ NP samples, X-ray diffractometer (XRD) (PANalytical X$'$-pert^3 power) measurements were taken. The morphologies were characterized by using field emission scanning electron microscope (SEM) (FE-SEM, Nova Nano SEM 450) and transmission electron microscope (TEM) (JEOL TEM-2100F). The physical state and elemental composition of the composite investigated by X-ray photoelectron spectroscopy (XPS). And also, the optical absorption spectra were measured by ultraviolet-visible (UV-Vis) spectrophotometer (UV-3600 plus, Shimadzu). All the measurements were carried out at room temperature.

Photocatalytic Activity and Stability of the Samples

The photodegradation effect of methylene blue (MB) dye were used to investigate the photocatalytic activity and stability of the prepared $ZnO@SiO_2$ and $ZnO@SiO_2@Ag$

samples. Accordingly, 85 mg of these samples were suspended each into separate 100 mL aqueous solution of MB (10 gm/L) dye which were, in advance prepared using deionized water. Magnetic stirrer was also used to keep the solution chemically uniform (to make adsorption-desorption equilibrium) at dark place [171, 172]. The mixture was poured into the photoreactor. Samples were collected at regular time (20 min) intervals and were immediately centrifuged to remove particles for analysis. Finally, the UV-Vis absorption spectra of the purified solutions were measured in the wavelengths ranging from 350 to 800 nm.

Moreover, the photodegradation efficiency of methylene blue has been calculated applying Eq. (6.2.1); where C_0 and C_t are the concentration of MB dye at the initial time $t = 0$ and at a later time t, respectively.

7.3 Results and Discussion

7.3.1 XRD Patterns of ZnO Nanoparticles

The structure of the 'bare' and Ag-coated $ZnO@SiO_2$ core-shell nanoparticles were investigated by XRD analysis and the diffraction patterns were recorded in the 2θ range from 20^o to 73^o as shown in Fig. 7.1.

As shown from the XRD spectra that for both core-shell NP samples $ZS12$ and $ZS4$ (i.e., $ZnO@SiO_2$ NPs prepared at reaction times of 12 h and 4 h), the diffraction peaks are detected at angles 2θ of 31.75^o, 34.43^o, 36.25^o, 47.55^o, 56.60^o, 62.90^o, 66.45^o, 67.98^o and 69.08^0 corresponding to the lattice planes (100), (002), (101), (102), (110), (103), (200), (112), and (201), respectively. It is found that all the major diffraction peaks are well matched with the standard hexagonal wurtzite phase of ZnO (JCPDS

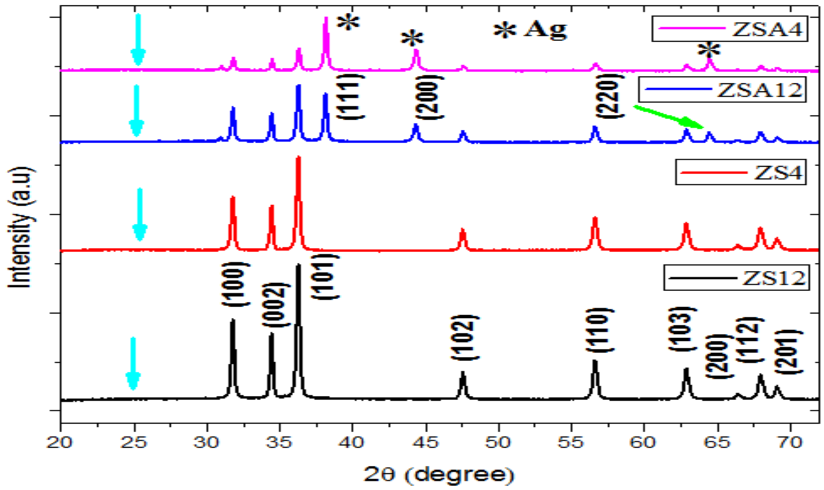

Figure 7.1: XRD pattern of $ZnO@SiO_2$ and $ZnO@SiO_2@Ag$ CSNPs.

Samples	Reaction time, $(hrs.)$	Average size, D (nm)
ZS4	4	25.04
ZS12	12	26.18
ZSA4	4	27.98
ZSA12	12	30.56

Table 7.1: Crystallite size of the nanoparticles prepared at a reaction temperature of 400 ^0C.

No. 36-1451, space group P63mc[186]) confirming the formation of a crystalline structure. Moreover, the diffraction peak of SiO_2 was expected around 25^o (indicated by blue arrow in Fig. 7.1), but no peaks were detected this is expected due to the high cohesive energy and the low recrystallization rates of SiO_2. This indicates that SiO_2 is amorphous does not change the structure of the core material [173].

In addition, Fig. 7.1 depicts the XRD pattern of the Ag-coated samples $ZSA12$ and $ZSA4$. Due to the Ag-coating of $ZnO@SiO_2$, additional diffraction peaks (JCPDS

No. 04-0783, space group-Fm-3m[225]) are observed at 2θ angles of 38.13^o, 44.30^o and 64.44^o corresponding to the Ag lattice planes (111), (200), and (220), respectively. In this pattern, no extra diffraction peaks of other phases are detected, indicating the phase purity of the composite powder. The result indicates that the core material is successfully modified with the shell material. Also, as shown in Fig. 7.1, the intensities are increased when the duration of reaction temperature is increased while it decreased when $ZnO@SiO_2$ is coated by plasmonic Ag. From this result, we understand that the crystallite or the atomic arrangement in the crystal is affected by temperature for prolong time [174]-[176]. In addition to the duration of reaction temperature, the intensity is decreased when the concentration of Ag is increased (see the result of EDS). The reason for this is that Ag nanoparticles may be dispersed in the structure of $ZnO@SiO_2$ or large amount of Ag is deposited at the surface of $ZnO@SiO_2$ [14].

The average crystallite size of the samples were calculated using Debye-Scherer formula Eq. (3.3.1). Accordingly, the estimated average crystallite sizes are about 26.18 nm, 25.04 nm for $ZS12$ and $ZS4$, respectively and for triple layered $ZnO@SiO_2@Ag$ are 27.98 nm and 30.56 nm for $ZSA12$ and $ZSA4$, respectively.

7.3.2 TEM Analysis

TEM analysis reveals whether the intended composite nanostructures are formed. In particular it aids in the conformation of the formation of a shell on the core surface of the SiO_2 shell [151]. The TEM images and the corresponding Energy-Dispersive X-rays Spectroscopy (EDS) analysis of the samples are shown in Fig. 7.2(a)-(f). It is observed that, SiO_2 NPs are successfully deposited on the surface of the rod-like ZnO NPs with thickness of around 6 nm and also the crystallite size of synthesized

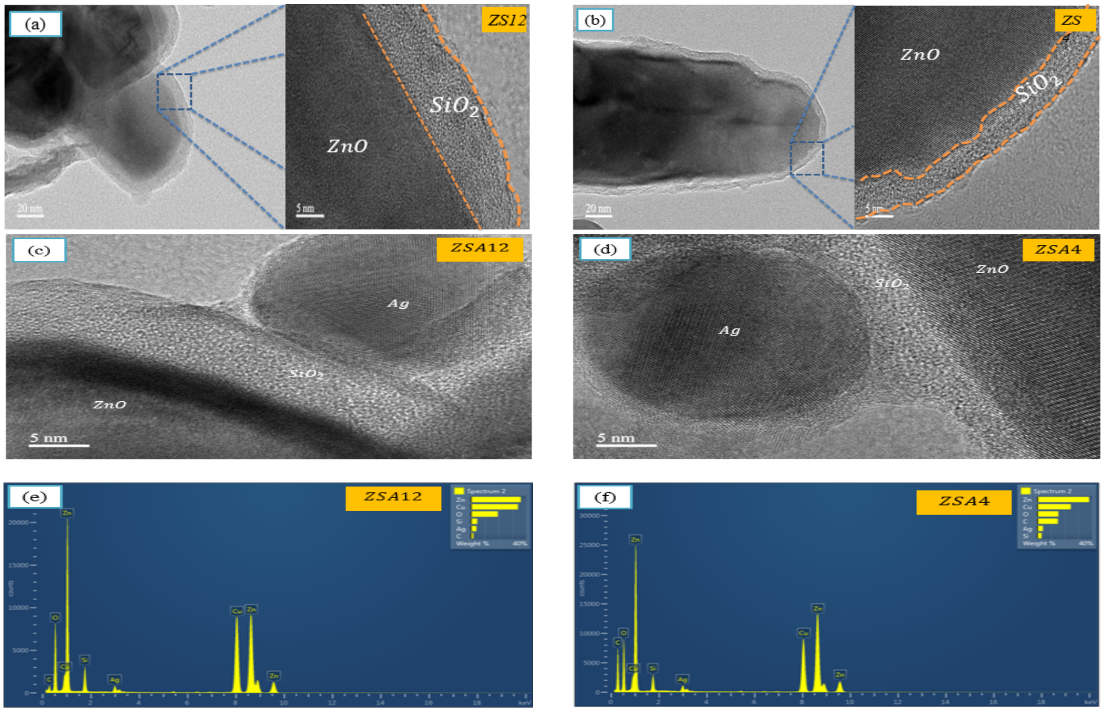

Figure 7.2: TEM image of $ZnO@SiO_2$ (a,b) and $ZnO@SiO_2@Ag$ (c,d) cylindrical CSNPs and EDS result of $ZnO@SiO_2@Ag$ (e,f).

nano-composite is confirmed to be in agreement with obtained by XRD. The Ag NPs deposited on the surface of $ZnO@SiO_2$ inner core-shell as in Fig. 7.2(c) and (d) are attributed to the electrostatic attraction between the Ag NPs and the CTAB functionalized SiO_2 NPs. However, in some regions the $ZnO@SiO_2$ inner CSNPs are found not to be 'fully' covered with Ag NPs which may due to the presence of interfacial interaction between the SiO_2 and Ag NPs.

Figures. 7.2(e) and (f) show the EDS spectra of the $ZnO@SiO_2@Ag$ CSNCs synthesized by coating the $ZS12$ and $ZS4$ samples with Ag NPs. The EDS analysis indicates the elemental composition of the prepared samples. From the Figures, it can be confirmed only Si (7.20 wt%, 5.24 wt%), Zn (55.65 wt%, 62.03 wt%), O (30.82

wt%, 25.85 wt%) and Ag (6.33 wt%, 6.88 wt%), respectively, for $ZSA12$ and $ZSA4$, elements are present in the synthesized material and there were no other impurities detected.

7.3.3 SEM Analysis of $ZnO@SiO_2@Ag$ Nanocomposite

The morphology of the prepared nanocomposites were studied by using scanning electron microscope (SEM) at different magnification for an applied potential 5 kV. Figure 7.3 (a)-(d), illustrates the SEM images of $ZnO@SiO_2$ and $ZnO@SiO_2@Ag$ CSNPs which were prepared at different reaction times. Due to the morphology of the initially prepared core material, the SEM images clearly indicate that the surface morphology of both $ZnO@SiO_2$ and $ZnO@SiO_2@Ag$ CSNPs are rod-shaped.

7.3.4 Optical Spectroscopy of Core-Shell Structures

UV-Vis-NIR spectroscopy is an important technique to investigate the optical properties of various forms of materials such as nanocomposites. The absorption spectra of the as-prepared $ZnO@SiO_2$ and $ZnO@SiO_2@Ag$ samples were recorded using UV-Vis-NIR spectrophotometer at room temperature as shown in Fig. 7.4. The UV-Vis spectra showed that all the four samples exhibited maximum absorbance peak at 363 nm, which conform to the well-known intrinsic band-gap absorption of the ZnO. Generally, the overall optical property is related to electron excitation from the valence band (VB) to the conduction band (CB), and it is used to evaluate the optical band gap energies of the samples. The energy band gap of the prepared samples are estimated using Tauc relation of Eq. (6.3.2); where $n = 0.5$. Then, the optical band gap energies of the samples were estimated from the $h\nu$- intercept in the plot of $(\alpha h\nu)^2$ versus $h\nu$. Accordingly, the band gap energies of double ($SA12$ and $ZS4$) and

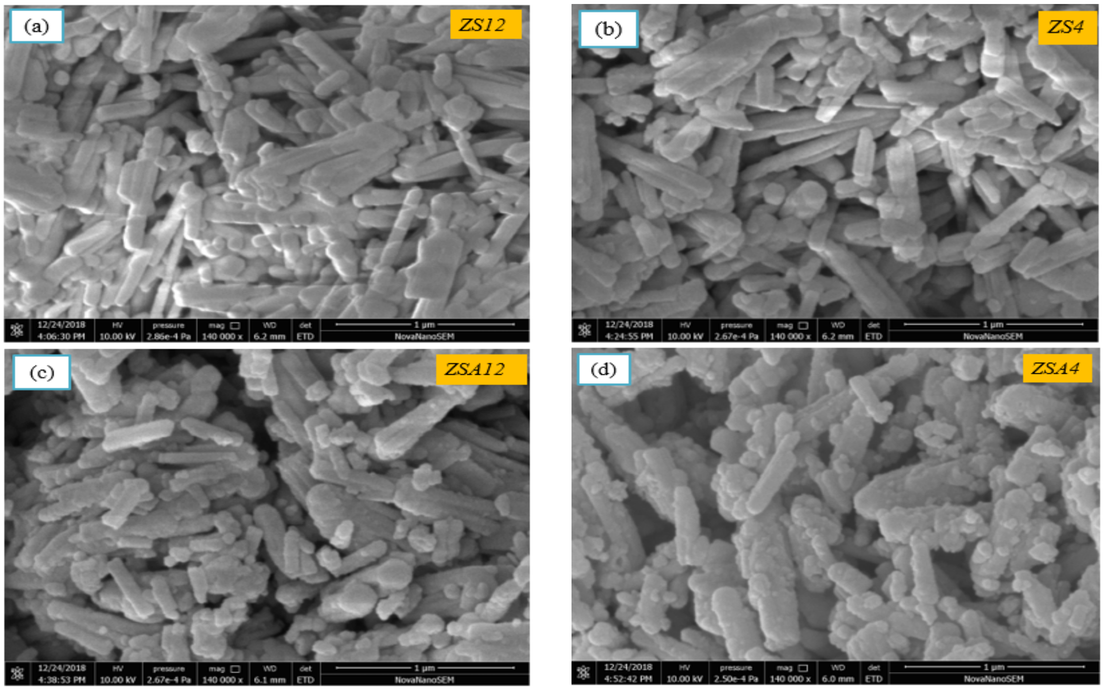

Figure 7.3: SEM image of $ZnO@SiO_2$ CSNPs ($ZS12$, $ZS4$) and $ZnO@SiO_2@Ag$ CSNPs ($ZSA12$, $ZSA4$).

triple layered ($ZSA12$ and $ZSA4$) core-shell nanostructure samples were found to be 3.21 eV and 3.13 eV, respectively. The band gap energy, morphology, photocatalytic response, and other properties of a certain matrical can be modified by doping, making core-shell, alloying. In this work, the band gap energies of double layered ($SA12$ and $ZS4$) core-shell composite nanostructures is decreased due to the presence of Ag as a coat.

7.3.5 X-ray Photoelectron Spectroscopy (XPS)

The surface element composition and chemical states of triple layered core-shell $ZnO@SiO_2@Ag$ nanostructures were studied by using XPS, as shown in Fig. 7.6.

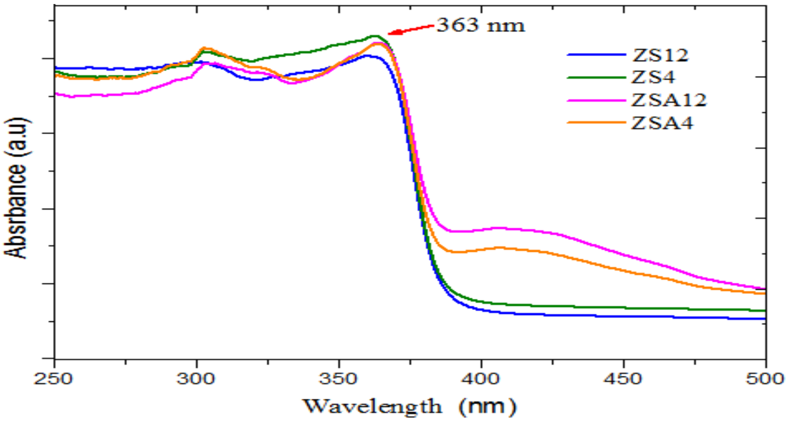

Figure 7.4: UV-Vis absorption spectra of $ZnO@SiO_2$ and $ZnO@SiO_2@Ag$ nanoparticles synthesized from two ZnO NPs which are calcinated at different time.

After calibrating the composite elements by the C 1s at 284.8 eV which is existed in the instrument [177], the survey scan XPS spectrum indicates the binding energies of Zn, Si, Ag, and O in the core-shell composite. The elemental composition of both ($ZSA12$ and $ZSA4$) composites are similar to the result obtained by EDS.

Figure 7.7(a)-(d) displays the high resolution of XPS spectra for Zn 2p, Si 2p, Ag 3d, and O 1s, respectively. Fig. 7.7(a), shows the binding energy of Zn 2p at 1046 eV and 1022.85 eV, which is attributed to Zn^{2+} in $ZnO@SiO_2@Ag$ ($ZSA12$) nanocomposite. For low reaction time of the composite ($ZSA4$), the binding energy is slightly shifted to the higher values due to low density of oxygen. In Fig. 7.7(b), the peak with the binding energy of 102.55 eV and 103.20 eV, respectively, for $ZSA12$ and $ZSA4$ are attributed to Si 2p, which represent the typical Si^{4+}. Similarly, in Fig. 7.7(c), the two peaks with the binding energies 373.30 eV and 367.30 eV are attributed to Ag 3$d_{3/2}$ and Ag 3$d_{5/2}$, respectively, of Ag nano-shell in $ZSA12$ composite. These two peaks for $ZSA4$ are shifted to higher energy values by 0.83 eV. The splitting of

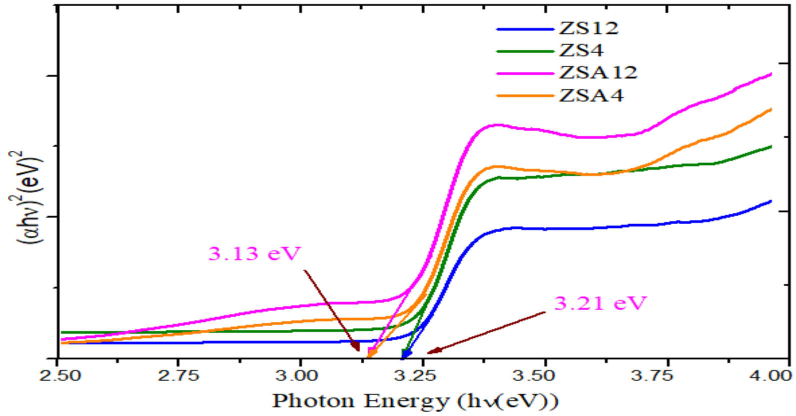

Figure 7.5: The optical absorption band gap energy estimated using Tauc's plot relation for $ZnO@SiO_2$ and $ZnO@SiO_2@Ag$ CSNPs.

the Ag $3d$ doublet at approximately 6 eV, confirms that Ag is present as Ag^0 in the synthesized triple layered CSNSs [169]. The peak associated to Ag $3d_{5/2}$ shifted to lower value relative to pure metallic Ag, this might be due to the interaction between Ag nano-shell and $ZnO@SiO_2$ core. As we have seen from the results, the XPS and the XRD data further confirmed the formation of Ag NPs in the nanocomposite. Fig. 7.7 (d) , shows the binding energy of O $1s$ at ~ 532 eV for both $ZSA12$ and $ZSA4$ CSNSs can be attributed to the metal bound oxide component (O^{2-}) of Zn^{2+} or Si^{4+}.

7.3.6 Photocatalytic Activity and Stability of the Samples

The evaluation of the photocatalytic activity of the synthesized double ($ZS12$, $ZS4$) as well as triple layered ($ZSA12$, $ZSA4$) core-shell nanostructures were carried out

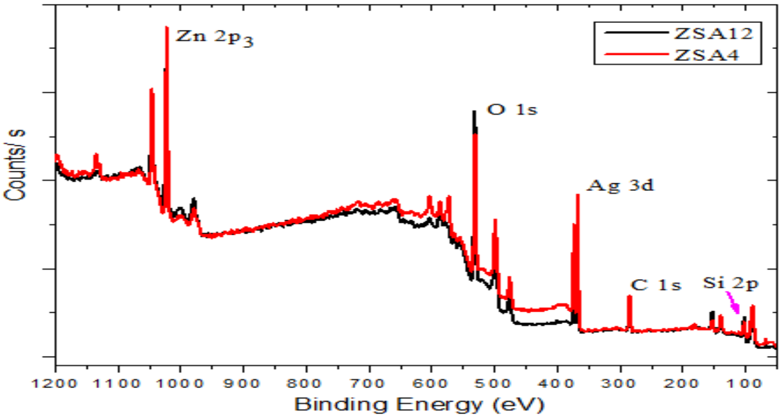

Figure 7.6: The survey scan XPS spectrum of $ZnO@SiO_2@Ag$ CSNPs.

using one of the important dyes, methylene blue (MB). Metallic shell Ag nanoparticles are used to make the synthesized nanocomposites chemically stable. The photocatalytic activity of the core-shell nanocomposite was evaluated by monitoring the degradation of MB in an aqueous solution, under irradiation of UV light. It is found out that as the irradiation time is increased, the maximum absorption decreased slowly and faded after 120 min of irradiation time, which indicates the discoloration of MB or remove of waste materials from polluted water.

When the nanocomposite solution is irradiated with energy equal to or greater than the band gap energy of the nanocomposite, electrons move to the conduction band (CB) to generate holes in the valence band (VB). The generation of electron-hole pairs due to UV irradiation leads to the formation of radicals, which are responsible for the degradation of organic pollutants [154, 178]. The possible photocatalytic

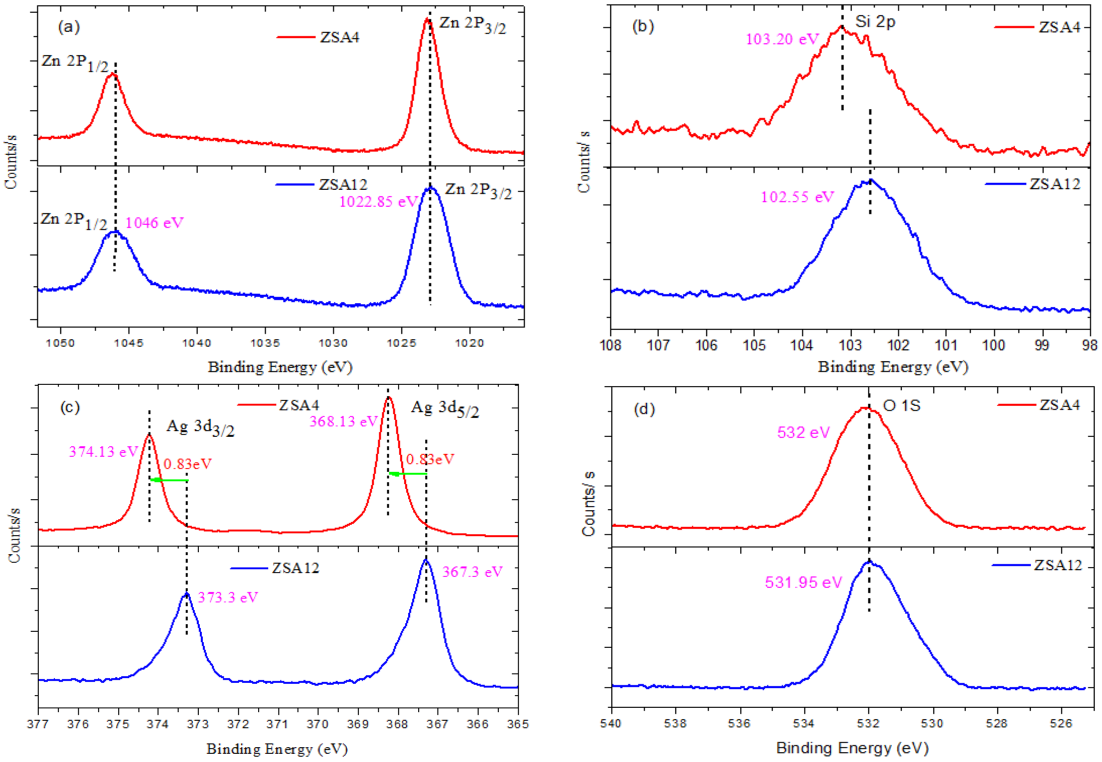

Figure 7.7: High resolution XPS spectra of (a) ZnO $2p$, (b) SiO_2 $2p$, (c) Ag $3d$, and (d) O $1s$.

reaction mechanism, for instance for the ZSA samples, can be described as follows:

$$
\begin{aligned}
ZSA + h\nu &\Rightarrow ZSA(e^-_{CB} + h^+_{VB}),\\
MB + h\nu &\Rightarrow MB^* + e^-_{CB} + h^+_{VB},\\
e^-_{CB} + O_2 &\Rightarrow \bullet O_2^-,\\
h^+_{VB} + H_2O &\Rightarrow H^+ + \bullet OH,\\
2 \bullet O_2^- + 2H_2O &\Rightarrow H_2O_2 + O_2 + 2OH^-,\\
H_2O_2 + e^-_{CB} &\Rightarrow \bullet OH + OH^-,\\
MB + h^+_{VB} / \bullet OH / \bullet O_2^- &\Rightarrow CO_2 + H_2O + other.
\end{aligned}
$$

Charge carriers are expected to be produced from both photocatalyst and MB dye. In this photodegradation reaction electrons from MB dye are injected to the CB of the catalyst. The photogenerated electrons and holes pairs are transferred to the surface and reacted with the absorbed reactants as shown in Fig. 7.8(d). The photogenerated holes and electrons from photocatalyst and dye are trapped, O_2 and H_2O. The reactions with these are produced radicals which are extremely strong oxidants for the degradation of organic chemicals.

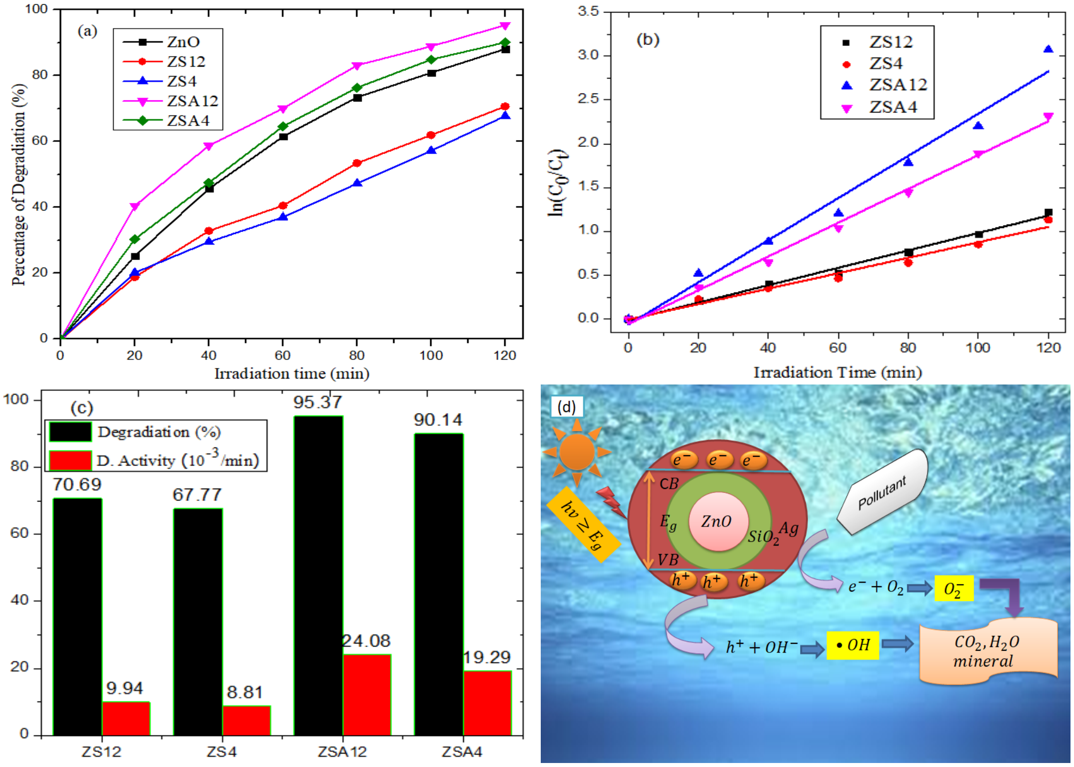

Figure 7.8: Percentage of degradation (a), photocatalytic activity (b), the summery of percentage of degradation (c) and photocatalytic activity (d) of double and triple layered CSNPs, and schematic of mechanism for MB degradation over triple layered CSNPs under UV irradiation light.

The absorption of photocatalytic solution is exponentially related with the irradiation time. The photocatalytic degradations of methylene blue (MB) in the presence of synthesized CSNPs, follow pseudo-first-order degradation kinetics described by [166, 179];

$$C_t = C_0 Exp(-kt), \tag{7.3.1}$$

where k is the photocatalytic degradation constant (photocatalytic activity) and t is a time of irradiation. As shown in Fig. 7.8(a), about 70.69 %, 67.77 %, 95.37 % and 90.14 % MB were degraded after 120 min for ZnO NPs, $ZS12$, $ZS4$, $ZSA12$ and $ZSA4$ core-shell nanostructures, respectively. As shown in the result, the photodegradation of the composite depend on the calcination time even for one constituent, i.e., for the core ZnO. In this case, both double - and triple - layered core-shell nanostructures which have their core material calcined for a long time, their photodegradation activity was found to be enhanced.

The enhancement of photodegradation activity of a certain catalyst was studied using the Langmuir-Hinshelwood kinetics model [180]. Here, to determine degradation rates from our data, the linear form of Eq. (7.3.1) is written as Eq. (6.3.3), where in this expression, k, is the slope. From this logarithmic equation, the photocatalytic activity is obtained from the graph of $\ln(C_0/C_t)$ versus t as shown in Fig. 7.8(b). The values of k for the samples $ZS12$, $ZS4$, $ZSA12$ and $ZSA4$ were found to be 9.94 $m(min)^{-1}$, 8.81 $m(min)^{-1}$, 24.08 $m(min)^{-1}$, and 19.29 $m(min)^{-1}$, respectively. The percentage of photocatalytic degradation and photocatalytic activity of both triple layered $ZnO@SiO_2@Ag$ CSNSs were summarized in Fig. 7.8(c).

7.3.7 Cyclic Stability of Triple Layered Core-Shell Nanostructure

A stable and re-usable photocatalyst has much more importance in the field of catalyst from the perspective economic and environmental objectives [14]. In this study, the cyclic stability of the as-prepared triple layered CSNS ($ZSA12$) for the photocatalytic degradation was evaluated for five catalytic runs. After separating the photocatalyst $ZSA12$ from the degraded solution by using centrifugation technique, the separated photocatalyst was washed with DI water several times and then dried in oven. The triple layered $ZnO@SiO_2@Ag$ CSNSs synthesized from $ZS12$, were re-used and the cyclic stability was evaluated. The cyclic stability of $ZnO@SiO_2@Ag$ CSNSs were evaluated by monitoring the photocatalytic degradation of the same dye MB under UV irradiation light. For the consecutive five cycles, we used photocatalyst separated from the preceding degraded solution. As shown in Fig. 7.9, it was found that the

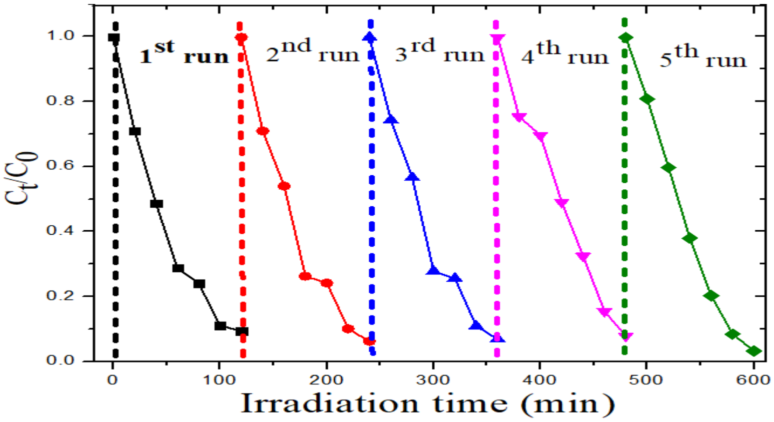

Figure 7.9: Cyclic photodegradation curve for the triple layered $ZnO@SiO_2@Ag$ CSNSs photocatalyst.

recycled triple layered CSNPs did not show any change in the photodegradation even after five cycles indicating that the photocatalyst has high chemical stability and does not photocorrode during the photocatalytic oxidation of the model pollutant molecules [171]. This new type of composite nanostructure has excellent photocatalytic stability and reusability than Ag doped ZnO [181]. Hence, the triple layered $ZnO@SiO_2@Ag$ CSNSs can be recycled and reused, which can be potentially used in practical applications.

7.4 Conclusions

In this work, the optical property and photocatalytic degradation application of triple layered core-shell composite nanostructure, ZnO as an inner core, Ag as a shell and SiO_2 as spacer between core and shell has been studied. The triple layered $ZnO@SiO_2@Ag$ cylindrical-shape core-shell composite nanostructures were synthesized by combining three methods: rapid thermal decomposition, st$\ddot{o}$eber and precipitation. The synthesized triple layered samples were characterized by X-ray diffraction (XRD) spectroscopy, transmission electron microscope (TEM), scanning electron microscope (SEM), X-ray photoelectron spectroscopy (XPS), and UV-Vis spectroscopy. From the result of these characterization techniques, double and triple layer core-shell composite nanostructures are successfully prepared with nano scale size. As confirm by TEM and XRD, the size of synthesized samples are in the range of 25 nm and 31 nm. The morphology and whether the samples are core-shell or not are characterized by TEM and SEM. Due to the presence of Ag as a coat over the double layer, the band gab energy is modified from 3.21 eV to 3.13 eV. The photocatalytic performance of the synthesized nanostructures was investigated by the decomposition of methylene blue solution. Due to interchange properties of constituents, the photocatalytic degradation of the composites are found to be enhanced in the UV spectral region. In the enhancement photodegradation, chemical stability, re-usability, and optical absorbance plasmonic shell Ag has a great role in the core-shell composite nanostructure. The formation of triple layered core-shell nanocomposite suppressed the recombination and promoted the separation of photogenerated the pairs of hole-electron. Finally, we note that triple layered core-shell nanostructure arrays may create the opportunity for broad band absorption and light harvesting applications.

Chapter 8

Enhancing the Photocatalytic Application of Bi Doped/Undoped TiO_2 Nanoparticles Using Ginger (Zingiber Officinale) Extract

8.1 Introduction

Green nanotechnology is the fastest growing segment in the field of nanoscience and nanotechnology. Nanoscience and nanotechnology refers to the field of studies about the fabrication and design of materials under $< 100\ nm$ at least in one dimension and characterization of tunable size dependent properties for a wide variety of applications. Generally, green nanotechnology and nanoscience in nanotechnology to minimize potential environmental pollutant and human health risks and the use of nanotechnology products, using less energy during manufacturing process, the ability to recycle products after use, and to encourage replacement of existing products with the new nanoproducts that are more environmentally friendly.

Nowadays, the rapid expansion of the global economy and extension of industrial expansion in developing economies has been the enormous release of waste materials which portend harmful effects to the environment through pollution. Adverse consequences to affect human health and environment require mitigation trough eradication of these toxic materials. There are few methods to control the hazardous of these pollutants, among which photocatalysis is considered as an efficient, stable, and environmentally friendly method. So far, TiO_2 nanoparticles (NPs) have been widely used as photocatalyst in the photo-degradation of organic pollutants, due to its high photocatalytic activity in UV region, cost-effectiveness, good stability, availability, non-volatile, high electrical resistance, reusable, and non-toxicity [12, 176, 182, 183]. Due to the fast recombination of electron-hole pairs and wide band gap ($3.2\ eV$), the synthesized TiO_2 is not sensitive to visible light which accounts for 45 % of solar spectrum [18, 36, 184]. TiO_2 NPs were synthesized by various chemical and physical methods: sol-gel, precipitation, hydrothermal, solvothermal, chemical vapour deposition, and the like. But, these methods are costly, toxic, and energy consumer. However, green synthesis method is cost effective, eco-friendly, biocompatible, consumes less energy, and avoid adverse effects during their applications [185, 186].

TiO_2 can exist in nature in three distinct polymorphs: tetragonal $-$ anatase, orthorhombic $-$ brookite and tetragonal $-$ rutile. The brookite phase is generally unstable and extremely difficult to synthesize, making it thus attract of low scientific interest. The anatase and rutile phases occur naturally, but can be synthesized easily in the laboratory. These two crystal phase exhibit important differences. The rutile crystal structure being more compact than the anatase form, presents a high refractive index, a higher density and is the more stable form. But, anatase titania is mostly used for photocatalytic application, due to its large surface area.

Particularly anatase TiO_2 NP has low photocatalytic efficiency in visible light range and restricts its activity to the UV range [187]. To increase this efficiency and to make it sensitive to visible light, various methods have been used to enhance its absorption of the solar spectrum and to inhibit the recombination of photogenerated electron-hole pairs [187, 188]. A prominent approach is doping it with transition metals (such as; Ag, Fe, V, Cr, Mn, Cu, Co), basic metals (like; In, Bi, Ga) or nonmetallic elements (such as; S, N, C, B), [12, 189, 190], rare earth elements (such as, La, Ce, Er, Eu) to TiO_2 and $TiO_2 -$ based hetrostructures (like core-shell, alloying) [190, 191]. Among these, doping is the most effective due to the existence of oxygen vacancy states that are below the conduction band. Additionally the anatase phase allows for incorporation of impurities that generate donor and acceptors levels in the proximity of the band gap to promote visible optical absorption. Titanium dioxide (titania) is used for various applications, such as white pigment, gas sensor, corrosion protective and optical layers, solar cell, purification of the environment, photocatalytic, biomedical, antibacterial, cosmetics, pharmaceutical, electronics device [7, 192, 193]. By considering the novel properties and potential/versatile applications into account, efforts are being made for the synthesis of Bi-doped TiO_2 nanoparticles by using green synthesis method. Basic metal Bi is used to modify the photocatalytic activity of TiO_2 through the following instances;

- can narrow the band gap of TiO_2
- inhibit recombination of photoinduced charges
- improve the CO_2 adsorption ability.

Large number of nanoparticles are synthesized from different parts of plants (like: root, stem, leaf, fruit, flower), fungi, bacteria, yeast, algae, and enzymes extraction [194, 195]. TiO_2 NP also synthesized from different part of plants for different application, for instance; trigonella foenum-graecum [186] for antibacterial application, datura innoxia [196] for biological application, mangrove [192] for eco-toxic effect, glycosmis cochinchinensis [16] for photocatalytic evaluation and antimicrobial properties, jatropha curcas [142] for photocatalytic degradation, bacillus amyloliquefaciens [10] for photocatalytic activity.

Here, we synthesized Bi- doped pristine TiO_2 NPs by using ginger extraction. To the best of our knowledge till date, green synthesis of Bi- doped/undoped TiO_2 nanostructures from ginger extract solution for photocatalytic application is not reported. Ginger has a scientific name of *Zingiber Officinale Rosc*, which is widely used as cooking spice, traditional medicine around the world: like anti-nausea agent, to treat bleeding disorders, rheumatism and vomiting, cough and colds, inflammation and tumours [194]. Recent studies show that ginger has been used for the synthesis of various nanoparticles [197] for certain applications.

The photocatalytic degradation of organic and inorganic pollutants using various types of semiconductors has been studied by several researchers. The oxidative degradation of adsorbed colored organic or inorganic molecules is due to the positive indirect reaction of holes that are formed in the valence band of the semiconductor and then migrate to the surface of the catalyst and are involved in reactions of interfacial oxidation-reduction. The band gap was decreased, but on the scale of nanoparticles, thus reducing the recombination process.

In this work, we report the enhanced photo-degradation application of TiO_2 NPs by doping with basic metal Bismuth and using green synthesis method. In this investigation, we doped 3% and 5% of basic metal Bi into TiO_2 nanostructure. However, doping with more than this percentage of concentration the efficiency of photodegradation can be decreased due to the production of coexists of element with the consumption of hole and electron. For further modifying the photodegradation efficiency of Bi doped/undoped TiO_2 nanocomposite we used ginger extraction solution.

8.2 Materials and Methods

8.2.1 Materials

The synthesis of $Bi-$ doped and undoped TiO_2 nanostructures (NSs) using green synthesis method, was carried out with the following materials as is without further purification; Titanium butoxide ($Ti(OBu)_4$, 98%), Bismuth (III) nitrate ($Bi(NO_3)_3.5H_2O$, 99.0%), fresh and healthy ginger as stabilizing and reducing agent, ethanol, and DI-water.

8.2.2 Synthesis Methods

Preparation of Extracted Ginger Solution

Ginger was bought from local market of the People's Republic of China (PR. China). After removing the cover of fresh ginger, it was washed by DI water. 20 gm of this sample was cut into small pieces and crashed by mortar and pestle. The fine crashed ginger was added into 100 mL DI water and boiled until the color of aqueous solution changed from watery to yellowish. Then the mixture was cooled to room temperature and filtered with Whatman No. 1 filter paper. Finally, the extracted solution was place under room temperature (RT) for further investigation.

Green Synthesis of Pure TiO_2

The precursor of TiO_2, $Ti(OBu)_4$ was added drop wise to the mixture of 50 mL ethanol and 10 mL of extracted solution under constant stirring with $pH = 5$. The solution was stirred for 2 hr and that leads to a change of color from watery to yellow due to the presence of ginger extraction solution. After stirring, the solution was centrifuged under 7000 rpm for 5 min and rinsed with ethanol and DI water many times. Further dried overnight in an oven at 80 ^oC and sintered in furnace at 450 ^oC for 2 hr. Finally, green synthesized TiO_2 was grinded using mortar and pestle; for use for further investigation in the next section. To compare the effect of extraction solution, we synthesized $\mathrm{TiO_2}$ without adding extracted solution using the same procedure. In the next section of this Chapter, we denote the TiO_2 nanoparticles prepared from chemical and green synthesis method as 'CT' and 'GT', respectively.

Green Synthesis of Bi- Doped TiO_2

The procedure of green synthesis Bi doped TiO_2 using ginger extracted solution was carried out as follow. 10 mL of $\mathrm{Ti(OBu)_4}$ (the precursor of TiO_2) and the required amount (3% and 5% of Bi) of $Bi(NO_3)_3.5H_2O$ was dispersed in 20 mL ethanol and 5 mL of ginger extracted solution. Both solutions were stirred using ultrasonic stirrer for 20 min separately. Then the mixture of the two solutions were added drop-wise into 50 mL of water under constant stirring. And then loaded into an autoclave for hydrothermal treatment at 200 ^oC for 5 hr. The result product was filtered using centrifuge and washed with DI water several times. The filtered sample was dried over night at 80 ^oC and sintered at 450 ^oC for 2 hr. Finally, after calcination the green synthesized Bi-doped TiO_2 was ground using mortar and pestle for photodegradation study. To simplify the long notation, the samples synthesized from 3 % and 5% of Bi are denoted as $GB3T$ and $GB5T$, respectively.

8.2.3 Photocatalytic Degradation of Trypan Blue Dye

The photocatalytic performances of the green synthesized of Bi- doped/undoped TiO_2 were evaluated by the decomposition of trypan blue (TB) solution under visible light with vigorous stirring. Trypan blue is one of the important toxic azo and direct dye. It has been used extensively in the textile, food, and paints factory for dyeing and coloring [198]; the release of this compound to the environment as a waste, pollutes the environment. A 100 mL aqueous solution of trypan blue (10 mg/L) dye was prepared in de-ionized water. 85 mg of $Bi-$ doped/undoped TiO_2 nanoparticles was suspended into the dye solution as photocatalyst. The solution was ultra-sonicated for 30 min in dark place for proper homogeneity of the photocatalyst and to maintain the absorption-desorption equilibrium and then we irradiated the solution by visible light. The samples were withdrawn within 20 min interval and after the visible irradiations the photocatalysts were removed from these solutions by centrifugation at 1200 rpm for 10 min. Thereafter, the absorption spectra of the samples were taken by using UV-Vis spectrophotometer in the wavelength range of $350 - 800$ nm and DI water used as reference medium.

The degradation rate was calculated using Eq. (6.2.1); where C_0 is the primal concentration of TB solution before irradiation and C_t is the concentration of TB at different visible light irradiation time.

8.2.4 Characterization Techniques

X-ray diffractometer (XRD) (PANalytical X-pert^3 powder) was used to identify the crystalline phase and to estimate the crystallite size. The size and morphology was characterized by field emission scanning electron microscope (SEM) (FE-SEM, Nova Nano SEM 450). The optical properties of absorption and photocatlytic response of the composite were measured by ultraviolet - visible spectrophotometer (UV-Vis) (UV-3600 plus, Shimadzu), the physical state and elemental composition of the composite were investigated by X-ray photoelectron spectroscopy (XPS) (ESCALAB 250Xi), and phase shift and absorbance were characterized by Fourier transform infrared spectroscopy (FT-IR) (Shimadzu FTIR-8400S). All the measurements were carried out at room temperature.

8.3 Results and Discussion

8.3.1 XRD Pattern Analysis

X-ray diffraction (XRD) analysis was performed using powder X-ray diffractometer, using Cu Kα radiation ($\lambda = 1.540598$ $\AA$) and was working at $40kV/40mA$. It has been used to characterize and determine crystallinity of the as prepared powder. The XRD pattern of the chemically synthesized TiO_2 and the green synthesized of Bi-doped/undoped TiO_2 nanoparticles are shown in Fig. 8.1. The peak position of Bi- doped/undoped TiO_2 NPs for both synthesis methods is almost the same, but, the intensity of the green synthesized TiO_2 nanoparticles is larger than the other nanoparticles synthesized by chemical and green synthesis methods. We can observe that for the calcination of 450 ^oC, the formation of single phase and crystalline anatase. In the synthesis section, we kept the calcination temperature below 500 ^oC to get anatase crystalline, above this calcination temperature the anatase phase will lose its intensity and the rutile phase will rise at different position. It is clearly found that the prominent diffraction peaks 2θ of 25.29^o, 37.92^o, 48.08^o, 53.96^o, 55.12^o, 62.73^o, 68.88^o, 70.19^o and 75.26^o correspond to (101), (004), (200), (105), (211), (204), (116), (220), and (215) crystal face of anatase TiO_2. Additional peaks are not observed after doping Bi NP; the peaks associated with Bi NP are not observed, i.e., dominated by TiO_2 NP. The crystalline structure of nanoparticles is strongly related to the sharpness and width of peaks. The size of nanoparticle is inversely proportional to the width of the peak i.e., as the width of the peak increases, size of the nanoparticles decreases, which represents the presence of material in nonoscale. The crystallite size of nanoparticle is calculated by using Scherrer's formula, Eq. (3.3.1). By the help of this equation, the average crystal size of chemical synthesized TiO_2 and green synthesized TiO_2 NP is 17.13 nm and 17.33 nm, respectively. And also the average

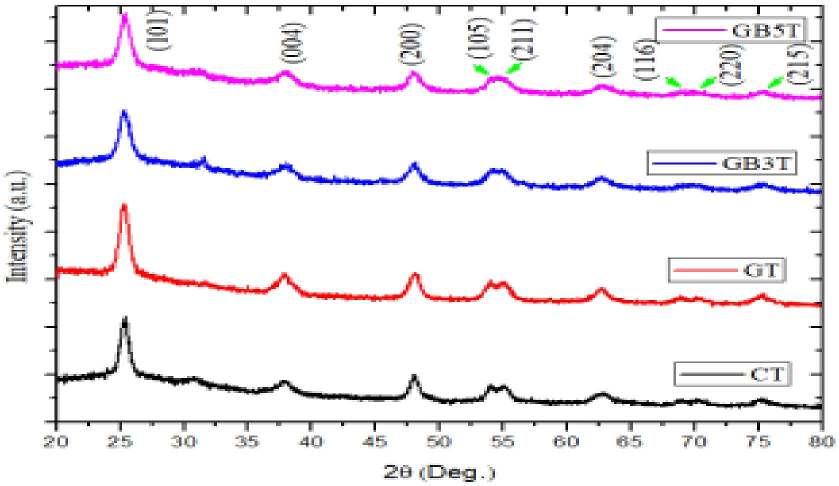

Figure 8.1: XRD pattern of $Bi-$ doped/undoped TiO_2 nanostructure using green synthesis and chemical synthesis route.

crystal size of $Bi-$ doped TiO_2 is 16.57 nm for $GB3T$ and 15.53 nm for $GB5T$. The lattice constants a and c related to the spacing d_{hkl} for tetragonal structure of TiO_2 have been calculated according to Eq. (8.3.1).

$$a = b = \frac{1}{\sqrt{3}} \frac{\lambda}{\sin(\theta)} \qquad \text{and} \qquad c = \frac{\lambda}{sin(\theta)}, \tag{8.3.1}$$

According to the above Eq. (8.3.1) the average lattice constants are $a = 0.24$ nm and $c = 0.42$ nm for chemically synthesized, $a = 0.24$ nm and $c = 0.41$ nm for green synthesized TiO_2 and $a = 0.23$ nm and $c = 0.40$ nm for both GB3T and GB5T. And by using Eq. 3.3.1, the spacing of Bi- doping and undoping TiO_2 at each Miller indices are summarized in Table 8.1.

The defect level of the given nanoparticles/nanocomposites is determined from the crystal size. The crystal imperfection or defect presence in the synthesized nanoparticle/nanocomposite was calculated by dislocation density (δ) and it is estimated by the following relation:

Table 8.1: Spacing and Miller indices of Bi- doped/undoped TiO_2 NPs.

hkl	CT, d_{hkl} ($\AA$)	GT,d_{hkl} ($\AA$)	GB$_3T$, d_{hkl} ($\AA$)	GB$_5$T, d_{hkl} ($\AA$)
101	18.48	18.86	10.24	10.24
004	10.33	10.54	5.73	5.73
200	10.33	10.54	5.73	5.72
105	7.67	7.83	4.25	4.25
211	7.67	7.83	4.25	4.25
204	7.31	7.46	4.05	4.05
116	5.96	6.09	3.31	3.31
220	5.96	6.09	3.31	3.31
215	5.68	5.79	3.15	3.15

$$\delta = 1/D^2, \tag{8.3.2}$$

where D is the crystallite size of the synthesized materials. The dislocation density δ of chemical synthesized, green synthesized TiO_2 NPs, GB3T and GB5T are 3.41×10^{-3} $(nm)^{-2}$, 3.33×10^{-3} $(nm)^{-2}$, 3.64×10^{-3} nm^{-2} and 4.15×10^{-3} nm^{-2}, respectively.

8.3.2 SEM Analysis of Bi- Doped/Undoped TiO_2

The morphology of the green synthesized Bi- doped/undoped TiO_2 nanoparticles confirmed by nano nova scanning electron microscope (NN-SEM). As shown in Fig. 8.2, the morphology of the particle is changed from 3D nanodot (nanosphere) to nanosheet when the dopant Bi concentration is increased. Nanostructures which have nanosheet morphology are recommended for photocatalytic application.

8.3.3 Fourier Transform Infrared Spectroscopy (FT-IR)

The presence of functional groups and the binding property of the Bi- doping and undoping green synthesized TiO_2 nanoparticles were determined by Fourier transform infrared spectroscopy (FT-IR) and were recorded in the range of $400 - 4000$ cm^{-1} as shown in Fig. 8.3. As depicted in figure, the absorption band appears between the frequency region $400 - 1200$ cm^{-1} corresponding to $Ti - O - Ti$ bond. The absorption peak around 3431.74 cm^{-1} is due to the presence of OH group. The slight shift of the peak position confirms the successful incoporation of metal Bi in TiO_2 nanostructures and the interaction between TiO_2 and the extraction solution.

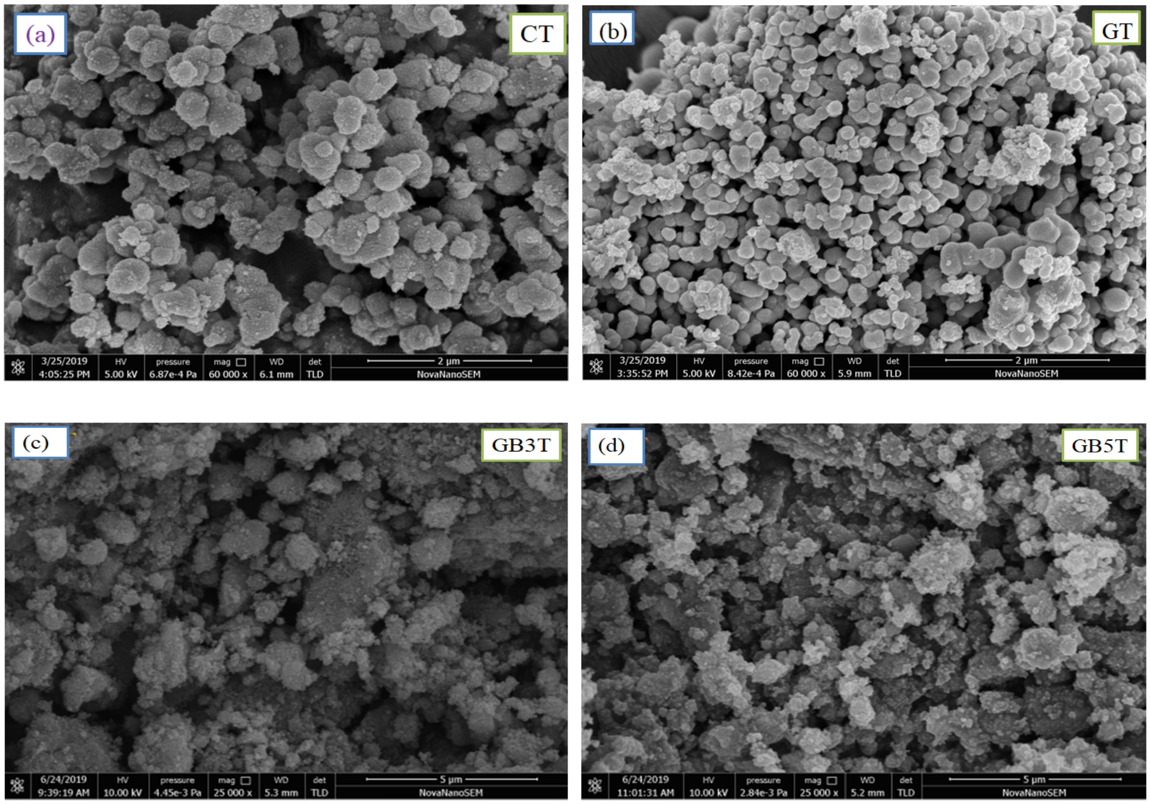

Figure 8.2: SEM image of $Bi-$ doped/undoped TiO_2 nanostructure using green synthesis and chemical synthesis method.

8.3.4 Chemical Stability of Bi- Doped TiO_2 Nanoparticles

The X-ray photoelectron spectroscopy (XPS) spectrum was obtained to study the surface composition and chemical states of green synthesized Bi-doped TiO_2 nanoparticles. The survey XPS spectrum of the nanocomposite verified the existence of elements; Bi, Ti, and O as shown in Fig. 8.4 (a). All binding energies of all elements were referenced to the C 1s peak at 284.60 eV of surface adventitious carbon. As

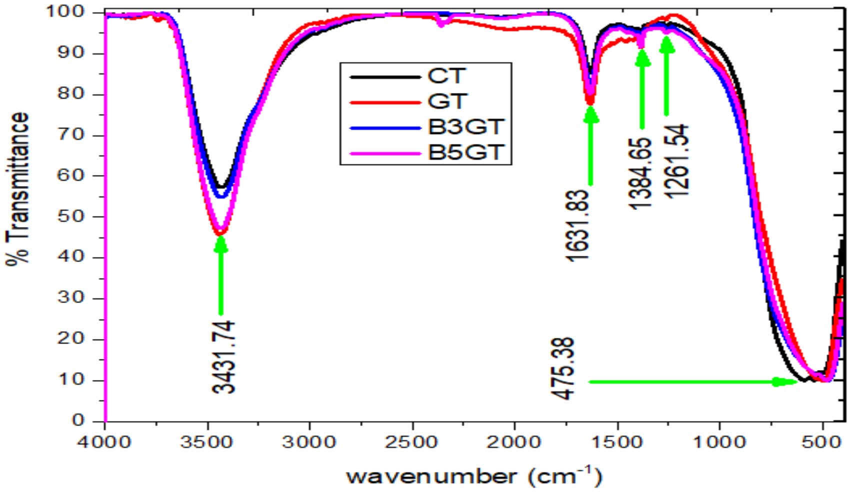

Figure 8.3: FT-IR spectra of Bi- doping and undoping green synthesized TiO_2 nanostructures.

illustrated in Fig. 8.4(b), the binding energies are 464.50 eV and 458.70 eV corresponding to spin-orbital spectrum of Ti $2p$ for Ti $2p_{1/2}$ and Ti $2p_{3/2}$, respectively. The Bi $4f$ XPS line (Fig. 8.4(c)) shows peaks centered at 164.55 eV and 159.25 eV corresponding to the binding energy of Bi $4f_{7/2}$ and Bi $4f_{5/2}$, respectively, indicating that the main chemical state of Bi in the composite was Bi^{3+} in this confirmation of the incorporation of the Bi in the lattice of TiO_2 and with this charge state where does it sit since Ti has a valence of +4. As depicted Fig. 8.4(d), O $1s$ peak could be divided into two different peaks at 529.93 eV and 531.02 eV. The first peak is due to the bond of $Ti-O$ and in the crystal lattice of TiO_2, whereas the second originates from the $Bi-O$ bond.

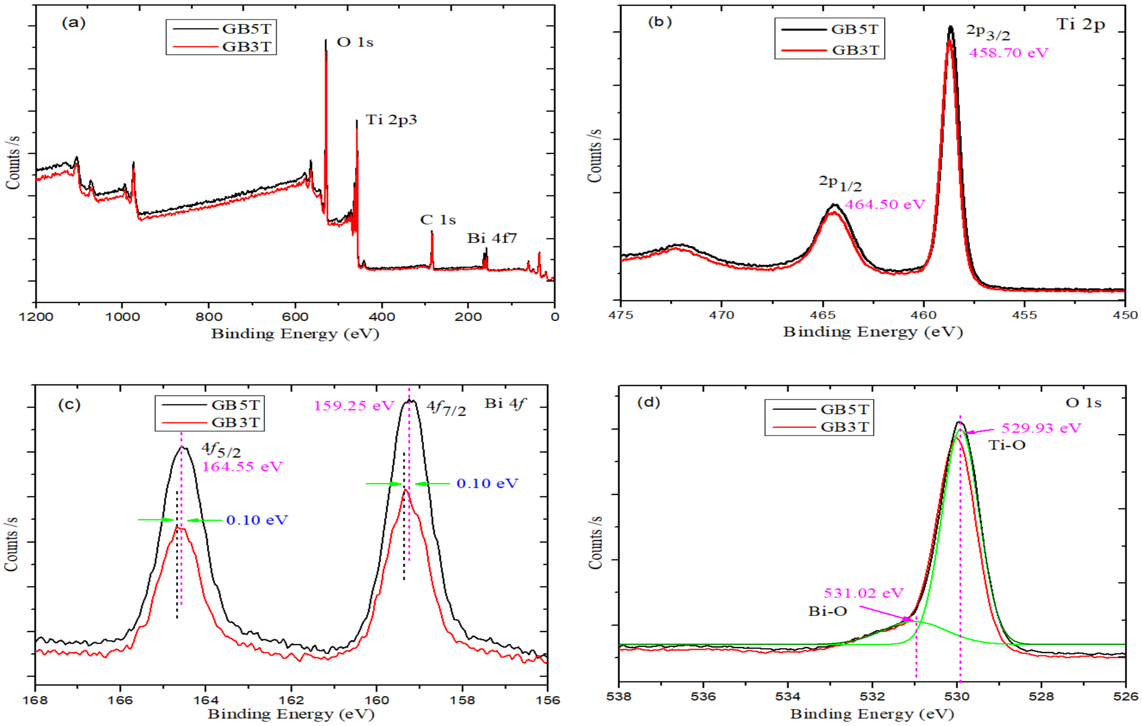

Figure 8.4: The survey scan XPS spectrum of (a) $GB5T$ and $GB3T$, (b) high resolution XPS spectra of $GB5T$ Ti $2p$ and $GB3T$ Ti $2p$, (c) $GB5T$ Bi $4f$ and $GB3T$ Bi $4f$, and (d) $GB5T$ O $1s$ and $GB3T$ O $1s$.

8.3.5 UV-Vis Analysis

UV-Vis spectrum was used to analyze the optical properties of the photocatalyst. The optical absorbance of Bi- doped/undoped TiO_2 nanoparticles analyzed using UV-Vis-NIR spectroscopy in the wavelength range of $200-800$ nm at room temperature and the absorbance was replotted using micro cal *origin* 8.5. As shown in Fig 8.5(A), the absorption band of green synthesized Bi- doped/undoped TiO_2 nanopaprticles is red-shifted relative to the chemically synthesized TiO_2, which clearly indicated the narrower band gap.

The band gap energy of green synthesized Bi- doped/undoped TiO_2 nanostructure was determined by using Tauc model according to Eq. (6.3.2), while taking $n = 2$ since the anatase phase is an indirect band gap semiconductor [190, 200].

The band gap energy of green synthesized Bi- doped/undoped TiO_2 nanoparticle can be determined by extrapolating the curve drawn between the incident photon energy ($h\nu$) and $(\alpha h\nu)^{1/2}$ as depicted in Fig. 8.5 (B). The band gap energy obtained by extrapolating curve to $\alpha = 0$ is found to be approximately 3.00 eV, 2.93 eV, 2.81 eV and 2.76 eV for CT, GT, $GB3T$ and $GB5T$, respectively. These variations are mainly due to ginger extraction solution and the substitution of Ti^{4+} by basic metal ion Bi^{3+} in the structure of anatase titania nanoparticle, which makes it an effective degradation of dye. The photocatalytic activity is increased under visible light as the band gap is reduced and then produce more electron-hole pairs under visible light.

8.3.6 Photocatalytic Activity

Under the irradiation of visible light, the degradation of trypan blue dye in the green synthesized Bi- doped and undoped TiO_2 nanoparticles was studied. The UV absorption of TiO_2 is shifted to visible absorption by doping narrow band gap metal Bi and by modifying the surface of TiO_2 with help of ginger extraction solution. The result obtained is shown in Fig. 8.6. As shown in this figure (Fig. 8.6 (A)), visible light absorption of green synthesized TiO_2 is enhanced than chemically synthesized due to the surface modification of TiO_2. And also by doping Bi, the photocatalytic degradation of TiO_2 is further enhanced with increasing the concentration of doped material. But, above this concentration of Bi the photo-degradation is decreased and

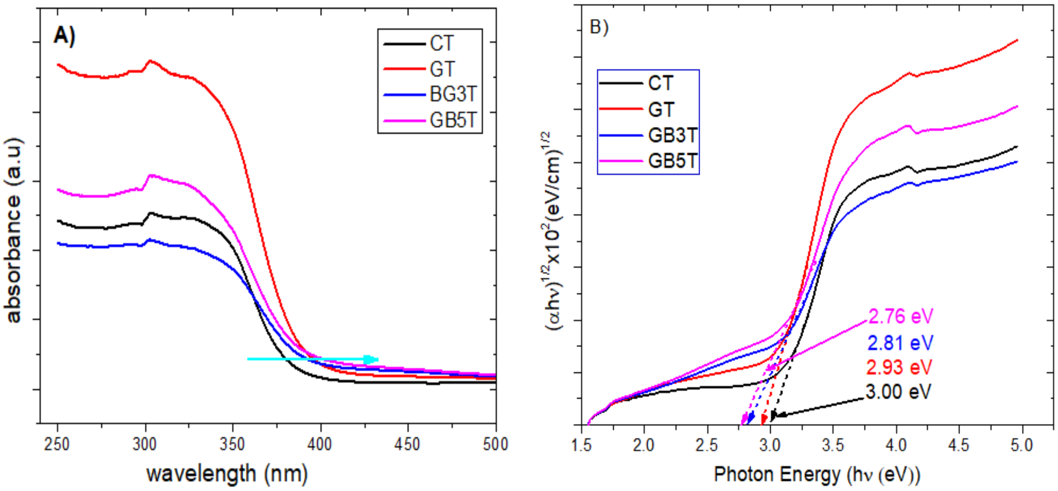

Figure 8.5: Optical absorbance (A) and band gap energy (B) of Bi- doping and undoping green synthesized TiO_2 nanostructures.

its photocatalytic performance can be diminished for visible light.

Ti vacancies were more dominant than the oxygen vacancies due to the presence of Bi. So, increasing Ti vacancies accompanied by oxygen vacancies could be responsible for the degradation process. According to this study, it can be concluded that the photocatalytic activity of TiO_2 NPs increase with dopant Bi, surface modification and increasing oxygen defect. The reaction between conduction-band electron and oxygen in the solution could generate the reactive oxygen species (ROSs) which is responsible for the color decolorization.

The photocatalytic elimination of TB with $Bi-$ doped/undoped TiO_2 NPs is expressed by the pseudo-first-order kinetic formula as written in Eq. (6.3.3).

From the logarithmic equation, Eq. (6.3.3), the photocatalytic activity is obtained from the graph of $ln(C_0/C_t)$ versus t as depicted in Fig. 8.6 (B). The degradation rate

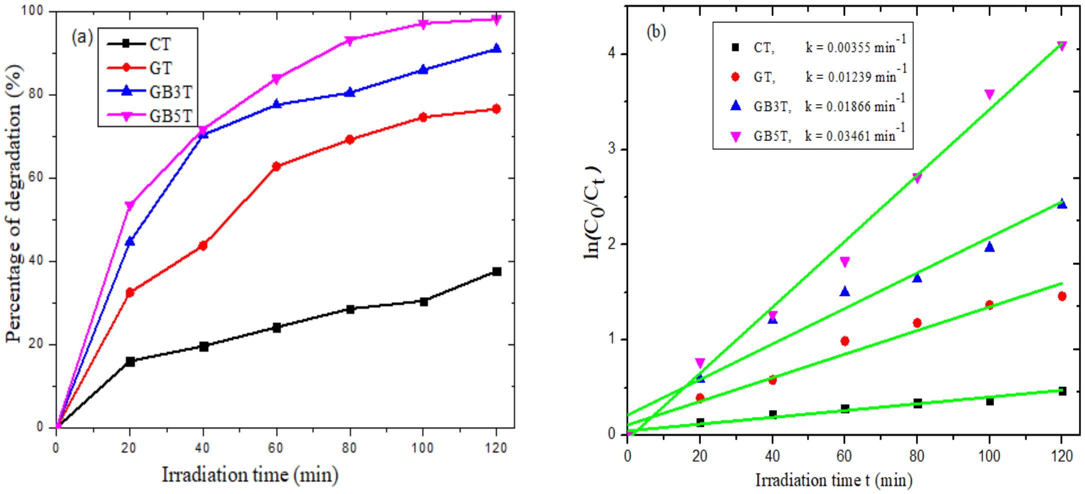

Figure 8.6: Efficiency of photo-degradation (a) and the photocatalytic activity (b) of green synthesized Bi- doped/undoped TiO_2 nanostructure versus irradiation time.

of our sample is the slope of the fitting curve (i.e., k). The photocatalytic activity of green synthesized TiO_2 (0.01239 min^{-1}) and $GB5T$ (0.03461 min^{-1}) is around 3 times and 10 times of chemically synthesized TiO_2 NP (0.00355 min^{-1}), respectively. Figure 8.7, schematically explains the mechanism of photocatalytic process on $Bi - TiO_2$ nanoparticles. In the dark, by dispersing $Bi - TiO_2$ nanoparticles in the TB solution, the surface electrons of the TiO_2 nanoparticles were transferred to the TB dye. The valance band electrons (e^-) in these nanoparticles under visible light radiation with the photons of energy greater than or equal to TiO_2 band gap (E_g), can be excited to the conduction band producing equal number of holes (h^+) in the valance band, simultaneously. Because the conduction band energy level of TiO_2 nanoparticles is higher than that of the Fermi level of $Bi - TiO_2$ nanoparticles, electrons can flow from TiO_2 nanoparticles to Bi nanoparticles. So, oxygen vacancy defects and Bi nanoparticles on the surface of TiO_2 nanoparticles trap electrons and prevents the recombination of $e^- - h^+$ pairs. Also, visible light radiation excites the dye molecules (TB^0 to TB$^+$). These TB molecules transfer electrons to the conduction band (CB) of TiO_2 (TB$^+$ to CB of TiO_2) and the Fermi level of Bi (TB^+ to Bi). CB electrons react to produce superoxide radicals ($\bullet O_2^-$) with dissolved oxygen in the solution, while the valence band (VB) holes react with hydroxide ions for the creation of hydroxyl radicals ($\bullet OH$) [201]. Both of these radicals are responsible for the decolorization of TB dye [154]. Also, the energy barrier of the $Bi - TiO_2$ junction prevented electron-hole recombination to separate photo-generated charges, effectively.

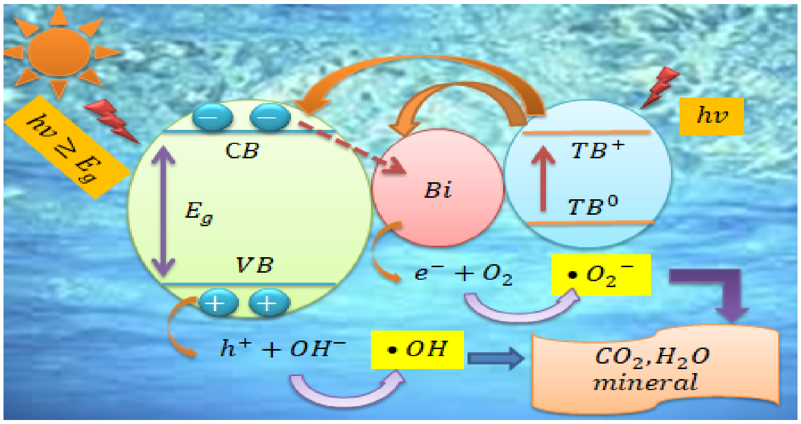

Figure 8.7: Schematic mechanism of photocatalysis process on $Bi - TiO_2$ nanoparticles under visible light irradiation.

8.4 Conclusion

The photocatalytic response of green synthesized Bi- doped/undoped TiO_2 nanoparticles is investigated by using ginger extraction solution and the photocatalytic performance was tested by the degradation of trypan blue dye under visible light radiation. The green synthesized Bi- doped/undoped TiO_2 nanostructure was characterized by X-ray diffraction, scanning electron microscope, FT-IR spectroscopy, UV-Vis-NIR spectroscopy, X-ray photoelectron spectroscopy, and the photocatalytic application characterized by UV-Vis spectroscopy. The photocatalytic activity as well as the band gap energy of TiO_2 modified by ginger extraction solution and doping with Bi. The photodegradation of green synthesized TiO_2 (76.66 %) is more enhanced than chemically synthesized (37.63 %) and further enhanced by doping basic metal Bi (98.34 %). The band gap energy is also found to decrease from 3.00 eV to 2.93 eV and 2.76 eV by using ginger extraction solution and by using both ginger extraction solution and Bi- doping, respectively.

Chapter 9

Conclusions and Future Work

9.1 Conclusions

In this dissertation work, we investigated theoretically, numerically, and experimentally the optical, plasmonic, and photocatalytic properties of various types of composite nanostructures. The plasmonic and optical properties of $ZnO@Ag$ spherical and spheroidal core-shell composite nanostructures are studied by employing the electrostatic-approximation by varying the parameters: core size, shell thickness, composite size/shape, and dielectric function of host medium. By varying these parameters, the plasmonic and optical properties: like: polarizability, refractive index, optical absorbance, absorption cross-section, and radiation efficiency are enhanced. Due to geometrical effect, the plasmonic responses for spherical and spheroidal composite is different; two plasmon resonances are observed corresponding to ZnO/Ag and Ag/host-medium interface, but, for spheroidal geometry additional two plasmon resonances are observed correspond to bonding/antibonding pairs due to separation of charges in the composites along the principal axes. The results obtained in this work may be utilized in various applications such as sensors, solar cell or photovoltaic technology, photocatalysis, and optoelectronics devices.

ZnO nanoparticle is synthesized by three different preparation techniques: sol-gel, rapid thermal decomposition, and green methods for photocatalytic application. The photodegration efficiency of the sample with absorbed methyl orange dye is different due to their band gap, morphology, electron-hole recombination rate. The morphology of ZnO nanoparticles prepared by green synthesis (biological route) is spherical in shape and very small in size.

The triple layered $ZnO@SiO_2@Ag$ cylindrical core-shell composite nanostructure were prepared by employing three synthesis techniques: rapid thermal decomposition (to prepare core material, ZnO), Stö̈eber (to prepared inner core-shell, $ZnO@SiO_2$) and precipitation (to synthesis final product, $ZnO@SiO_2@Ag$) for photocatlytic application. The photocatalytic performance of the prepared composite nanostructures was investigated by the decomposition of methylene blue solution. Due to the effect of combination, the composite is excellent for photodegradation, chemically stable, reusable, and optical absorbance.

Finally, the photocatalytic response of TiO_2 and Bi- doped/undoped TiO_2 is investigated and prepared by using green synthesis route (using ginger extraction solution) and chemical synthesis route. The photocatalytic activity of the synthesized sample is tested by trypan blue dye. The photocatalytic activity associated with band gap energy of TiO_2 is enhanced by ginger extraction solution and doping basic metal Bi in the structure.

The prepared samples were characterized by X-ray diffraction (XRD) spectroscope, scanning electron microscope (SEM), transmission electron microscope (TEM), ultraviolet visible (UV-Vis) spectroscopy, Fourier transform infrared (FT-IR) spectroscopy, X-ray photoelectron spectroscopy (XPS).

9.2 Future Work

The plasmonic and optical properties of core-shell composite nanostructures are not only dependent on the core size, shell thickness, composite size, composite shape, and host medium, but also depend on the material of the constituents, number of layer, and core shape. In addition, the photocatalytic properties of various types of composite nanostructures are investigated using green synthesis and chemical synthesis routes. However, these investigations have several topics that remain unsolved and further investigations need to be completed in order to produce quality materials. Therefore, our general future work should include:

- Plasmonic response of core-shape dependent $ZnO@Ag$ core-shell spherical, spheroidal, and cylindrical composite nanostructures embedded in passive and active host medium.
- Optical/plasmonic properties of multilayered $ZnO@Ag$ based core-shell composite nanostructures.
- The effect of concentration of extraction solution on the photocatalytic activity of ZnO nanoparticles.
- Photocatalytic response of triple layered $ZnO@SiO_2@Ag$ core-shell composite nanostructure with different morphology and different concentration of the constituents.
- The photocatalytic application of Bi doped TiO_2 based core-shell composite nanostructures with different concentration of extraction solution, dopant, core, and shell materials.

List of Publications

1. **Gashaw Beyene**, T. Senbeta, B. Mesfin, Ni Han, G. Sakata and Q. Zhang, "*Rapid Synthesis of Triple Layered Cylindrical* $ZnO@SiO_2@Ag$ *Core-Shell Nanostructures for Photocatalytic Applications*", J. Nanopart. Res. 22, 355(2020).
2. **Gashaw Beyene**, T. Senbeta, B. Mesfin, Q. Zhang, "*Plasmonic properties of spheroidal spindle and disc shaped core-shell nanostructures embedded in passive host-matrices*", Opt. Quant. Electron. 52, 157 (2020).
3. **Gashaw Beyene**, T. Senbeta, B. Mesfin, "*Size dependent optical properties of ZnO@Ag core/shell nanostructures*", Chinese J. Phys. 58, 235-243 (2019).
4. **Gashaw Beyene**, Ni Han, T. Senbeta, B. Mesfin, Zhu Lei, and Q. Zhang, "*Enhanced Photocatalytic Application of Bi doped/Undoped* TiO_2 *Nanoparticles Using Ginger (Zingiber Officinale) Extract*", Under review.
5. **Gashaw Beyene**, T. Senbeta, B. Mesfin, Ni Han and Q. Zhang, "*Synthesis and Characterization of Ultraviolet Emitter ZnO Nanoparticle Prepared Via Rapid, Sol-Gel and Green Method for Photocatalytic Application*", Submitted.

List of Publications not Include in the Thesis

1. **Gashaw Beyene**, "*Effect of spacer on size dependent plasmonic properties of triple layered spherical core-shell nanostructure*", AIMS Mater. Sci. 7(6) 788-799 (2020).
2. **Gashaw Beyene**, Gamachis Sakata, Teshome Senbeta and Belayneh Mesfin, "*Effect of Core Size/Shape on the Plasmonic Response of Spherical ZnO@Au*

Core-shell Nanostructures Embedded in a Passive Host-Matrices of MgF_2", AIMS Mater. Sci. 7(6) 705-719 (2020).

3. N. Han, Q. Xu, **Gashaw Beyene**, Q. Zhang, "*Enhanced photocatalytic activity over g-C3N4/(BiO)2(OH)xCl2-x Z-scheme heterojunction*", App. Sur. Sci. 521, 146464 (2020).

4. **Gashaw Beyene**, "*High Tunability of Size Dependent Optical Properties of ZnO@M@Au* ($M = SiO_2$, TiO_2, In_2O_3) *Core/Spacer/Shell Nanostructure*", Adv. Nano Res. 2 1-13 (2019).

5. **Gashaw Beyene**, "*Enhancing Optical Properties of Triple Layered Core-Shell Nanostructures*", J. Chem. Sci. Eng., 2(2), 90-93 (2019).

Bibliography

[1] A.K. Elyahb, C. Elise, W. Yongmei, H. Xiaohua, "*Synthesis and properties of magnetic-optical core shell nanoparticles*", RSC Adv. **7** , 17137-17153 (2017).

[2] L. Chen, et al. "*Biosynthesis of gold and silver nanoparticles from Scutellaria baicalensis roots and in vitro applications*", App. Phys. A **126**, 424 (2020).

[3] T.K. Pathak, R.E. Kroon, H.C. Swart, "*Photocatalytic and biological applications of Ag and Au doped ZnO nanomaterial synthesized by combustion*", vauum **157**, 508-513 (2018).

[4] A. Sadollahkhani, I. Kazeminezhad, J. Lu, O. Nur, L. Hultman, M. Willander, "*Synthesis, structural characterization and photocatalytic application of ZnO@ZnS coreshell nanoparticles*", RSC Adv.**4**, 36940 (2014).

[5] N.A. Galedari, M. Rahmani, M. Tasbihi, "*Preparation, characterization, and application of ZnO@SiO_2 core-shell structured catalyst for photocatalytic degradation of phenol*", Environ. Sci. Pollut. Res. **24**, 12655-12663 (2017).

[6] N. Daneshfar, K. Bazyari, "*Optical and spectral tunability of multilayer spherical and cylindrical nanoshells*", Appl. Phys. A 1**16**(2), 611-620 (2014.

[7] H. Li, J. Liu, J. Qian, Q. Li, J. Yang, "*Preparation of Bi-doped TiO_2 nanoparticles and thier visible light photocatalytic performance*", Chinese J. Catal., **35**, 1578-1589 (2014).

[8] T. Prakash, et al. "*Structural, morphological and optical properties of Bi-doped ZnO nanoparticles synthesized by a microwave irradiation method*", J. Mater. Sci.: Mater. Electron. **26**, 4913-4921 (2015).

[9] E.T. Seid, F.B. Dejene, "*Controlled synthesis of In-doped ZnO: the effect of indium doping concentration*", J. Mater. Sci.: . Electron. **30**, 11833-11842 (2019).

[10] R. Khan, M.H. Fulekar, "*Biosynthesis of titanium dioxide nanoparticles using Bacillus amyloliquefaciens culture and enhancement of its photocatalytic activity for the degradation of a sulfonated textile dye Reactive Red 31*", J. Colloid. Interface. Sci. **475**, 184-191 (2016).

[11] H. Taghvaei, M. Farhadian, N. Davari, S. Maazi, "*Preparation , characterization and photocatalytic degradation of methylene blue by Fe^{3+} doped TiO_2 supported on natural zeolite using response surface methodology*", Adv. Environmetal. Technol. **4**, 205-216 (2018).

[12] D. Sethi, R. Sakthivel, "*ZnO/TiO_2 composites for photocatalytic inactivation of Escherichia coli*" J. Photochem. Photobiol. B Biol. **168**, 117-123 (2017).

[13] H. Zhuang, W. Xu, L. Lin, M. Huang, M. Xu, S. Chen, Z. Cai, "*Construction of one dimensional $ZnWO_4@SnWO_4$ core-shell heterostructure for boosted photocatalytic performance*" J. Mater. Sci. Technol. **35**, 2312-2318 (2019).

[14] H.R. Yousefi, B. Hashemi, "*Photocatalytic properties of Ag@Ag-doped ZnO core-shell nanocomposite*", J. Photochem. Photobiol. A Chem. **375**, 71-76 (2019).

[15] M.A. Salem, E.A. Bakr, H.G. El-Attar, "*Pt@Ag and Pd@Ag core/shell nanoparticles for catalytic degradation of Congo red in aqueous solution*", Spectrochim. acta A. **188**, 155-163 (2018).

[16] H. Rosi, S. Kalyanasundaram, "*Synthesis, characterization , structural and optical properties of titanium-dioxide nanoparticles using Glycosmis cochinchinensis Leaf extract and its photocatalytic evaluation and antimicrobial properties*", World News Nat. Sci. **17**, 1-15 (2018).

[17] S.H. Joo, J.Y. Park, C.K. Tsung, Y. Yamada, P. Yang, G.A. Somorjai, "*Thermally stable Pt/mesoporous silica core-shell nanocatalysts for high-temperature reactions*", Nat. Mater. **8**, 126-131 (2009).

[18] P. Dong, E. Cui, G. Hou, R. Guan, Q. Zhang, "*Synthesis and photocatalytic activity of $Ag_3PO_4/TiOF_2$ composites with enhanced stability*", Mater. Lett. **143**, 20-23 (2015).

[19] J. Zhang, L. Zhang, "*Nanostructures for surface plasmons*", Adv. Opt. Photonics **4**(2), 157-321 (2012).

[20] C. Burda, X. Chen, R. Narayanan, M.A. El-Sayed, "*Chemistry and properties of nancrystals of different shapes*", Chem. Rev. **105**, 1025-102 (2005).

[21] P. Drude, "*Zur elektronentheorie der metalle*", Annalen der Physik **305**(4), 566-613 (1900).

[22] P. Drude, "*Zur elektronentheorie der metalle; ii. teil. galvanomagnetische und thermomagnetische effecte*", Annalen der Physik **308**, 369-402 (1900).

[23] Stafan A. Maier, "*Plasmonics: Fundamentals And Applications*", Springer, New York, NY (2007).

[24] L. Tang, J. Casas, M. Venkataramasubramani, "*Magnetic Nanoparticle Mediated Enhancement of Localized Surface Plasmon Resonance for Ultrasensitive Bioanalytical Assay in Human Blood Plasma*", Anal. Chem. **85**(3), 1431-1439 (2013).

[25] C. Bohren, D. Huffman, "*Absorption and Scattering of Light by Small Particles*", John Wiley and Sons, New york, USA (2008).

[26] K. Tanabe, "*A simple optical model well explains plasmonic-nanoparticle-enhanced spectral photocurrent in optically thin solar cells*", Nanoscale Res. Lett. **11**, 236245 (2016).

[27] Yi-Tao Long, Chao Jing, "*Localized Surface Plasmon Resonance Based Nanobiosensors*", Springer, New York, USA (2014).

[28] M. Hu, et al. "*Gold nanostructures: engineering their plasmonic properties for biomedical applications*", Chem. Soc. Rev. **35**(11), 1084-1094 (2006).

[29] S.L. Boris, "*Optimum forward light scattering by sperical and spheroidal dielectrics nanoparticles with high refractive index*", ACS Photonics **7**(2), 993-999 (2015).

[30] Uwe Kreibig, Michael Vollmer, "*Optical Properties of Metal Clusters*", Springer, Berlin, Heidelberg (1995).

[31] A.D. Kondorskiy, K.S. Kislov, N.T. Lam, V.S. Lebedev, "*Absorption of light by hybrid metalorganic nanostructures of elongated shape*", J. Russian Laser Res. **36**(2), 175-192 (2015).

[32] A.A. Ismail, A.V. Gholap, Y.A. Abbo, "*Enhancement of local electric field in core-shell orientation of ellipsoidal metal/dielectric nanoparticles*", Cond. Matt. Phy. **20**, 23401 (2017).

[33] Andreas Trügler, "*Optical Properties of Metallic Nanoparticles, Basic Principles and Simulation*" Springer, Switzerland **232** (2016).

[34] L. Fernandez, et al. "*Photodegradation of organic poluttants in water by immobilized porphyrins and phthalocyanines*", J. Porphyrins Phthalocyanines, **20**, 2-17 (2016).

[35] Richa Srivastava, "*Synthesis and Characterization Techniques of Nanomaterials*", Int. J. Green Nanotech. **4**, 17-27 (2012).

[36] M.C. Wu, et al. "*Photo-induced disinfection property and photocatalytic activity based on the synergistic catalytic technique of Ag doped* TiO_2 *nanofibers*", Appl. Surf. Sci. **484**, 326-334 (2019).

[37] P.W. Hawkes, J.C.H. Spence, "*Science of Microscopy*", Springer, New York, USA (2007).

[38] Z. Zhang, et al. "*In-situ growth of all-solid Z-scheme heterojunction photocatalyst of* $Bi_7O_9I_3$/ *g-*C_3N_4 *and high efficient degradation of antibiotic under visible light*", Appl. Cata. B: Environ. **261**, 118212 (2020).

[39] M. Wang, H. Wang, Y. Ren, C. Wang, Z. Weng, B. Yue, H. He, "*Construction of g-C_3N_4-mNb_2O_5 Composites with Enhanced Visible Light Photocatalytic Activity*", Nanomaterials. **8**, 427 (2018).

[40] P.S. Mbule, "*The effects of the ZnO nanoparticles buffer layer on organic solar cells (M.Sc Thesis)*", University of the Free State, Republic of South Africa, 2013.

[41] Swati S. Kulkarni and Mahendra D. Shirsat, "*Optical and Structural Properties of Zinc Oxide Nanoparticles*", Int. J. Adv. Res. Phy. Sci. (IJARPS) **2**, 14-18 (2015).

[42] S.C. Singh, R.K. Swarnkar, R. Gopal, "*Zn/ZnO core/shell nanoparticles synthesized by laser ablation in aqueous environment: Optical and structural characterizations*", Bull. Mater. Sci. **33**, 21-26 (2010).

[43] D. Bera, L. Qian, T.K. Tseng, P.H. Holloway, "*Quantum Dots and Their Multimodal Applications: A Review*", Materials **3**(4), 2260-2345 (2010).

[44] M.H. Huang, et al, "*Room-Temperature Ultraviolet Nanowire Nanolasers*", Science, **292**, 1897 (2001).

[45] J.C. Johnson, et al, "*Single Nanowire Lasers*", J. Phys. Chem. B **105**, 11387-11390 (2001).

[46] M.M. Ismail, W.Q. Cao, M.D. Humadi, "*Synthesis and optical properties of Au/ZnO core-shell nanorods and their photocatalytic activities*", Optik **127**, 4307-4311 (2016).

[47] S. Siuleiman, N. Kaneva, A. Bojinova, K. Papazova, A. Apostolov, D. Dimitrov, "*Photodegradation of Orange II by ZnO and TiO_2 powders and nanowire ZnO and ZnO/TiO_2 thin films*", Colloids Surf. A: Physicochem. Engg. Asp. **460**, 408-413 (2014).

[48] R.A. Rakkesh, S. Balakumar, "*Facile synthesis of ZnO/TiO_2 core-shell nanostructures and their photocatalytic activities*", J. Nanosci. Nanotechnol. **13**, 370-376 (2013).

[49] N. Senthil Kumar, M. Ganapathy, S. Sharmila, M. Shankar, M. Vimalan, I. Vetha Potheher, "*ZnO/Ni(OH)$_2$ core-shell nanoparticles: Synthesis, optical, electrical and photoacoustic property analysis*", J. Alloys Comp. **703**, 624-632 (2017).

[50] M.B. Gawande, A. Goswami, T. Asefa, H. Guo, A.V. Biradar, D.L. Peng, R. Zboril, R.S. Varma, "*Core-shell nanoparticles: synthesis and applications in catalysis and electrocatalysis*". J. Chem. Soc. Rev. **7**(44), 7540-7590 (2015).

[51] E.R. Encina, M.A. Pérez, E.A. Coronado, "*Synthesis of Ag@ZnO core-shell hybrid nanostructures: an optical approach to reveal the growth mechanism*", J. Nanopart. Res. **15**, 1688 (2013).

[52] L. He, Y. Liu, J. Liu, Y. Xiong, J. Zheng, Y. Liu, "*Core-Shell Noble-Metal@ Metal-Organic-Framework Nanoparticles with Highly Selective Sensing Property*". Angewandte, Angew. Chemie. **125**, 3829-3833 (2013).

[53] Y. Liu, Z. Tang, "*Functional nanoparticle@MOF core-shell nanostructures*", Adv. Mater. **25**, 5819-5825 (2013).

[54] X. Liu, L. He, J. Zheng, J. Guo, F. Bi, X. Ma, K. Zhao, Y. Liu, R. Song, Z. Tang, "*Solar-Light-Driven Renewable Butanol Separation by CoreShell Ag@ZIF-8 Nanowires*", Adv. Mater. **27**, 3273-3277 (2015).

[55] S. Kalele, S.W. Gosavi, J. Urban, S.K. Kulkarni, "*Nanoshell particles: synthesis, properties and applications*", Curr. Sci. **91**, 1038-1052 (2006).

[56] A. Sambou, B.D. Ngom, L. Gomis, A.C. Beye, "*Turnability of the Plasmonic Response of the Gold Nanoparticles in Infrared Region*", Am. J. Nanomater. **4**, 63-69 (2016).

[57] V.V. Apyari, S.G. Dmitrienko, Y.A. Zolotov, "*Unusual application of common digital devices: Potentialities of Eye-One Pro mini-spectrophotometer - A monitor calibrator for registration of surface plasmon resonance bands of silver and gold nanoparticles in solid matrices*", Sensors Actuators B chemical **188**, 1109-1115 (2013).

[58] M.J. Ko, "*Optical absorption behaviour of metal/semiconductor hybrid nanoparticle composites*", Adv. Mater. Opt. Electron **8**(4), 173-180 (1998).

[59] John David Jackson, "*Classical Electrodynamics*", John Wiley and Sons, USA (1999).

[60] A. Sihvola, "*Mixing Rules with Complex Dielectric Coefficients*", Subsurface Sensing Technologies and Applications, **1**, 393-415 (2000).

[61] M. Popov, G. Sreenivasulu, V.M. Petrov, F.A. Chavez, G. Srinivasan, "*High frequency magneto-dielectric effects in self-assembled ferrite-ferroelectric core-shell nanoparticles*", AIP Adv. **4**, 097117 (2014).

[62] S.E. Starodubtcev, N.V. Korolev, A.F. Klinskikh, P.A. Meleshenko, "*Reduced Polarizability and Local-Field Effect in Self-Assembled Ensemble of Nanoparticles*", J. Nano. Electron. Phys. **5**(1), 01001 (2013).

[63] Vadim Markel, "*Introduction to the Maxwell-Garnett approximation: tutorial*", J. Opt. Soc. Am. A **33**, 1244-1256 (2016).

[64] S. Link, M.A. El-Sayed, "*Shape and size dependence of radiative, non-radiative and photothermal properties of gold nanocrystals*", Int. Reviews Physical Chem. **19**(3), 409-453 (2000).

[65] Z. Kaminskiene, et al. "*Evaluation of Optical Properties of Ag, Cu, and Co Nanoparticles Synthesized in Organic Medium*", Acta Physica Polonica A **123**, 1 (2013).

[66] A.R. Bijanzadeh, M.R. Vakili, R. Khordad, "*A study of the surface plasmon absorption band for nanoparticles*", Int. J. Phy. Sci. **7**, 1943-1948 (2012).

[67] Challa S.S.R. Kummar, "*UV-VIS and Photoluminescence Spectroscopy for Nanomaterials Characterization*", Springer, (2013).

[68] W. Lv, et al. "*Multifunctional Core-Shell Nanoparticle Suspensions for Efficient Absorption*", J. Solar Energy Eng. **135**(2), 021004-1 (2013).

[69] S. Bhardwaj, R. Uma and R.P. Sharma, "*A Study of Metal@Graphene Core-Shell Spherical Nano-Geometry to Enhance the SPR Tunability: Influence of Graphene Monolayer Shell Thickness*", Plasmonics **12**(4), 961-969 (2016).

[70] L. Jule, et al. "*Fano-like resonance and scattering in dielectric (core)-metal (shell) composites embedded in active host matrices*", Phys. Status Solidi B, **252**, 2707-2713 (2015).

[71] S. Shewamare, V.N. Mal'nev, "*Two optical bistability domains in composites of metal nanoparticles with nonlinear dielectric core*", Physica B **407**, 4837-4842 (2012).

[72] J. Ebenezar, "*Recent trends in materials science and applications*", Springer Proceedings in Physics, Springer, Switzerland, (2017).

[73] M.D. McCluskey, S.J. Jokela, "*Defects in ZnO*", J. Appl. Phys. **106**(7), 071101 (2009).

[74] H.Y. Lin, C.L. Cheng, Y.Y. Chou, et al. "*Enhancement of band gap emission stimulated by defect loss*", Opt. Express **14**(6), 2372-2379 (2006).

[75] M. Mahanti and D. Basak, "*Highly enhanced UV emission due to surface plasmon resonance in Ag-ZnO nanorods*", Chem. Phys. Lett. **542**, 110-116 (2012).

[76] Y. Zhao, S. Li, Y. Zeng, Y. Jiang, "*Synthesis and properties of Ag/ZnO core/shell nanostructures prepared by excimer laser ablation in liquid*", APL Mater. **3**, 086103 (2015).

[77] L. Jule, F. Dejene, K. Roro, "*Enhancing absorption in coated semiconductor nanowire/nanorod core-shell arrays using active host matrices*", Opt. Commun. **380**, 186-194 (2016).

[78] M. Azimi, et al. "*Fabrication and Characterization of Core/shell ZnO/Gold Nanostructures and Study of their Structural and Optical Properties*", Orient. J. Chem. Vol. **32**(5), 2517-2523 (2016).

[79] J, Lee, H.S. him, M. Lee, J.K. Song, D. Lee, "*Size-controlled electron transfer and photocatalytic activity of ZnO-Au nanoparticle composites*", J. Phys. Chem. Lett. **2**, 2840-2845 (2011).

[80] A. Wood, M. Giersig, P. Mulvaney, "*Fermi level equilibration in quantum dot-metal nanojunctions*", J. Phys. Chem. B **105** , 8810-8815 (2001).

[81] V. Subramanian, E. Wolf, P.V. Kamat, "*Green emission to probe photoinduced charging events in ZnO-Au nanoparticles: Charge distribution and Fermi-level equilibration*", J. Phys. Chem. B **107**, 7479-7485 (2003).

[82] M. Jakob, H. Levanon, P.V. Kamat, "*Charge distribution between UV-irradiated* TiO_2 *and gold nanoparticles: determination of shift in the Fermi level*", Nano Lett. **3**, 353-358 (2003).

[83] M.R. Kim, Z. Xu, G. Chen, D. Ma, "*Semiconductor and Metallic Core Shell Nanostructures: Synthesisand Applications in Solar Cells and Catalysis*", Chem. A Eur. J. **20**, 11256-11275 (2014).

[84] C. Loo, et al. "*Nanoshell-enabled photonics-based imaging and therapy of cancer*", Techno. Cancer Res. Treat. **3**, 33-40 (2004).

[85] S.A. Shahamirifard, M. Ghaedi, M. Montazerozohori, "*Application of nanostructure* $ZnLI_2$ *complex in construction of optical pH sensor*", Appl. Organometallic Chem. **32**, 1-11 (2017).

[86] N. Shah, F. Claessyns, S. Rimmer, M.B. Arain, T. Rehan, A. Wazwaz, M.W. Ahmad, M. Ul-Islam, "*Effective role of magnetic coreshell nanocomposites in removing organic and inorganic wastes from water*", Recent Pat. Nanotechnol. **10**, 202-212 (2016).

[87] N.K. Grady, N.J. Halas, P. Nordlander, "*Influence of dielectric function properties on the optical response of plasmon resonant metallic nanoparticles*", Chem. Phys. Lett. **399**, 167-171 (2004).

[88] S. Pillai, K. R. Catchpole, T. Trupke, G. Zhang, J. Zhao, M. A. Green, "*Enhanced emission from Si-based light-emitting diodes using surface plasmons*", Appl. phys. Lett. **88**, 16-18 (2006).

[89] M.S. Chen, D.W. Goodman, "*Catalytically active Au: from nano-particles to ultra-thin films*", Acc. Chem. Res. **39**, 739-746 (2006).

[90] N. Yang, K. Aoki, H. Nagasawa, "*Thermal metallization of silver stearate-coated nanoparticles owing to the destruction of the shell structure*", J. Phys. Chem. B **108**, 15027-15032 (2004).

[91] J.P. Wilcoxon , B.L. Abrams, Synthesis, "*Structure and properties of metal nanoclusters*", Chem. Soc. Rev. **35**, 1162-1194 (2006).

[92] G. Beyene, T. Senbeta, B. Mesfin, "*Size dependent optical properties of ZnO@Ag core/shell nanostructures*", Chinese J. Phys. **58**, 235-243 (2019).

[93] C. Noguez, "*Surface plasmons on metal nanoparticles: The influence of shape and physical environment*", J. Phys. Chem. C **111**, 3806-3819 (2007).

[94] P.K. Jain, M.A. El-Sayed, "*Surface plasmon resonance sensitivity of metal nanostructures: physical basis and universal scaling in metal nanoshells*", J. Phys. Chem. C **111**, 17451-17454 (2007).

[95] F. Chen, R.L. Johnston, "*Plasmonic properties of silver nanoparticles on two substrates plasmonic properties of silver nanoparticles on two substrates*", Plasmonics **4**, 147-152 (2009).

[96] G.B. Kassahun, "*High Tunability of Size Dependent Optical Properties of ZnO@M@Au (M = SiO_2, TiO_2, In_2O_3) Core/Spacer/Shell Nanostructure*", Adv. Nano Res. **2**, 1-13 (2019).

[97] N. Senthilkumar, M. Ganapathy, A. Arulraj, M. Meena, M. Vimalan, I. Vetha Potheher, "*Two step synthesis of ZnO/Ag and ZnO/Au core/shell nanocomposites: Structural, optical and electrical property analysis*", J. Alloys Compd. **750**, 171-181 (2018).

[98] E.I. Gorokhova, G.V. Anan'eva, V.A. Demidenko, P.A. Rodnyí, I.V. Khodyuk, E.D. Bourret-Courchesne, "*Structural, optical, and luminescence properties of ZnO: Ga optical scintillation ceramic*", J. Opt. Technol. **75**, 741-746 (2008).

[99] U. Pal, R. Melndrez, V. Chernov, M. Barboza-Flores, "*Thermoluminescence properties of ZnO and ZnO: Yb nanophosphors Thermoluminescence properties of ZnO and ZnO: Yb nanophosphors*", Appl. Phys. Lett. **89**, 148-151 (2006).

[100] C. Zeng, L. Yuan, X. Li, C. Gao, H. Wang, "*Fabrication of urchin-like Ag/ZnO hierarchical nano/microstructures based on galvanic replacement mechanism*

and their enhanced photocatalytic properties", Surf. Interface Anal. **49**, 599-606 (2017).

[101] A. Oliver, et al. "*Controlled anisotropic deformation of Ag nanoparticles by Si ion irradiation*", Phys. Rev. B **74**, 245425 (2006).

[102] A. Sambou, P.D. Tall, K.H. Talla, O. Sakho B.D. Ngom, A.C. Beye, "*Control of the Surface Plasmon Resonance of Two Configurations of Nanoparticles: Simple Gold Nanorod and Gold/Silica Core/Shell*", Nanosci. Nanotechnol. Res. **4**, 1-6 (2017).

[103] M. Liu, P. Guyot-Sionnest, "*Preparation and optical properties of silver chalcogenide coated gold nanorods*", J. Mater. Chem. **16**, 39423945 (2006).

[104] Yoshinobu Aoyagi, Kotaro Kajikawa, "*Optical Properties of Advanced Materials*", Springer Series in Materials Science, Berlin, Germen (2013).

[105] M. Dalarsso, et al. "*Absorption and optimal plasmonic resonances for small ellipsoidal particles in lossy media*", J. Phys. D Appl. Phys. **50**, 345401 (2017).

[106] H.R. Stuart, D.G. Hall, "*Island size effects in nanoparticle-enhanced photodetectors*", Appl. Phys. Lett. **73**, 38153817 (1998).

[107] M. Alsawafta, M. Wahbeh, T. Vo-Van, "*Plasmonic modes and optical properties of gold and silver ellipsoidal nanoparticles by the discrete dipole approximation*", J. nanomater. **2012**, 1-10 (2012).

[108] S.J. Oldenburg, R.D. Averitt, S.L. Westcott, N.J. Halas, "*Nanoengineering of optical resonances*", Chem. Phys. Lett. **288**, 243-247 (1998).

[109] T. Pan, J.P. Huang, Z.Y. Li, "*Optical bistability in metal/dielectric composite with interfacial layer*", Physica B **301**, 190-195 (2001).

[110] M. Piralaee, A. Asgari, "*Modeling of optimum light absorption in random plasmonic solar cell using effective medium theory*", Opt. Mater. **62**, 399-402 (2016).

[111] M. Piralaee, A. Asgari, V. Siahpoush, "*Modeling and optimizing the performance of plasmonic solar cells using effective medium theory*", Phys. Lett. A **381**, 489-493 (2017).

[112] J. Zhang, A. Zayats, "*Multiple Fano resonances in single-layer nonconcentric core-shell nanostructures*", Opt. Express **21**, 707-715 (2013).

[113] J.J. Penninkhof, A. Moroz, A. van Blaaderen, A. Polman, "*Optical properties of spherical and oblate spheroidal gold shell colloids optical properties of spherical and oblate spheroidal gold shell colloids*", J. Phys. Chem. C **112**, 4146-4150 (2008).

[114] M. Wang, M. Cao, X. Chen, N. Gu, "*Subradiant plasmon modes in multilayer metalDielectric nanoshells*", J. Phys. Chem. C **115**, 20920-20925 (2011).

[115] M.J. Haqueet et al, "*Synthesis of ZnO nanoparticles by two different methods and comparison of their structural, antibacterial, photocatalytic andoptical properties*", Nano express **1**(1), 010007 (2020)

[116] C.B. Onga, L.Y. Ngb, A.W. Mohammad, "*A review of ZnO nanoparticles as solar photocatalysts: Synthesis, mechanisms and applications*", Renewable and Sustainable Energy Reviews **81**, 536-551 (2018).

[117] A. Kolodziejczak-Radzimska and T. Jesionowski, "*Zinc oxide-from synthesis to application: A review*", Materials **4**(7), 2833-2881 (2014).

[118] M. Sudha, M. Rajarajan, "*Deactivation of Photocatalytically active Zno nanoparticle by surface capping with poly viny pyrrodidone*", IOSR J. Appl. chem. **3**, 345-53 (2013).

[119] A. Mohamad, A. Sandhanasamy, D Martin et al. "*Study on photocatalytic and impedance spectroscopy investigations of composite CuO/ZnO nanoparticles*", J. Mater. Sci.: Mater. Electron. **30**(14), 13708-13718 (2019).

[120] S. Jin, et al. "*Photocatalytic antibacterial application of zinc oxide nanoparticles and self-assembled networks under dual UV irradiation for enhanced disinfection*", Int. J. Nanomed. **14**, 1737-1751 (2019).

[121] E.S. Rodrigues, et al. "*ZnO nanoparticles with tunable bandgap obtained by modified Pechini method*", Appl. Phys. A **125**(8), 1-6 (2019).

[122] R. Suntako, "*Effect of synthesized ZnO nanoparticles on thermal conductivity and mechanical properties of natural rubber*", Mater. Sci. Eng. **284**, 012017 (2017).

[123] R. Suntako, "*Effect of zinc oxide nanoparticles synthesized by a precipitation method on mechanical and morphological properties of the CR foam*", Bull. Mater. Sci. **4**(38), 1033-1038 (2015).

[124] V. Kumar, S. Kumari, P. Kumar, M. Kar, L. Kumar, "*Structural analysis by rietveld method and its correlation with optical propertis of nanocrystalline zinc oxide*", Adv. Mater. Lett. **6**, 139-147 (2015).

[125] S. Kundu, S. Sain, B. Satpati, S.R. Bhattacharyya, S.K. Pradhan, "*Structural interpretation, growth mechanism and optical properties of ZnO nanorods synthesized by a simple wet chemical route*", RSC Adv. **5**, 23101-23113 (2015).

[126] S. Rani, P. Suri, P.K. Shishodia, R.M Mehra, "*Synthesis of nanocrystalline ZnO powder via sol-gel route for dye-sensitized solar cells*", Sol. Energy Mater. Sol. Cells. **92**, 1639-1645 (2008).

[127] D. Chu, S. Li, "*Growth and Electrical Properties of Doped ZnO by Electrochemical Deposition*", New J. Glass Ceram. **2**, 13-16 (2012).

[128] Z.M. Kakhaki, A. Youzbashi and N. Naderi, "*Optical Properties of Zinc Oxide Nanoparticles Prepared by a One-Step Mechanochemical Synthesis Method*", J. Phys. Sci. **26**(2), 41-51 (2015).

[129] P. Shubha, K. Namratha, Jit Chatterjee, M.S. Mustak, K.Byrappa, "*Use of Honey in Stabilization of ZnO Nanoparticles Synthesized via Hydrothermal Route and Assessment of their Antibacterial Activity and Cytotoxicity*", Glob. J. Nanomed. **2**(2), (2017).

[130] S. Narendhran, Rajeshwari Sivaraj, "*Biogenic ZnO nanoparticles synthesized using L. aculeata leaf extract and their antifungal activity against plant fungal pathogens*", Bull. Mater. Sci. **39**(1), 15 (2016).

[131] C. Kun-Ching, C. Ho, C. Chih-Hao, K. Mu-Jung, L. Xuan-Rong, "*A Study of Mixed Vegetable Dyes with Different Extraction Concentrations for Use as a Sensitizer for Dye-Sensitized Solar Cells*", Int. J. Photoenergy, **2014**, 1-5 (2014).

[132] N. Bala, S. Saha, M. Chakraborty, M. Maiti, S. Das, R. Basub, P. Nandy, "*Green synthesis of zinc oxide nanoparticles using Hibiscus subdariffa leaf extract: effect of temperature on synthesis, anti-bacterial activity and anti-diabetic activity*", RSC Adv. **5**, 4993-5003 (2015).

[133] Prasanta Sutradhar, Mitali Saha, "*Synthesis of zinc oxide nanoparticles using tea leaf extract and its application for solar cell*", Bull. Mater. Sci., **38**(3), 653-657 (2015).

[134] S. Jurablu, M. Farahmandjou, T.P. Firoozabadi, "*Sol-Gel Synthesis of Zinc Oxide (ZnO) Nanoparticles: Study of Structural and Optical Properties*", J. Sci., Islamic Republic of Iran **26**(3), 281-285 (2015).

[135] S.K. Mishra, R.K. Srivastava, S.G. Prakash, "*ZnO nanoparticles: Structural, optical and photoconductivity characteristics*", J. Alloys Compd. **539**, 1-6 (2012).

[136] A.C. Mohana, B. Renjanadevi, "*Preparation of Zinc Oxide Nanoparticles and its Characterization Using Scanning Electron Microscopy (SEM) and X-Ray Diffraction(XRD)*", Procedia Technol. **24**, 761-766 (2016).

[137] A. Srithar, J.C. Kannan, T.S. Senthil, "*Preparation and Characterization of Ag doped ZnO nanoparticles and its Antibacterial Applications*", J. Adv. Chem. **6**(13), (2017).

[138] Y. He, Z. Huang, Z. Ma, B. Yao, H. Liu, L. Hu, Q. Zhao, Q. Yang, D. Liu, D. Du, "*Highly efficient photocatalytic performance and mechanism of*

a-ZnTcPc/g-C_3N_4 composites for methylene blue and tetracycline degradation under visible light irradiation", Appl. Surf. Sci. **498**, 143834 (2019).

[139] C. Wattanawikkam, T. Kansa-ard, W. Pecharapa, "*X-ray absorption spectroscopy analysis and photocatalytic behavior of $ZnTiO_3$ nanoparticles doped with Co and Mn synthesized by sonochemical method*", Appl. Sur. Sci. **474**, 169-176 (2019).

[140] M.J. Chatterjee, S.T. Ahamed, M. Mitra, C. Kulsi, A. Mondal, D. Banerjee, "*Visible-light influenced photocatalytic activity of polyaniline -bismuth selenide composites for the degradation of methyl orange, rhodamine B and malachite green dyes*", Appl. Sur. Sci. **470**, 472-483 (2019).

[141] A. Kumar, A. Kumar, G. Sharma, A.H. Al-Muhtaseb, M. Naushad, A.A. Ghfar, F.J. Stadler, "*Quaternary magnetic BiOCl/g-$C_3N_4/Cu_2O/Fe_3O_4$ nano-junction for visible light and solar powered degradation of sulfamethoxazole from aqueous environment*", Chem. Eng. J. **334**, 462-478 (2018).

[142] S.P. Goutam, G. Saxena, V. Singh, A.K. Yadav, R.N. Bharagava, K.B. Thapa, "*Green synthesis of TiO_2 nanoparticles using leaf extracts of Jatropha curcas L. for photocatalytic degradation of tannery wastewater*", Chem. Eng. J. **336**, 386-396 (2018).

[143] G.S.C. Muthukumaran, K.S.S. Santhiya, R.S. Pradeep, N.M. Kumar, "*Biosynthesis, characterization, and antibacterial activity of zinc oxide nanoparticles derived from Bauhinia tomentosa leaf extract*", J. Nanostructure Chem. **8**, 293-299 (2018).

[144] S.K. Naveen Kumar, K.C. Gayithri, S. Kiran, "*Fabrication and characterization of high performance resistive type humidity sensor based on ZnO/pyrrole composite materials*", Int. J. ChemTech Res. **7**, 936-942 (2015).

[145] L. Znaidi, "*Solgel-deposited ZnO thin films: A review*", Mater. Sci. Eng B. **174**, 18-30 (2010).

[146] L. Saikia, D. Bhuyan, M. Saikia, B. Malakar, D.K. Dutta, P. Sengupta, "*Photocatalytic performance of ZnO nanomaterials for self sensitized degradation of malachite green dye under solar light*", Appl. Catal. A Gen. **490**, 42-49 (2015).

[147] X. Zhu, G. Wen, H. Liu, et al. "*One-step hydrothermal synthesis and characterization of Cu doped* TiO_2 *nanoparticles/nanobucks/nanorods with enhanced photocatalytic performance under simulated solar light*", J. Mater. Sci: Mater. Electron **30**, 13726-13734 (2019).

[148] A. Priyadharsan, et al. "*Crumpled sheet like graphene based* $WO_3 - Fe_2O_3$ *nanocomposites for enhanced charge transfer and solar photocatalysts for environmental remediation*", App. Sur. Sci. **470**, 114-128 (2019).

[149] G. Beyene, T. Senbeta, B. Mesfin, Q. Zhang, "*Plasmonic properties of spheroidal spindle and disc shaped core-shell nanostructures embedded in passive host matrices*", Opt. Quant. Electron. **52**, 157 (2020).

[150] G.K. Naik, S.M. Majhi, K.U. Jeong, I.H. Lee, Y.T. Yu, "*Nitrogen doping on the core-shell structured Au@TiO2 nanoparticles and its enhanced photocatalytic hydrogen evolution under visible light irradiation*", J. Alloys. Compd. **771**, 505-512 (2019).

[151] B. Bartosewicz, M. Michalska-Domanska, M. Liszewska, D. Zasada, B.J. Jankiewicz, "*Synthesis and characterization of noble metal-titania core-shell nanostructures with tunable shell thickness*", Beilstein J. Nanotechnol. **8**, 2083-2093 (2017).

[152] K. Mondal, A. Sharma, "*Recent advances in the synthesis and application of photocatalytic metalmetal oxide core-shell nanoparticles for environmental remediation and their recycling process*", RSC Adv. **6**, 83589-83612 (2016).

[153] E.J. Guidelli, O. Baffa, D.R. Clarke, "*Enhanced UV Emission from Silver/ZnO and Gold/ZnO Core-Shell Nanoparticles: Photoluminescence, Radioluminescence, and Optically Stimulated Luminescence*", Sci. Rep. **5**, 1-11 (2015).

[154] S. Lee, J. Lee, K. Nam, W.G. Shin, Y. Sohn, "*Application of Ni-Oxide@TiO_2 core-shell structures to photocatalytic mixed dye degradation, CO oxidation, and supercapacitors*", Materials **9**, 1-15 (2016).

[155] B. Wang, X. Zhu, S. Li, M. Chen, H. Lu, Y. Yang, "*Ag@SiO_2 Core-shell Nanoparticles Embedded in a TiO_2 Mesoporous Layer Substantially Improve the Performance of Perovskite Solar Cells*", Nanomater. **8**, 701 (2018).

[156] K. Aranishi, H.L. Jiang, T. Akita, M. Haruta, Q. Xu, "*One-step synthesis of magnetically recyclable Au/Co/Fe triple-layered core-shell nanoparticles as highly efficient catalysts for the hydrolytic dehydrogenation of ammonia borane*", Nano Res. **4**, 1233-1241 (2011).

[157] X. Shao, B. Li, B. Zhang, L. Shao, Y. Wu, "*Au@ZnO core-shell nanostructures with plasmon-induced visible-light photocatalytic and photoelectrochemical properties*", Inorg. Chem. Front. **3**, 934-943 (2016).

[158] M. Aminuzzaman, L.P. Ying, W.S. Goh, A. Watanabe, "*Green synthesis of zinc oxide nanoparticles using aqueous extract of Garcinia mangostana fruit pericarp and their photocatalytic activity*", Bull. Mater. Sci. **41**, 50 (2018).

[159] C. Gomez-Sols, J.C. Ballesteros, L.M. Torres-Martnez, I. Jurez-Ramrez, L.A. Daz Torres, M. Elvira Zarazua-Morin, S.W. Lee, "*Rapid synthesis of ZnO nano-corncobs from Nital solution and its application in the photodegradation of methyl orange*", J. Photochem. Photobiol. A Chem. **298**, 49-54 (2015).

[160] Y. Jin, J. Long, X. Ma, T. Zhou, Z. Zhang, H. Lin, J. Long, X. Wang, "*Synthesis of caged iodine-modified ZnO nanomaterials and study on their visible light photocatalytic antibacterial properties*", Appl, Catal. B Environ. **256**, 117873 (2019).

[161] G. Zhang, D. Chen, N. Li, Q. Xu, H. Li, J. He, J. Lu, "*Fabrication of Bi_2MoO_6/ZnO hierarchical heterostructures with enhanced visible-light photocatalytic activity*", Appl. Catal. B Environ. 313-324 (2019).

[162] B. Xu, H. Maimaiti, S. Wang, A. Awati, Y. Wang, J. Zhang, T. Chen, "*Preparation of coal-based graphene oxide/SiO_2 nanosheet and loading ZnO nanorod for photocatalytic Fenton-like reaction*", Appl. Surf. Sci. **498**, 143835 (2019).

[163] Y. Yang, L. Xu, C. Su, J. Che, W. Sun, H. Gao, "*Electrospun ZnO/Bi_2O_3 Nanofibers with Enhanced Photocatalytic Activity*", J. Nanomater. **2014**, 1-7 (2014).

[164] J. Zhai, X. Tao, Y. Pu, X.F. Zeng, J.F. Chen, "*Core/shell structured ZnO/SiO_2 nanoparticles: Preparation, characterization and photocatalytic property*", Appl. Surf. Sci. **257**, 393-397 (2010).

[165] J. Verma, A. Bhattacharya, "*Development of coating formulation with silica titania core shell nanoparticles against pathogenic fungus*", R. Soc. Open Sci. **5**(8), 180633 (2018).

[166] A. Giesriegl, J. Blaschke, S. Naghdi, D. Eder, "*Rate-Limiting Steps of Dye Degradation over Titania-Silica Core-Shell Photocatalysts*", Catalysts. **9**, 583 (2019).

[167] B. Pant, H.R. Pant, D.R. Pandeya, G. Panthi, K.T. Nam, S.T. Hong, C.S. Kim, H.Y. Kim, "*Characterization and antibacterial propertis of Ag NPs loaded nylon-6 nanocomposite prepared by one-staep electrospining process*", Colloids and Surfaces A: Physicochem. Eng. Asp. **395**, 94-99 (2012).

[168] J. Zhang, Y. Huang, Y. Dan, L. Jiang, "*P3HT/Ag/TiO_2 ternary photocatalyst with significantly enhanced activity under both visible light and ultraviolet irradiation*", Appl. Surf. Sci. **488**, 228-236 (2019).

[169] X. Song, X. Shi, "*Biosynthesis of Ag/reduced graphene oxide nanocomposites using Shewanella oneidensis MR-1 and their antibacterial and catalytic applications*", Appl. Surf. Sci. **491**, 682-689 (2019).

[170] Y. Zhai, Y. Zhang, J. Yin, X. Fan, "*Enhanced photocatalytic property of Ag loaded on well-defined ferroelectric* $Na_3VO_2B_6O_{11}$ *crystals under visible light irradiation*", Appl. Surf. Sci. **484**, 981-989 (2019).

[171] C. Liu, T. Sun, L. Wu, J. Liang, Q. Huang, J. Chen, W. Hou, "*N-doped* $Na_2Ti_6O_{13}$ *at* TiO_2 *core-shell nanobelts with exposed 101 anatase facets and enhanced visible light photocatalytic performance*", Appl. Catal. B Environ. **170**, 1724 (2015).

[172] S. Vignesh, et al. "*Highly efficient visible light photocatalytic and antibacterial performance ofPVP capped Cd:Ag: ZnO photocatalyst nanocomposites*", App. Surf. Sci. **479**, 914-929 (2019).

[173] E. Alzahrani, "*Photodegradation of binary Azo dyes using core-shell* $Fe_2O_4/SiO_2/TiO_2$ *nanospheres*", Am. J. Anal. Chem. **8**, 95-115 (2017).

[174] D. Tahir, K. Hee Jae, "*Effect of growth temperature on structural and electronic properties of ZnO thin films*", AIP. Conf. Proc. 1801 (2017).

[175] S.A.A. Terohid, S. Heidari, A. Jafari, S. Asgary, "*Effect of growth time on structural, morphological and electrical properties of tungsten oxide nanowire*", Appl. Phys. A **124**, 567 (2018).

[176] Y. Xu, H. Xu, H. Li, J. Yan, J. Xia, S. Yin, Q. Zhang, "*Ionic liquid oxidation synthesis of Ag@AgCl core-shell structure for photocatalytic application under visiblelight irradiation*", Colloids Surf. A: Physicochem. Eng. Asp. **416**, 80-85 (2013).

[177] Z. He, et al, "*BiOCl/BiVO_4 p-n heterojunction with enhanced photocatalytic activity under visible-light irradiation*", J. Phys. Chem. C. **118**, 389-398 (2014).

[178] D. Majhi, et al, "*One pot synthesis CdS/BiOBr/$Bi_2O_2CO_3$: A novel ternary double Z-acheme heterostructure photocatalyst for efficient degradation of atrazine*", Appl. Catal. B: Environ. **260**, 118222 (2020).

[179] Y. Liu, J. Xu, L. Wang, H. Zhang, P. Xu, X. Duan, H. Sun, S. Wang, "*Three-dimensional BiOI/BiOX (X = Cl or Br) nanohybrids for enhanced visible-light photocatalytic activity*", Nanomater. **7**, 64 (2017).

[180] A.N. Kadam, D.P. Bhopate, V.V. Kondalkar, S.M. Majhi, C.D. Bathula, A.V. Tran, S.W. Lee, "*Facile synthesis of Ag-ZnO core-shell nanostructures with enhanced photocatalytic activity*", J. Ind. Eng. Chem. **61**, 78-86 (2018).

[181] R. Raji, et al. "*ZnO:Ag nanorods as efficient photocatalysts: Sunlight driven photocatalytic degradation of sulforhodamine B*", App. Surf. Sci. **427**, 863-875 (2018).

[182] Z. Peng, H. Tang, Y. Tang, K.F. Yao, H.H. Shao, "*Synthesis and Photocatalytic Activity of Magnetically Recoverable Core-Shell Nanoparticles*", Int. J. Photoenergy. **2014**, 8 (2014).

[183] N. Neelakandeswari, K. Nithya, N. Rajasekaran, S.S. Kumar, P. Yuvasree, K. Uthayarani, M. Chitra, "*Phytochemical Preparation, Characterization and Photocatalytic Applications of Ag - TiO_2 Nanocatalyst*", Adv. Mater. Res. **1086**, 1-6 (2015).

[184] H. Wang, S. Li, Y. Liu, J. Ding, Y. Lin, H. Xu, B. Xu, C. Nan, "$Bi_{1-x}La_xCuSeO$ *as New Tunable Full Solar Light Active Photocatalysts*", Sci. Rep. **6**, 2-10 (2016).

[185] V. Patidar, P. Jain, "*Green Synthesis of* TiO_2 *Nanoparticle Using Moringa Oleifera Leaf Extract*", Int. Res. J. Eng. Technol. **4**, 470-473 (2017).

[186] S. Subhapriya, P. Gomathipriya, "*Green synthesis of titanium dioxide (*TiO_2*) nanoparticles by Trigonella foenumgraecum extract and its antimicrobial properties*", Microb. Pathog. **116**, 215-220 (2018).

[187] X. Zhu, Z. Liu, J. Fang, S. Wu, W. Xu, "*Synthesis and characterization of mesoporous* Bi/TiO_2 *nanoparticles with high photocatalytic activity under visible light*", J. Mater. Res. **28**, 1334-1342 (2013).

[188] D.V. Raorane, P.S. Chavan, S.R. Pednekar, R.S. Chaughule, "*Green and Rapid Synthesis of Copper-Doped* TiO_2 *Nanoparticles with Increased Photocatalytic Activity*", Adv. Chem. Sci. **6**, 13-20 (2017).

[189] G. Lusvardi, C. Barani, F. Giubertoni, G. Paganelli, "*Synthesis and Characterization of* TiO_2 *Nanoparticles for the Reduction of Water Pollutants*", Materials, **10**, 1-11 (2017).

[190] T.T. Loan, N.N. Long, "*Optical Properties of Anatase and Rutile* $TiO_2 : Cr^{3+}$ *Powders*", VNU J. Sci. Math. Phys. **30**, 59-67 (2014).

[191] X. Zhang, G. Xiang,"*Ferromagnetic ZnO-*TiO_2 *Core-Shell Nanowire PhotoCatalyst with High Efficiency and Recyclability*", Appl. Mech. Mater. **93**, 1702-1705 (2011).

[192] A. El Nemr, E.A. Gomaa, S.M. Eldafrawy, M.A. Mousa, E.T. Helmy, "*Mangrove Leaves Aqueous Extract Mediated Green Synthesis of TiO_2 and Boron-doped TiO_2 Nanoparticles and their Ecotoxic Effect on Rotifers*", Egypt. J. Aquat. Biol. Fish. **22**, 149-162 (2018).

[193] M.C. Wu, Y.H. Chang, T.H. Lin, "*Bismuth doping effect on crystal structure and photodegradation activity of Bi-TiO_2 nanoparticles*", Jpn J. Appl. Phys. **56**, 2-6 (2017).

[194] Y. Nan, L.I. Fuyan, J. Tiancai, L.I.U. Chongchong, S.U.N. Hushan, W. Lei, X.U. Hui, "*Biogenic synthesis of silver nanoparticles using ginger (Zingiberofficinale) extract and their antibacterial properties againstaquatic pathogens*", Acta Ocean. Sin. **36**, 95-100 (2017).

[195] A. Gour, N.K. Jain, Artif. Cells, "*Advances in green synthesis of nanoparticles*", Artif. Cells. Nanomedicine, Biotechnol. **47**, 844-851 (2019).

[196] P. Rajput, S. Dasgupta, M. Chakraborty, S. Nandwani, M. Hajoori, Int. J. Pharm. Biol. Sci. **8**, 1086-1092 (2018).

[197] G.H. Priyaa, K.B. Satyan, "*Biological synthesis of silver nanoparticles using ginger (Zingiber Officinale) extract*", J. Environ. Nanotechnol. **3**, 32-40 (2014).

[198] T.N. Ravishankar, K. Manjunatha, T. Ramakrishnappa, G. Nagaraju, Dhanith Kumar, S. Sarakar, B.S. Anandakumar, G.T. Chandrappa, Viswanath Reddy, J. Dupont, Mater. Sci. Semicond. Process. **26**, 7-17 (2014).

[199] G. Chen, G.L. Fang, G.D. Tang, "*Photoluminescence and photocatalytic properties of BiOCl and* $Bi_{24}O_{31}Cl_{10}$ *nanostructures synthesized by electrolytic corrosion of metal Bi*", Mater. Res. Bull. **48**, 1256-1261 (2013).

[200] K. Wang, X. Yang, S. Hu, L. Hu, "*Fabrication of Zscheme* Ag_3PO_4/TiO_2 *Heterostructures for Enhancing Visible Photocatalytic Activity*", Nanoscale Res. Lett. **14**, 203 (2019).

[201] T.V. Surendra, S.M. Roopan, N.A. Al-dhabi, M.V. Arasu, G. Sarkar, "*Vegetable Peel Waste for the Production of ZnO Nanoparticles and its Toxicological Efficiency, Antifungal, Hemolytic, and Antibacterial Activities*", Nanoscale Res. Lett. **11**, 546 (2016).